University of Leoben, Austria

Dissertation

Damage Tolerant Design Concepts for the Application of High strength Materials in Railway Switch Components

DI (FH) Stefan Kolitsch, M.Sc.

Material Center Leoben Forschung GmbH

&

Erich Schmidt Institute of Material Science

1st Advisor:
Univ. Prof. DI Dr. mont. Reinhard Pippan
Erich Schmid Institute of Materials Science
Austrian Academy of Sciences
University of Leoben, Austria

2nd Advisor:
Univ.-Prof. DI Dr.mont. Thomas Antretter
Institute for Mechanical Engineering
University of Leoben, Austria

August 2017

Affidavit

I declare in lieu of oath, that I wrote this thesis and performed the associated research myself, using only literature cited in this volume.

Abstract

Switch components, especially switch blades, are highly loaded rails. The high loads are a result of small bending radii during the manufacturing process and high dynamic forces due to the wheel contact transition from the stock to the switch rail. Dealing with those high loads, it requires an improvement of the wear resistance and the application of high strength materials. The implementation of new material types demands applications of new design concepts and the comparison to the manufacturing processes of conventional materials. For this reason, in the present thesis, modified and new damage tolerant design concepts, for the static failure during the bending process and the dynamic behavior in track, have been investigated. Furthermore, the application of four different material types with different tensile strengths and microstructures have been analyzed.

For the development of a design criterion in the bending process, specimens with different crack lengths have been tested until failure. In consideration of the load and small flaws, a new concept, the somewhat modified static strain based Kitagawa-Takahashi diagram, is investigated. Here, the nominal failure strain in the outer fiber, due to the bending load, is plotted over the flaw size. The failure strain is estimated by fracture mechanics criteria, using the *J*-integral as a crack driving force and compared with the experimental results for the different material types.

For cyclically loaded components, two different approaches are compared. The Smith diagram for different loads and surface conditions is presented in the stress based approach. Additionally, the estimated failure curves are compared with fatigue experiments at selected load ratios and surface conditions. Considering cracks, the Kitagawa-Takahashi diagram represents the endurable stress range and is represented for the different material types and stress ratios in the fracture mechanics approach.

Furthermore, for the analytical calculation of the crack growth, an enhanced method for the calculation of the geometry factor is investigated. This method provides the possibility to calculate the stress intensity of semi-elliptical cracks, where the crack is close to the specimen boundaries for tension and bending around two axes.

Moreover, the influence of the stress concentration of a notch on the crack growth behavior of short cracks is investigated by experiments. For this purpose, an advanced method with respect to the direct current potential drop method is used for estimation of crack lengths, considering semi-elliptical shapes. The experimental results are then compared with the analytically calculated solutions of the crack growth behavior, considering plastic deformation in front of the notch root.

Kurzfassung

Weichenbestandteile, im Speziellen Zungenschienen, sind hochbeanspruchte Schienenbauteile. Diese Beanspruchung entsteht durch kleine Biegeradien im Herstellungsprozess und im Betrieb durch hohe dynamische Kräfte während des Wechsels des Radkontaktes von der Backen- auf die Zungenschiene. Diese hohen Belastungen fordern die Verbesserung der Verschleißfestigkeit und den Einsatz hochfester Materialien. Bei Verwendung neuer Materialien sind neue Auslegungskonzepte und der Vergleich zu den Herstellungsprozessen der derzeitig verwendeten Materialien notwendig. In der vorliegenden Arbeit werden dazu abgeänderte und neue Schädigungskonzepte für das statische Versagen im Biegeprozess und der dynamischen Schädigung im Betrieb untersucht. Dies wird anhand von vier unterschiedlichen Materialien mit verschiedenen Zugfestigkeiten und Mikrostrukturen durchgeführt.

Zur Entwicklung eines Schädigungsparameters für den Biegeprozess wurden Proben mit unterschiedlichen Risslängen bis hin zum statischen Versagen getestet. Unter Berücksichtigung der Last und der Fehlergröße wurde ein neues Konzept, das statisch dehnungsbasierende Kitagawa-Takahashi Diagramm, entwickelt. Dabei wird die nominelle Dehnung in der Randfaser bei Biegung über die Fehlergröße aufgetragen. Die Bruchdehnung wird dabei über bruchmechanische Ansätze, genauer gesagt mit dem *J*-integral als risstreibende Kraft, verwendet und mit den experimentellen Ergebnissen verglichen.

Für die Beurteilung von zyklisch belasteten Bauteilen werden zwei Ansätze verglichen. Einerseits wird das Smith Diagramm für verschiedene Belastungen und Oberflächenbeschaffenheiten in einem spannungsbasierenden Konzept verwendet. Zusätzlich werden die berechneten Fehlerkurven mit Dauerfestigkeitsexperimenten für verschiedene Belastungen und Oberflächenqualitäten miteinander verglichen. Andererseits wird im bruchmechanischen Konzept, unter Berücksichtigung von Rissen, das Kitagawa-Takahashi Diagramm zur Beurteilung der ertragbaren Spannungsschwingbreite für die verschiedenen Werkstoffe und Spannungsverhältnisse dargestellt.

Des Weiteren wurde für die analytische Berechnung des Rissfortschrittes eine erweiterte Geometriefunktion entwickelt, welche die Berechnung der Spannungsintensität für halb-elliptische Risse nahe der Probenoberfläche unter Zug und Biegung um zwei Achsen ermöglicht.

Zusätzlich wurde der Einfluss der Spannungsintensität einer Kerbe auf das Kurzrisswachstum anhand von Experimenten untersucht. Dazu wurde ein erweitertes Verfahren anhand der Potentialmessmethode zur Abschätzung der Risslänge von halb-elliptischen Rissen entwickelt. Die experimentellen Ergebnisse werden dann unter Berücksichtigung der plastischen Verformung vor der Kerbe mit den analytisch berechneten Ergebnissen verglichen.

Acknowledgements

Financial support by the Austrian Federal Government (in particular from Bundesministerium für Verkehr, Innovation und Technologie and Bundesministerium für Wissenschaft, Forschung und Wirtschaft) represented by Österreichische Forschungsförderungsgesellschaft mbH and the Styrian and the Tyrolean Provincial Government, represented by Steirische Wirtschaftsförderungsgesellschaft mbH and Standortagentur Tirol, within the framework of the COMET Funding Programme is gratefully acknowledged.

The studies underlying this thesis have been performed at the Erich Schmid Institute of Materials Science and the Material Center Leoben Forschung GmbH in cooperation with voestalpine Schienen GmbH and voestalpine VAE GmbH.

First of all, I would like express my gratitude to Univ.-Prof. R. Pippan not only because he was my supervisor, but also for his valuable help and fruitful discussions during my scientific work for this thesis. His door was always open for me, also after my time as a scientific employee. His recommendations and valuable critical discussions on results were always supportive and helpful for understanding challenging topics.

Furthermore, I want to thank Univ.-Prof. Antretter from the Institute for Mechanics for his suggestions and helpful solutions regarding challenges in applied mechanics and also finite element simulation related topics during my thesis.

For the opportunity to work on this thesis and the freedom to develop myself during my studies, my thanks go to the Materials Center Leoben Forschung GmbH. My special thanks go to my colleagues Franz, Peter and Toni from the Erich Schmid Institute and Hans-Peter, Jürgen, Masoud and Thomas from the Materials Center Leoben for spending cheerful time after work.

In particular, I would like to thank my girlfriend Marianne for her support and appreciation and for giving me time to undertake my work and studies. She reminds me on the beautiful side of life and shows me a different opinion in difficult situations.

Finally I would like to thank my family, especially my mother for all their support during my whole life, for their persistent help and all the wonderful time we had and still have together.

Table of contents

1. Introduction

1.1. Railway Switches

Railways are commonly used hauling systems all over the world. Depending on the location and application the requirements on the rails are different. Nevertheless, standardized profiles are used. In general, additionally to the main track, railway switches are used to change the direction of a train. In Fig. 1 a switch is schematically plotted, where the stock rail represents the rail for the straight rolling direction and the switch rail is responsible for the direction change.

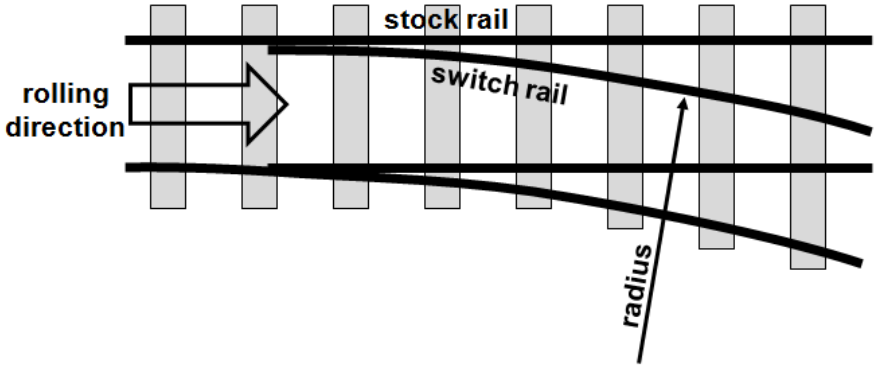

Fig. 1.: Schematic sketch of a railway switch and the distinction of the stock rail and the switch blade.

To force a passing train to change the rolling direction, the switch blade is moved by a mechanism to the stock rail and so the train wheels are switching from the stock rail to the switch blade. Due to the wheel transition from the stock rail to the switch rail and the radius of the switch rail, high dynamic forces are applied on the rails. Hence, switch rails are highly loaded components and require high quality standards.

The stock rail and the switch rail have different profiles, shown in Fig. 2.

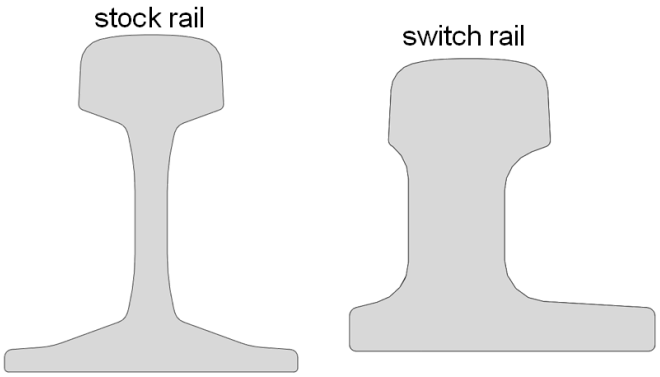

Fig. 2.: Sketch of the profiles indicating the stock and the switch rail.

Due to high loads and the frequency of passing trains, the demand for wear resistance increases and high strength materials have to be adapted. In the literature most of the scientific work focuses on rolling contact fatigue (RCF) between the wheel and the rail head. Nevertheless, neglecting the wheel contact, the highest applied structural stress occurs in the rail foot area due to the bending load.

In this thesis the focus is set on a damage tolerant design concept for the application of high strength materials for railway switches especially for switch rails. The static and dynamic behavior of four different material types with different strength and microstructure is investigated.

- pearlite with a tensile strength of 1070 MPa,
- fine-pearlite with a tensile strength of 1120 MPa,
- bainite with a tensile strength of 1120 MPa,
- ferrite-martensite with a tensile strength of 1510 MPa

For this purpose, for application to railway switches, standard fatigue strength and fracture mechanics methods have been adapted for the static and dynamic assessment [1], [2]. Additionally, new concepts for static failure during the manufacturing process have been investigated by using a fracture mechanics approach [3], [4]. Furthermore an enhanced method for the analytical calculation of the crack growth assuming different loading conditions is provided [5] and the influence of notches on the crack growth from initiation to the end of lifetime has been analyzed [6], [7].

1.2. Stress based damage tolerant design

1.2.1. Endurance limit

Common design concepts use the endurance limit as a safety limit for cyclically loaded components. Fatigue strength diagrams ([8], [9]) are used as a limitation criterion, where the dependency of the applied stress amplitude σ_a or the stress range $\Delta\sigma = 2 \cdot \sigma_a$ is plotted over the mean stress σ_m. In Fig. 3 the Haigh diagram [10] is schematically presented, in which the stress amplitude on the vertical axis is plotted over the mean stress on the horizontal axis. The red line represents the admissible stress amplitude, which is equivalent to the endurance limit $\sigma_{e,0}(R)$, where index "0" denotes a constant applied stress for tension/compression loading. As a static limitation the flow stress $\sigma_{F,0}$ is used, which is the mean value of the yield stress σ_{ys} and the ultimate tensile stress σ_{UTS}.

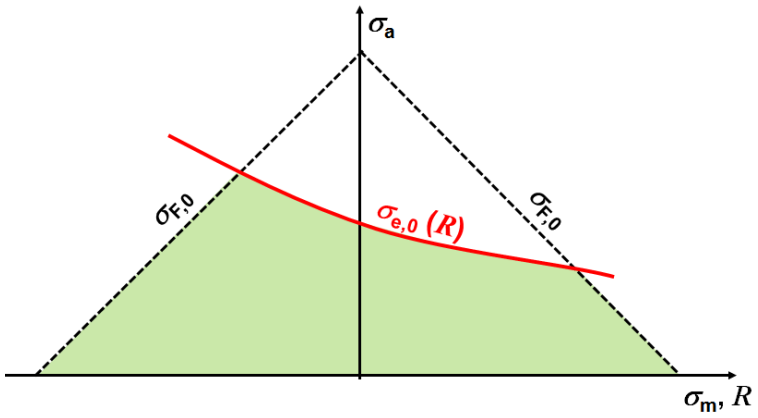

Fig. 3.: Schematic plot of the Haigh diagram; dependency of the stress amplitude on the mean stress.

The dependency of the admissible stress amplitude on the mean stress is often denoted by the stress ratio R, which is proportional to σ_m and can be calculated by the ratio of the minimum σ_{min} and maximum stress amplitude σ_{max}.

$$R = \frac{\sigma_{min}}{\sigma_{max}} = \frac{\sigma_m - \sigma_a}{\sigma_m + \sigma_a} \qquad 1.1$$

The mean stress σ_m or the stress ratio R is changing due to dynamic forces and residual stresses caused by heat treatment and different manufacturing processes also have an influence on the mean stress and stress ratio, respectively.

Amplitudes below the endurance limit, which is marked by the green area in Fig. 3, are considered as safe. The higher the mean stress, the lower is the admissible stress. A lot of different approaches [11], [12], [13] can be found in the literature to describe the dependency of the admissible stress amplitude over the mean stress.

For the damage tolerant design in engineering approaches, the FKM guideline [14] is commonly used. The admissible stress amplitude or the endurance limit is calculated from the static material behavior extracted from tensile experiments.

In Eq. 1.2 the endurance limit $\sigma_{e,0}(R)$, depending on R, is calculated from the ultimate tensile strength σ_{UTS}, reduced by the endurance limit constant f_e, which is depending on the material class (~ 0.4- 0.45 for steel). The dependency of the mean stress is considered by the mean stress sensitivity factor $K_m(R)$.

$$\sigma_{e,0}(R) = \sigma_{UTS} \cdot f_e \cdot K_m(R) \tag{1.2}$$

$K_m(R)$ can be calculated with the FKM guideline, where the mean stress sensitivity is distinguished into three areas and can be calculated with Eq. 1.3, of which the different gradients are shown in Fig. 4.

$$K_m(R) = \begin{cases} \dfrac{1}{1 + M_\sigma \cdot (1+R)/(1-R)} & for \quad R < 0 \\ \dfrac{1}{(1+M_\sigma) \cdot [3 + M_\sigma \cdot (1+R)/(1-R)]} & for \quad 0 < R < 0.5 \\ \dfrac{3 + M_\sigma}{3 \cdot (1+M_\sigma)^2} & for \quad R > 0.5 \end{cases} \tag{1.3}$$

M_σ describes the mean stress sensitivity depending on the ultimate tensile stress σ_{UTS} using the material constants a_m and b_m depending on the material class.

$$M_\sigma = a_m \cdot 10^{-3} \cdot \frac{R_m}{\mathrm{MPa}} + b_m \tag{1.4}$$

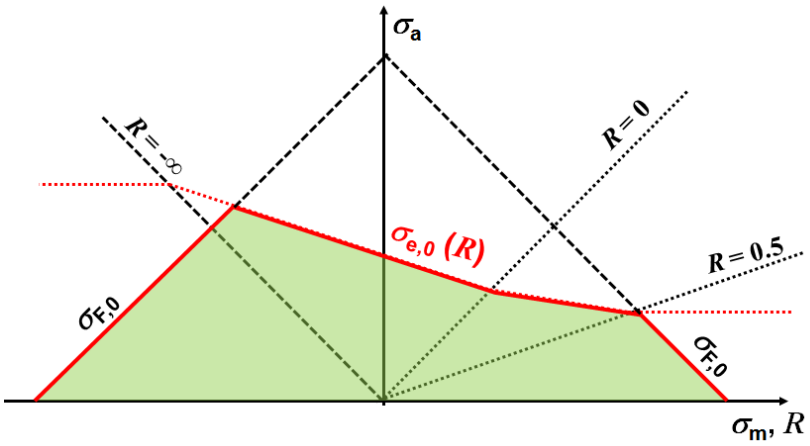

Fig. 4.: Distinction of the endurance limit into areas depending on the mean stress or stress ratio in the Haigh diagram and limited by the flow stress $\sigma_{F,0}$.

In the field of railway engineering a different fatigue strength diagram, the Smith diagram [15] is commonly used and is schematically plotted in Fig. 5. In comparison with the Haigh diagram, the mean stress is tilted by 45° counter clockwise. The red line denotes the minimum (lower) and maximum (upper) endurable stress. The green area is described by the upper and lower endurable stress amplitude and denotes the stress range $\Delta\sigma_{e,0}(R) = 2 \cdot \sigma_{e,0}(R)$.

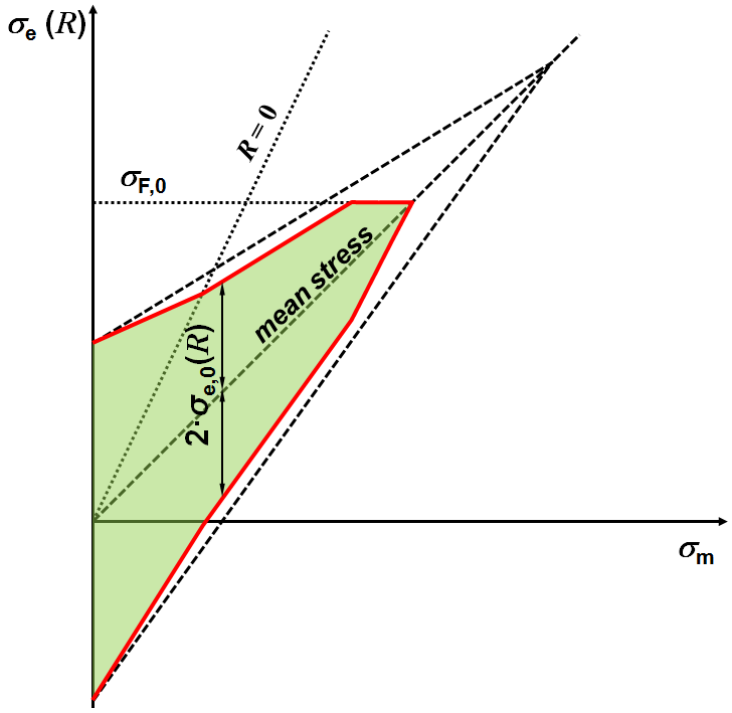

Fig. 5.: Endurable stress amplitude depending on the stress ratio, plotted schematically in the Smith diagram.

As already mentioned, Index "0" denotes a constant stress distribution for tension/compression loading. Nevertheless, rails are loaded in general with a bending load. Due to the different stress gradients, the endurable stress amplitude is higher in case of a bending load than for pure tension/compression. The difference can be considered by including the elastic support factor n_σ for cyclic loading

$$\sigma_{e,bending} = \sigma_{e,0} \cdot n_\sigma \qquad 1.5$$

and the plastic support factor n_{pl} factor for static loading

$$\sigma_{F,bending} = \sigma_{F,0} \cdot n_{pl} . \qquad 1.6$$

Considering notches, the endurance limit is reduced by shape factors and can be found in the literature ([8], [9], [14]) for different approaches. A commonly used approximation for the notch shape factor α_k can be estimated by Eq. 1.7.

$$\alpha_k = 1 + 2 \cdot \sqrt{\frac{t}{\rho}} \,. \qquad 1.7$$

where t represents the notch depth and ρ the notch radius.

Estimating the endurance limit directly from tensile experiments is only valid for polished surface conditions. Due to the rail manufacturing process the surface roughness due to hot rolling can be considered by the surface reduction factor K_{surface} following FKM [14].

$$\sigma_{\text{e,bendingskin}} = \frac{\sigma_{\text{e,0}}}{K_{\text{surface}}} \,. \qquad 1.8$$

The endurance limit as a design criterion is a conservative approach due to an assumed safe area of no damage for an infinite lifetime. In general, notches, surface conditions etc. reduce the endurance limit and hence they are considered by safety factors in standards. Nevertheless, considering very sharp resp. deep notches or rough surfaces, applied loads can exceed acceptable values acc. to standards. In such cases, the endurance limit cannot be used as a design criterion anymore and the fatigue strength has to be considered.

1.2.2. Fatigue strength

The estimation of the lifetime by consideration of the fatigue strength is commonly carried out by the damage cumulative approach of Palmgren and Miner [16], [17].

In Fig. 6 the stress amplitude over the number of cycles N to failure is shown in a log-log plot.

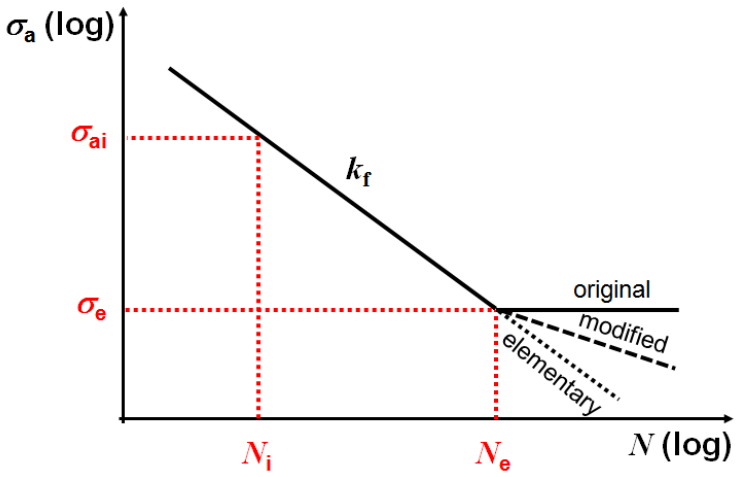

Fig. 6.: Schematic plot to the damage cumulative concept from Palmgren and Miner.

Stress amplitudes σ_{ai} beyond the endurance limit σ_e, can be considered as damage D_i at each cycle N_i. The damage in each cycle D_i is denoted by the reciprocal value of the number of cycles at each cycle ($D_i = 1/N_i$), where $D = \Sigma D_i = 1$ represents the failure of the component. The slope in the fatigue strength is described by the gradient k_f (~ 5 for steel) and the number of cycles N_e at the endurance limit (~10^6 for steel). These two parameters are depending on the material class. The stress over the number of cycles (SN-curve) can then be calculated with the following relationship:

$$N_i \cdot \sigma_{ai}^{k_f} = N_e \cdot \sigma_e^{k_f} . \qquad 1.9$$

Different approaches have been investigated at the intersection point N_e and σ_e. The elementary form of the Miner rule is a simple approach, where the endurance limit is neglected. Nevertheless, this method is too conservative, because every load generates a cumulative damage, even for stresses smaller than the endurance limit which is considered in the original form of the Miner rule like in Fig. 6. However, Haibach [18] investigated a more precise approach for damages in the high cycle fatigue regime ($N > 10^7$), called the modified Miner rule.

1.3. Fracture mechanics design concept

1.3.1. Basics in fracture mechanics

Considering very sharp notches, where the notch radius $\rho \rightarrow 0$, the notch can be assumed as a crack and in front of a crack high stresses are acting, which result in high deformations. In case of an elastic-plastic material behavior, a plastic zone is built up in front of the crack. In the linear elastic fracture mechanics (LEFM), called the regime of small scale yielding, where the size of the plastic zone is small compared to the other dimensions, the stress intensity factor K is used as a crack driving force to describe the stress field in front of the crack tip outside the plastic zone.

$$\sigma = \frac{K}{\sqrt{2 \cdot \pi \cdot r}} \qquad 1.10$$

Where r is the distance from the crack tip and denotes the $1/\sqrt{r}$ singularity [19], shown in Fig. 7.

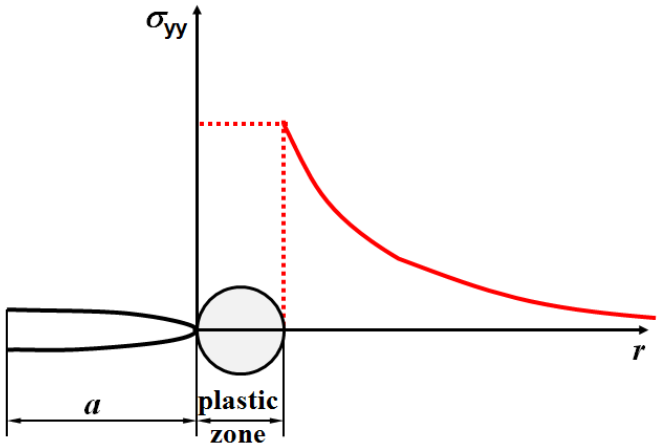

Fig. 7.: Stress distribution in front of the crack denoted by 1/ √ r singularity.

K can be estimated from the applied stress σ_{appl} with

$$K = \sigma_{appl} \cdot Y \cdot \sqrt{\pi \cdot a}\,, \qquad 1.11$$

where a represents the crack length and Y denotes a dimensionless geometry factor which can be found in stress intensity factor handbooks (e.g. [20]).

If the size of the plastic zone is not small compared to the other dimensions, the J-integral can be used as a crack driving force. This is then called the regime of large scale yielding or the field of elastic plastic fracture mechanics (EPFM).

The *J*-integral is calculated by the path independent line integral J_Γ [21].

$$J_\Gamma = \int_\Gamma \left(w dy - T_i \frac{\partial u_i}{\partial x} ds \right) \tag{1.12}$$

where Γ denotes the counter clockwise path from the lower to the upper crack flank, w the strain energy density, T_i the components of traction vector, u_i the displacement vector and ds the incremental length of the path (Fig. 8).

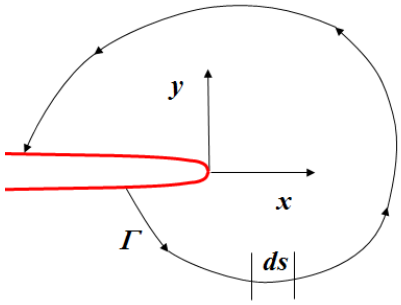

Fig. 8.: Counter clockwise path for the calculation of the *J*-integral.

In the regime of large scale yielding, the stress in front of the crack tip can be calculated by the HRR-field (Hutchinson, Rice and Rosengren) [22], [23] which is depending on the hardening exponent n and the angle θ, shown in Fig. 9.

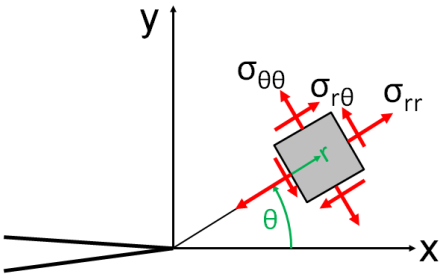

Fig. 9.: Stress element in front of the crack tip.

The stress acting in front of the crack tip can be calculated with

$$\sigma_{ij} = \sigma_0 \cdot \left[\frac{J}{\alpha \cdot \sigma_0 \cdot \varepsilon_0 \cdot I_n \cdot r} \right]^{\frac{1}{n+1}} \cdot \tilde{\sigma}_{ij}(\theta, n) \tag{1.13}$$

$\theta = 0°$ denotes the direction along the crack propagation path and $\theta = 90°$ refers to the normal direction on the crack surfaces. σ_0, ε_0, n and α are the material parameters of the Ramberg-Osgood material law, shown in Eq. 1.14 and can be extracted from tensile experiments.

$$\varepsilon = \frac{\sigma}{E} + \alpha \cdot \varepsilon_0 \cdot \left(\frac{\sigma}{\sigma_0} \right)^n \qquad 1.14$$

The material constants I_n and $\tilde{\sigma}_{ij}(\theta,n)$ have been determined by finite element (FE) simulations from Shih *et al.* (1983) and can be extracted from tables [24] for plane stress and plane strain conditions.

In Fig. 10 three different stress situations are plotted to indicate the different regimes: a) for small scale yielding b) for large scale yielding and c) general or full scale yielding. The red line denotes the stress acting in front of the crack tip, in the crack opening direction over the distance *r* in a log-log plot.

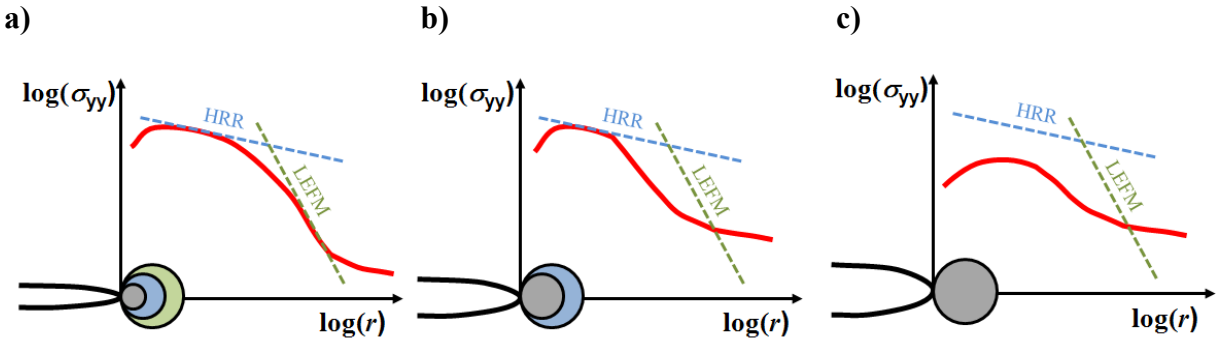

Fig. 10.: Stress distributions acting in front of the crack for different applied stresses, distinction for the *K*-dominated zone in the LEFM, (green), the HRR-field in the regime of large scale yielding (blue) and the large strain region (grey). a) for small scale yielding, b) for large scale yielding and c) full scale or general yielding.

For small loads in a) and a resulting small size of the plastic zone, the LEFM can be used, where *K* describes the stress field in the *K*-dominated zone (green area). Due to the $1/\sqrt{r}$ singularity, the gradient of LEFM stress slope is -1/2 in the log-log plot.

Assuming a higher load in b), will induce a larger plastic zone and *K* cannot be used anymore as a crack driving force. Nevertheless, the HRR-field denoted by *J* in the *J*-dominated zone (blue area) is still valid. Here the gradient of the HHR-slope is due to Eq. 1.13, $-1/(n+1)$.

With increasing load the increasing plastic zone will induce general or full scale yielding. Here, the plastic zone is dominated by the boundaries of the specimen or component. The so called in-plane constraint has to be considered.

In general, the stresses in front of a crack, in the center of the specimen are higher compared to the boundary. Due to the high stress triaxiality in the center, plane strain conditions are assumed, whereas at the surface plane stress conditions are prevalent. The smaller the specimen thickness, the higher is the influence from the surface to the center of the crack which influences the plane strain condition.

Barsom and Rolfe [25] showed the dependency of the critical stress intensity K on the thickness. Different methods have been investigated to consider the geometry dependency, called the constraint. In the field of LEFM the T-stress [26] concept is used to describe this constraint effect. Hence, the $1/\sqrt{r}$ singularity is valid and the stress triaxiality can be modified by the T-stress.

For higher deformations at the crack tip, the J-Q-locus has to be considered, which is part of the EPFM. In this case, the Q-stress [27], [28], [29] is the describing parameter for the J-integral and is defined by the difference between the actual stress field (estimated from FE simulations) and the theoretical solution of the HRR field over the dimensionless distance $r/(J\cdot\sigma_0)$. O'Dowd and Shih [29], [30] tested the Q-parameter in the range $0 < r/(J\cdot\sigma_0) < 5$. In the literature, it is usually recommended to extract the Q-stress at $r/(J\cdot\sigma_0) = 2$.

$$Q = \left.\frac{\sigma_{\theta\theta,\mathrm{FEM}} - \sigma_{\theta\theta,\mathrm{HRR}}}{\sigma_0}\right|_{r=2J/\sigma_0} \tag{1.15}$$

Using the Q-stress, the critical K or J can then calculated with Eq. 1.16, where the Q-stress is depending on the ratio of the crack length and specimen thickness a/W.

$$K = K_{\mathrm{mat}} \cdot \left[1 + \eta \cdot (Q)^h\right] \tag{1.16}$$

where K_{mat} denotes the fracture toughness derived from experiments; η and h are material constants to describe the constraint dependency.

1.3.2. Static fracture

1.3.2.1. Experimental determination of *K*

In contradiction to general stress based designs, where the yield stress, the ultimate strength or the fracture strain is used as a design criterion, the fracture toughness from experiments is not proportional to the static strength due to a different fracture mechanism. Standards [31], [32], [33] provide different test methods depending on the loading and the geometry for the fracture toughness. In general for a valid experimentally determined fracture toughness K_{Ic} , where the index "I" denotes the crack in Mode I [19], the dimensions have to fulfil the following criterion:

$$a, b, B \leq 2.5 \cdot \left(\frac{K_I}{\sigma_{ys}} \right)^2 \tag{1.17}$$

where a is the crack length, b the ligament length ($b = W - a$) and B is the specimen thickness. This criterion ensures that the fracture toughness is independent of geometry effects.

1.3.2.2. Experimental determination of *J*

Compared to K, the experimental determination of the J-integral is more challenging. It is recommended in standards [33] or can be estimated by additional FE simulation using Eq. 1.12. Only in case of small scale yielding in the field of LEFM, J can be calculated from K by using

$$J_{el} = \frac{K_{Ic}^{\ 2}}{E} \cdot \left(1 - \nu^2\right) \tag{1.18}$$

in a plane strain state.

For short cracks ($a << W$) Shih and Hutchinson [34] and enhanced by Dowling [35] suggested an analytical estimation of the J-integral from the experimental data, where J is calculated from the strain energy density w. Dowling [35] showed an acceptable correlation between the experimental data and an analytically calculated J-integral, using this method.

Dowling`s approach by application of pre-factors implies a semi-circular crack in plane stress state. For a more general investigation in plane strain conditions the approach from Dowling has to be adapted. It was investigated in [3], [4] and is explained below.

The *J*-integral is split into an elastic and a plastic part:

$$J = J_{el} + J_{pl}. \tag{1.19}$$

J_{el} can be calculated from the true stress-strain curves using the strain energy density w_{el} in the plane strain state and a trough thickness crack.

$$J_{el} = 2 \cdot \pi \cdot a \cdot Y\left(\frac{a}{W}\right)^2 \cdot \left(1 - \nu^2\right) \cdot w_{el} \tag{1.20}$$

with

$$w_{el} = \frac{\sigma \cdot \varepsilon_{el}}{2} = \frac{\sigma^2}{2 \cdot E} \tag{1.21}$$

where σ in combination with ε_{el} represents the true stress and strain in the linear elastic regime and $Y(a/W)$ denotes the geometry function.

The plastic part of the *J*-integral can be calculated in a similar way by inserting w_{pl} instead of w_{el} into Eq. 1.20

$$J_{pl} = 2 \cdot \pi \cdot a \cdot Y^2 \cdot \left(1 - \nu^2\right) \cdot f(n) \cdot w_{pl} \tag{1.22}$$

where w_{pl} denotes the plastic work and $f(n)$ a plastic correction factor depending on the strain hardening exponent n from Eq. 1.14, provided by Shih and Hutchinson [34] and can be calculated for the approach in Eq. 1.22 with

$$f(n) = \left[3.85 \cdot \sqrt{n}\left(1 - \frac{1}{n}\right) + \frac{\pi}{n}\right] \cdot \frac{n+1}{2 \cdot \pi \cdot (n-1)}. \tag{1.23}$$

The plastic work w_{pl} beyond the yield stress has to be derived from the true stress strain curves using the Ramberg Osgood material law (Eq. 1.14).

$$w_{pl} = \int \sigma \cdot d\varepsilon_{pl} = \int \left[\frac{\varepsilon_{pl}}{\alpha \cdot \varepsilon_0} \cdot {\sigma_0}^n\right]^{1/n} \cdot d\varepsilon_{pl} \tag{1.24}$$

$$w_{pl} = \left[\frac{{\sigma_0}^n}{\alpha \cdot \varepsilon_0}\right]^{1/n} \cdot \frac{n}{1+n} \cdot {\varepsilon_{pl}}^{\frac{1+n}{n}} = \sigma \cdot \varepsilon_{pl} \cdot \frac{n}{1+n} \tag{1.25}$$

The plastic part of the *J*-integral can then be calculated from Eqns. 1.22 and 1.25.

$$J_{\mathrm{pl}} = 2 \cdot \pi \cdot a \cdot Y\left(\frac{a}{W}\right)^2 \cdot \left(1-\nu^2\right) \cdot \sigma \cdot \varepsilon_{pl} \cdot \frac{n}{1+n} \cdot f(n) \qquad 1.26$$

To determine the *J*-integral, this method is quite useful as the experimental data can be used directly from the measured stress strain curve.

1.3.2.3. Damage tolerant concepts for static fracture

Using the information of the material and fracture characteristics, a failure curve can be constructed and then compared with the nominal applied stress or strain at failure which can be derived from experimental data. For designing a failure curve by using fracture mechanics criteria, several different approaches are provided depending on the material type and damage behavior. The failure assessment diagram (FAD) is a widely used approach in failure analysis like in the R6 method [36], [37], [38]. In this diagram, the limiting parameters L_r and K_r are used as follows:

$$L_\mathrm{r} = \frac{\sigma_{\mathrm{ref}}}{\sigma_\mathrm{y}} \qquad 1.27$$

$$K_\mathrm{r} = \frac{K}{K_{\mathrm{mat}}} = \sqrt{\frac{J}{J_{\mathrm{mat}}}} \qquad 1.28$$

where again K_{mat} represents the fracture toughness.

The failure curve can then be calculated by different approaches e.g. an empirical formulation in combination with the strip yield assumption [37], [38].

$$f(L_\mathrm{r}) = \left[1+0.5 \cdot {L_\mathrm{r}}^2\right]^{-1/2} \cdot \left[0.3+0.7 \cdot \exp\left(-0.6 \cdot {L_\mathrm{r}}^6\right)\right] \qquad 1.29$$

Nevertheless, the influence of the material behavior on the failure curve is negligible. Option 2 in the R6 approach considers the true stress-strain curve [19].

$$f(L_\mathrm{r}) = \left[\frac{E \cdot \varepsilon_{\mathrm{ref}}}{\sigma_{\mathrm{ref}}} + \frac{1}{2} \cdot \frac{\left(\sigma_{\mathrm{ref}}/\sigma_{\mathrm{ys}}\right)^2}{E \cdot \varepsilon_{\mathrm{ref}}/\sigma_{\mathrm{ref}}}\right]^{-1/2} \quad \text{for} \quad 0 \le L_\mathrm{r} \le {L_\mathrm{r}}^{\max} \qquad 1.30$$

where ${L_\mathrm{r}}^{\max}$ is defined by the relation of the yield and ultimate tensile stress.

$${L_\mathrm{r}}^{\max} = \frac{1}{2} \cdot \frac{\sigma_{\mathrm{ys}} + \sigma_{\mathrm{UTS}}}{\sigma_{\mathrm{ys}}} \qquad 1.31$$

Nevertheless, those methods only consider small scale yielding. In the regime of large scale yielding, the geometry dependency, especially for small a/W-ratios, has to be considered by the Q-stress. Betegòn [39], [40] investigated a potential function to describe the failure curve of the critical J-integral for different a/W ratios, where J is up to 6 times higher than the fracture toughness J_{mat}.

Using the Q-stress, a constraint-based diagram can be designed [41], [42] by increasing the critical K-value in the form of a potential function depending on the crack length. In the literature mostly the following approach is recommended to describe the increasing fracture toughness [37], [38], [41], cf. Eq. 1.16.

$$K = K_{mat} \cdot \left[1 + \eta \cdot \left(-\beta \cdot L_r\right)^h\right] \tag{1.32}$$

where η and h are material constants and β implies the constraint using the Q-stress by

$$Q = \beta \cdot L_r \tag{1.33}$$

Instead of using the stress as a failure criterion, the strain can be used in a similar approach as for the stress based R6 procedure, e.g. [44], [43]. In this case, the parameter L_r is exchanged by D_r.

$$D_r = \frac{\varepsilon_{ref}}{\varepsilon_{ys}} \tag{1.34}$$

where ε_{ref} denotes the nominal strain of the un-cracked specimen and ε_{ys} the strain at the yield stress.

Similar to the stress based approach, different options are investigated for the strain based failure curve. Details are shown in Budden and Ainsworth [43] where the advantages of the different approaches are worked out.

For small scale yielding Budden [44] provided a strain based failure curve for two regions, equal to the stress-based failure line:

$$f^*\left(D_r\right) = \begin{cases} \left[1 + \frac{1}{2} \cdot D_r^{\,2}\right]^{-1/2} & \text{for} \quad D_r < 1 \\ f^*(1) \cdot D_r^{\,-1/2} & \text{for} \quad D_r \geq 1 \end{cases} \tag{1.35}$$

Nevertheless, this is not conservative for high deformations. Therefore, for large D_r the following equation (strain based FAD option 2) is used:

$$f^*(D_r)=\begin{cases}\left[\dfrac{E\cdot\varepsilon_{ref}}{\sigma_{ref}}+\dfrac{1}{2}\cdot\dfrac{\left(\sigma_{ref}/\sigma_{ys}\right)^3}{E\cdot D_r}\right]^{-1/2} & \text{for} \quad D_r<1\\ \left[\dfrac{2\cdot D_r}{\sigma_{ref}/\sigma_{ys}}\right]^{-1/2} & \text{for} \quad D_r>1\end{cases} \tag{1.36}$$

Another approach is called Option 3, where Budden [44] proposed to use directly the *J*-integral from finite element (FE) simulations.

$$f^*(D_r)=\sqrt{\frac{J_{el}}{J}} \tag{1.37}$$

The R6 method and strain based failure assessment diagram is an established approach to describe the static failure in fracture mechanics. Furthermore, by considering the constraint due to small *a*/*W*-ratios, a constraint based diagram can be designed.

1.3.3. Fatigue fracture

Similar to the static fracture the stress intensity is used as a crack driving force for cyclically loaded components. Following Paris [45], [46] and Rice [47], the stress intensity factor range ΔK of the crack is used to describe the crack propagation.

$$\Delta K = Y \cdot \Delta\sigma \cdot \sqrt{\pi \cdot a} \qquad 1.38$$

where $\Delta\sigma$ denotes the applied stress range and denotes $2 \cdot \sigma_a$.

1.3.3.1. Damage tolerant concepts for fatigue fracture

In fracture mechanics, for cyclically loaded components, the Kitagawa-Takahashi diagram [48] is commonly used as a design criterion. It represents a similar approach as the Smith diagram, already explained in chapter 1.2.1. In the Kitagawa-Takahashi diagram the admissible stress range $\Delta\sigma$ of cyclically loaded components is plotted as a function of the crack length a (Fig. 11).

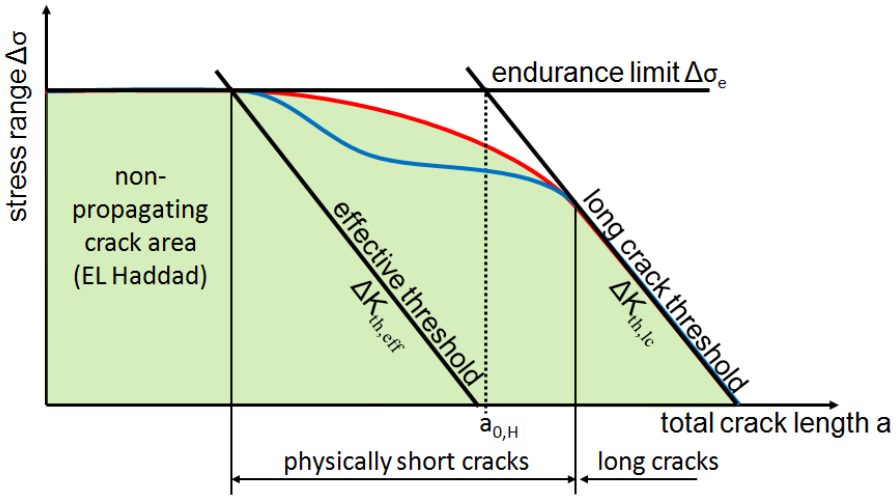

Fig. 11.: Schematic plot of the endurable stress range $\Delta\sigma$ depending on the crack length (Kitagawa-Takahashi diagram) [1].

Considering un-cracked components or micro structural short cracks the endurance limit can be used as limitation, like in the Smith diagram. For long cracks the admissible stress range is denoted by the long crack threshold $\Delta K_{th,lc}$. Beyond $\Delta K_{th,lc}$, considering a constant applied stress range, cracks will grow until failure. Furthermore, the green area in Fig. 11 represents stress range and crack length combinations where cracks do not propagate.

The red line denotes the transition from the endurance stress range $\Delta\sigma_e$ to the long crack threshold and was first used by El-Haddad [49] by introducing an intrinsic crack length $a_{0,H}$.

Furthermore, in Fig. 11, the parallel slope to the long crack threshold denotes the effective (intrinsic) threshold $\Delta K_{th,eff}$ (~2.5 MPa√m for steel), which constitutes the limit for crack propagation. This means for loads below $\Delta K_{th,eff}$ no crack propagation takes place. Between the long crack and the effective threshold, the crack growth threshold depends on the build-up of crack closure. The blue line represents the transition from the effective to the long crack threshold and was presented by Tabernig [50]. Maierhofer [51] proposed a modified description by a double exponential function (Eq. 1.39), where each summand characterizes a different closure mechanism.

$$\Delta K_{th} = \Delta K_{th,eff} + (\Delta K_{th,lc} - \Delta K_{th,eff}) \cdot \left[1 - \sum_{i=1}^{2} v_i \cdot \exp\left(-\frac{\Delta a}{l_i} \right) \right] \qquad 1.39$$

where l_i and v_i denote fit parameters.

The cyclic resistance curve (R-curve) describes the short crack growth and is represented by a different closure mechanism ([52], [53], [54]), depending on the material behavior. The R-curve is schematically plotted in Fig. 12 and distinguishes between an effective threshold, a contribution from plasticity induced and a roughness induced crack closure. While the plasticity induced closure effect depends on the plastic properties, the roughness induced closure effect is related to the microstructure.

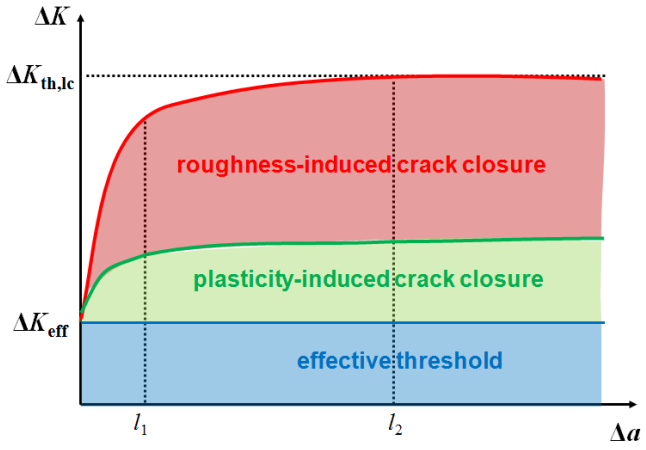

Fig. 12.: Illustration of the crack resistance curve caused by two different closure mechanisms; each closure mechanism is built up completely after a specific crack extension (described by the fictitious length scales l_i) [51].

The crack tip loading is a function of the total crack length $a = a_0 + \Delta a$, where a_0 denotes the initial crack length assuming no closure effects [55] and Δa the crack extension where closure effects are built up by Eq. 1.39.

Moreover, not only the endurance limit $\Delta\sigma_e$, also the long crack threshold $\Delta K_{th,lc}$ is depending on the stress ratio R. The dependency of the $\Delta K_{th,lc}$ on R can be estimated by a bi-linear approximation with Eq. 1.40 [51].

$$\Delta K_{th,lc}(R) = \begin{cases} \Delta K_{th,lc(R=0)} \cdot (1-R) & \text{for} \quad \Delta K_{th,lc(R=0)} \cdot (1-R) > \Delta K_{th,eff} \\ \Delta K_{th,eff} & \text{for} \quad \Delta K_{th,lc(R=0)} \cdot (1-R) \leq \Delta K_{th,eff} \end{cases} \tag{1.40}$$

The higher R, is the lower is the endurance limit and the long crack threshold. Due to a linear relationship between the threshold for long cracks and the load ratio, the range for any stress intensity factor can be calculated.

The admissible stress range $\Delta\sigma$ depends therefore on three variables, Δa, a_0 and R ([1], [2]).

$$\Delta\sigma(\Delta a, R, a_0) = \min\left(\frac{\Delta K_{th}(\Delta a, R)}{Y \cdot \sqrt{\pi \cdot (a_0 + \Delta a)}}, \Delta\sigma_e(R) \right) \tag{1.41}$$

Eq 1.41 describes a three-dimensional surface for each stress ratio R, which is shown in Fig. 13. Each surface represents the admissible stress range depending on the crack extension Δa, the initial crack (notch) depth a_0 where each surface denotes a different load ratios R.

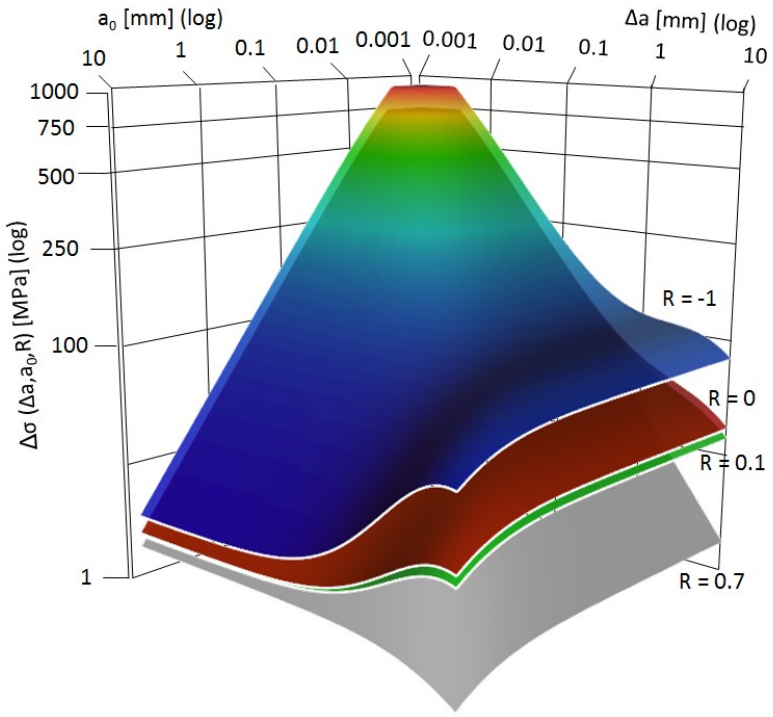

Fig. 13.: Three-dimensional plot of admissible stress range $\Delta\sigma$ depending on a_0, Δa, R [2].

1.3.3.2. Crack growth modelling for cyclically loaded components

For stress and crack length combinations beyond the area of no crack propagation in the Kitagawa-Takahashi diagram (cf. Fig. 11), cracks will grow until failure. The NASGRO equation is commonly used to describe the crack growth behavior of cyclically loaded components and different approaches can be found in literature [53], [56]. Maierhofer [51] provided a modified NASGRO equation in consideration of the crack resistance of physically short cracks (R-curve), depending on the stress ratio R and the crack extension Δa.

$$\frac{da}{dN} = C \cdot F(R,\Delta a) \cdot \Delta K^{m-p} \left(\Delta K - \Delta K_{th}(R,\Delta a)\right)^{p} \qquad 1.42$$

$\Delta K_{th}(R, \Delta a)$ is denoted by the dependency of R. Additional to the commonly used parameters C and m in the Paris slope ([57], [58]), illustrated in Fig. 14, the constant p governing the transition from the near-threshold stage to the Paris slope of crack growth is included.

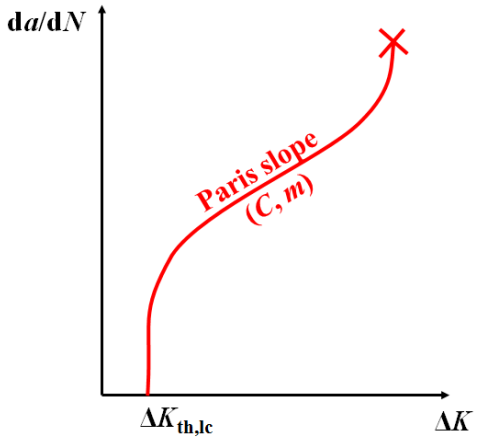

Fig. 14.: Schematical plot for the long crack behavior and the Paris slope characterized by the parameters C and m.

The crack velocity factor

$$F(R,\Delta a) = 1 - \left[1 - \left(\frac{1 - f(R)}{1 - R}\right)^{m}\right] \cdot \left[1 - \sum_{i=1}^{n} v_i \cdot \exp\left(-\frac{\Delta a}{l_i}\right)\right], \qquad 1.43$$

is depending on the stress ratio R, the built up of crack closure (R-curve) and Newman's crack opening function $f(R)$.

$$f(R)=\begin{cases}\max(R;A_0+A_1\cdot R+A_2\cdot R^2+A_3\cdot R^3, & R\geq 0\\ A_0+A_1\cdot R, & -2\leq R<0\\ A_0-2\cdot A_1, & R<-2\end{cases} \quad 1.44$$

The parameters can be calculated with

$$A_0=\left(0{,}825-0{,}34\cdot\alpha_N+0{,}05\cdot{\alpha_N}^2\right)\cdot\left[\cos\left(\frac{\pi\cdot\sigma_{max}}{2\cdot\sigma_F}\right)\right]^{1/\alpha} \quad 1.45$$

$$A_1=\left(0{,}415-0{,}071\cdot\alpha_N\right)\cdot\frac{\sigma_{max}}{\sigma_F} \quad 1.46$$

$$A_2=1-A_0-A_1-A_3 \quad 1.47$$

$$A_3=2A_0+A_1-1, \quad 1.48$$

where the ratio of the maximum applied stress and the flow stress σ_{max}/σ_F = 0.3 and α_N=3.0 for plane strain conditions.

1.3.3.3. Experimental determination of the R-curve and NASGRO parameters

The determination of the crack resistance curve for physically short cracks and the long crack growth behavior beyond $\Delta K_{th,lc}$, requires a number of fracture mechanics experiments. Therefore, SENB (single edge notched bending) specimens with a specimen height W = 20 mm, specimen thickness B = 6 mm and a length L = 100 mm are tested at different stress ratios R, each in a four-point bending device, shown in Fig. 15.

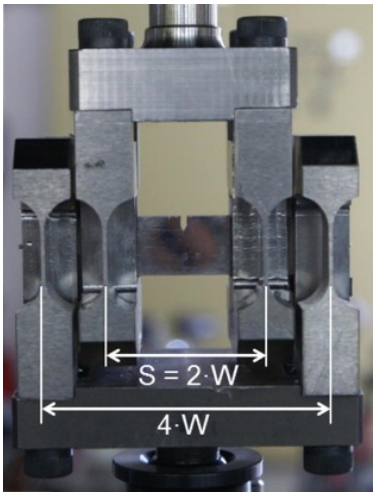

Fig. 15.: SENB specimen in a four point bending device [55].

A notch is eroded on one side and sharpened by a razor blade. Following this, a pre-crack is induced by compression loading [59]. The cyclic fracture behavior is then tested by the load increasing method, where the load is increased in a stepwise manner (shown in Fig. 16). At each load when the crack arrests, a point on the crack resistance curve for ΔK_{th} can be obtained.

Furthermore, for loads beyond the long crack threshold ($\Delta K > \Delta K_{th,lc}$) no further increase of the crack closure effects occurs and the crack propagates until failure.

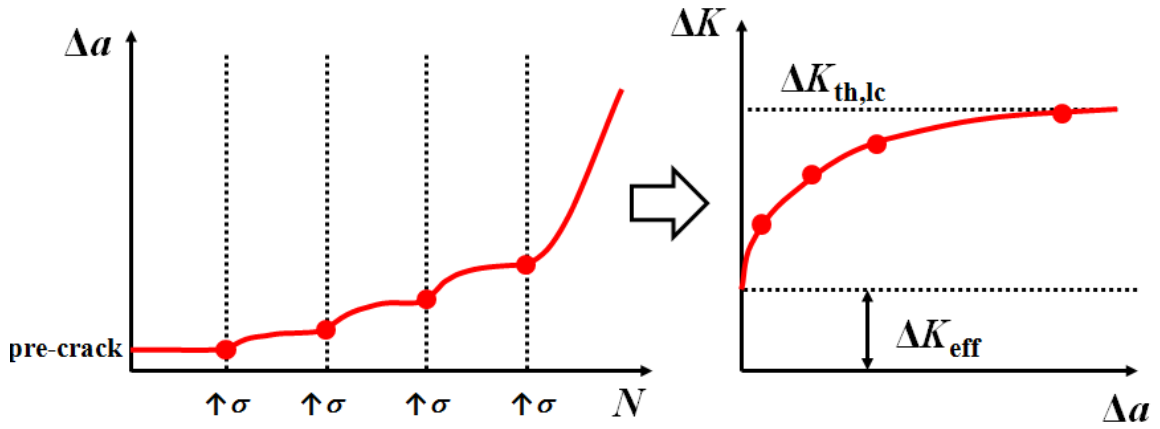

Fig. 16.: Load increasing method to determine the cyclic crack resistance curve for ΔK_{th} device [50].

To obtain the crack length, the direct current potential drop (DCPD) method with the formulation of Johnson [60] and Schwalbe [61] is used.

2. Damage tolerance design for the manufacturing process

The application of high strength materials poses new challenges for the manufacturing process, especially in bending the curvature radius which has been worked out in [3] and is presented in this section. The applied load during bending – as a central element of the manufacturing process for switches – is about ten times higher than the typical load observed during a train passage. As a characteristic quantity for the bending process one can take the strain at the outer fiber of the component. Consequently, commonly used rail standards prescribe a minimum rupture strain of 8-9% in the tensile test. It is understood that the standard tensile specimens have a ground and polished surface, whereas the finishing of the rail surface is much coarser; due to the surface roughness and flaws generated during processing – which acts much the same as small surface flaws – the actual rupture strain for the rail will be lower than for the standard specimen. For this reason, the tensile properties generally do not represent a design criterion but an acceptance criterion for rail production.

In order to analyze the fracture behavior and to design a failure curve of the nominal strain in the outer fiber depending on the size of such surface flaws, three-point bending specimens with surface cracks of varying lengths have been manufactured from four typical rail materials with different microstructures and have then been tested until fracture. A comparison of fracture mechanics estimation with experimental results will be performed in order to deliver a simple failure criterion for the bending process.

2.1. Materials

The different material hardening behaviors are specified by the Ramberg-Osgood material law (Eq. 1.14).

The parameters σ_0, ε_0, n and α are determined by a statistical analysis from the true stress-strain curves of the tensile experiments. The material parameters describing these curves are listed in Table 1 and the resulting true stress-strain curves are plotted in Fig. 17.

Table 1: Ramberg-Osgood parameters

material	n **[-]**	α **[-]**	σ_0 **[MPa]**	ε_0 **[-]**
pearlite	4.56	0.1329	316	0.001497
fine-pearlite	3.82	0.1872	302	0.001465
bainite	9.18	0.1207	685	0.003567
ferrite-martensite	12.55	0.0321	944	0.004796

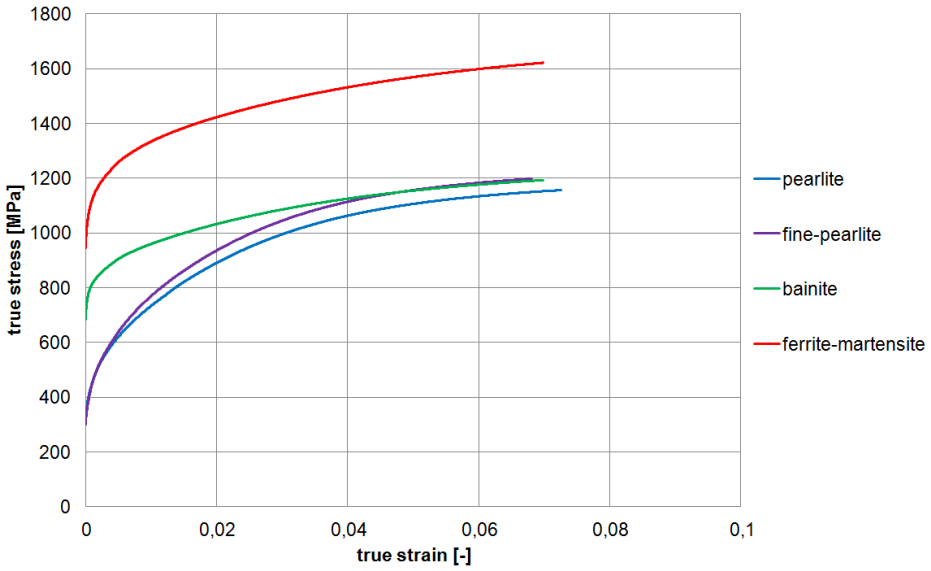

Fig. 17.: Results of the tension experiments in the true stress-strain diagram.

2.2. Experimental determination of the failure curve

For the determination of the failure curve, the fracture toughness of four different materials with different strengths is tested in a three-point bending support (Fig. 18). The specimen has a height $W = 20$ mm and a thickness $B = 10$ mm; the distance $2 \cdot s$ between the supports is 200 mm. On one side of the specimen a notch is eroded and sharpened by a razor blade. Then a pre-crack is generated by cyclic compression loading in a four-point bending support using a load ratio of $R = -10$ [59]. The total crack length a varies from about 8 to 0.1 mm; in addition a specimen with ground surface without crack is tested for each material for comparison of the numerical model and material behavior. The specimens are loaded by a force in the center of the specimen by the upper cylinder until rupture. During the experiment the deflection v (load line displacement) is measured. In this way, a force *vs.* deflection curve is obtained.

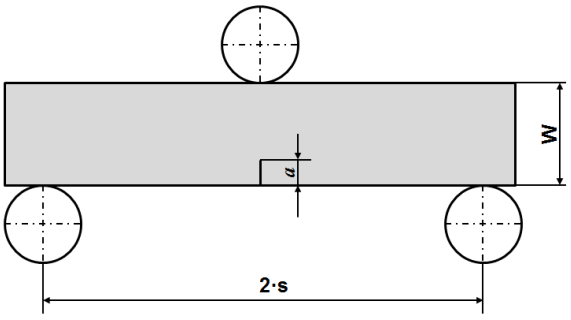

Fig. 18.: Schematic of the three-point bending test.

To obtain the crack length, the fracture surface is characterized in the optical microscope after the test. This is shown exemplarily in Fig. 19, where the total crack length a is composed of the depth of the eroded notch and the initiated pre-crack generated by compression loading.

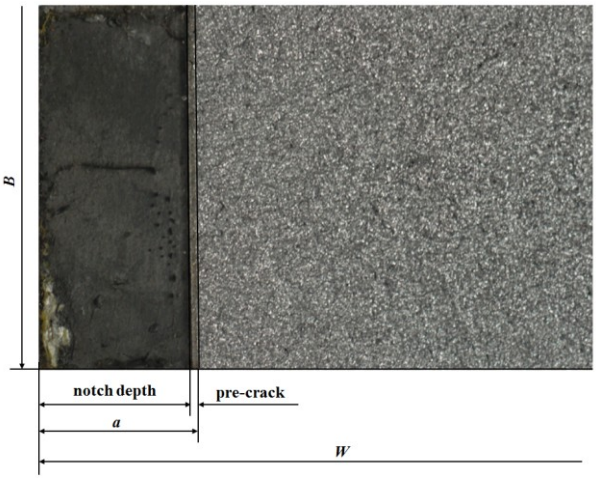

Fig. 19.: Exemplary fracture surface; distinction of notch depth and pre-crack length for the extraction of the crack length *a*.

2.3. Determination of the failure strain in a static strain based Kitagawa-Takahashi type diagram

FAD diagrams presented in chapter 1.3.2.3 are used to describe the static failure by a fracture mechanic approach. However, the influence of the parameters K_r, L_r or D_r in the R6 method are difficult to understand in the field of engineering. In order to design a direct link between the nominal strain in the outer fiber of an un-cracked specimen and the failure size, a direct approach more suitable for mechanical engineering applications comes to mind; namely, to generate a direct relation between the nominal strain at failure and the crack length *a*. This approach is, in a certain sense, the static strain based equivalent to the Kitagawa-Takahashi diagram for the fatigue endurance limit stress of cracked specimens. We will therefore refer to this diagram as the "static strain based Kitagawa-Takahashi diagram" in what follows.

For plotting this diagram, the nominal strain at the outer fiber upon failure has to be determined. In our study, it is computed by means of FE simulations.

Using the hardening behavior from the tensile tests, a three-dimensional FE simulation of the bending experiment is performed for an un-cracked specimen. The specimen is loaded with the maximum force F_{max} from the experiment so that the nominal failure strain at the outer fiber can be extracted. The numerical model is shown in Fig. 20, where the symmetry of the bending specimen is used and a quarter symmetric model is generated. The force is applied by an analytical rigid cylinder with a radius of 30 mm, the same is used for the support on the lower side of the specimen. A penalty surface-to-surface contact with a friction coefficient of 0.1 is used between the rigid cylinders and the specimen. The finite element program ABAQUS is used with large deformations.

For meshing the specimen, 20 node elements with a quadratic shape functions and a global element size of maximum 1 mm are used. Additionally a refinement in the area of interest, the center of the specimen with an element size of 0.1 mm was generated. In this way, the error of the extracted strain is kept as small as possible.

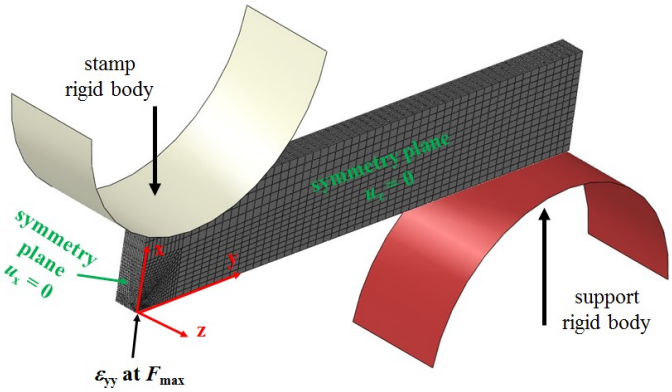

Fig. 20.: Numerical model extracting the maximum strain in crack opening direction ε_{yy}. Additionally, the boundary conditions with the symmetry planes and the rigid bodies representing the support and the stamp for the applied force are shown.

To validate the numerical model, the applied force and resulting deflection are compared with the experimental force-deflection curve of the un-cracked specimen. In Fig. 21 the experimental results in comparison with the numerical simulation are exemplarily shown for the pearlitic material, where the markers denote the experiments at failure.

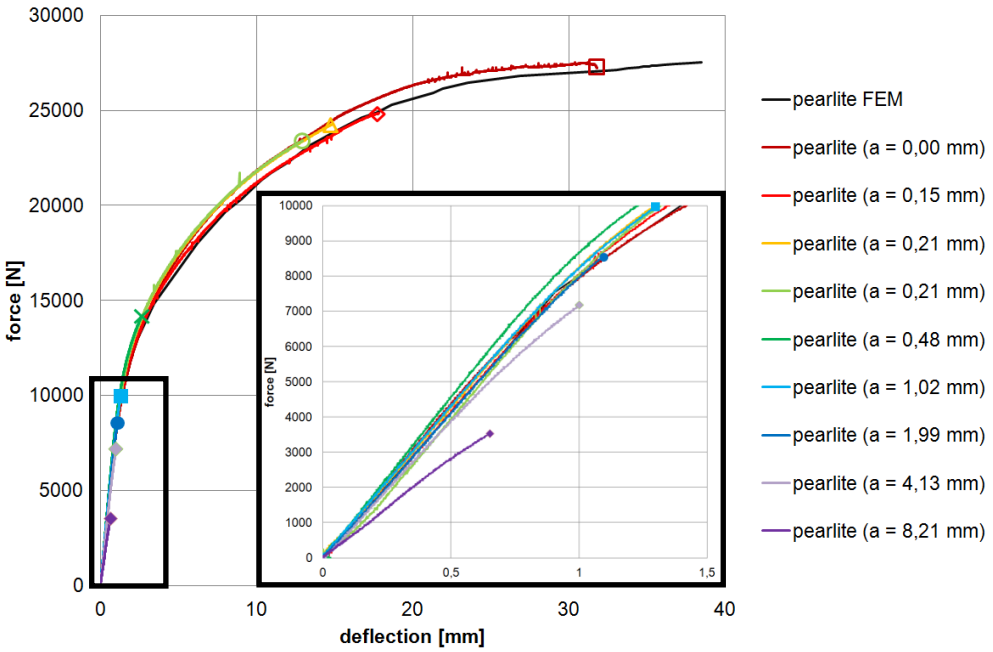

Fig. 21.: Exemplary force-deflection curves of the experiments with different crack lengths in comparison with numerical simulation without a crack for the pearlitic steel. In the insert the force-displacement curves for smaller deflections are shown.

The nominal strain at failure can now be plotted against the crack length in a log-log plot (Fig. 22). Looking at the experimental results, the diagram can be roughly divided into two regions with different gradients of the failure line.

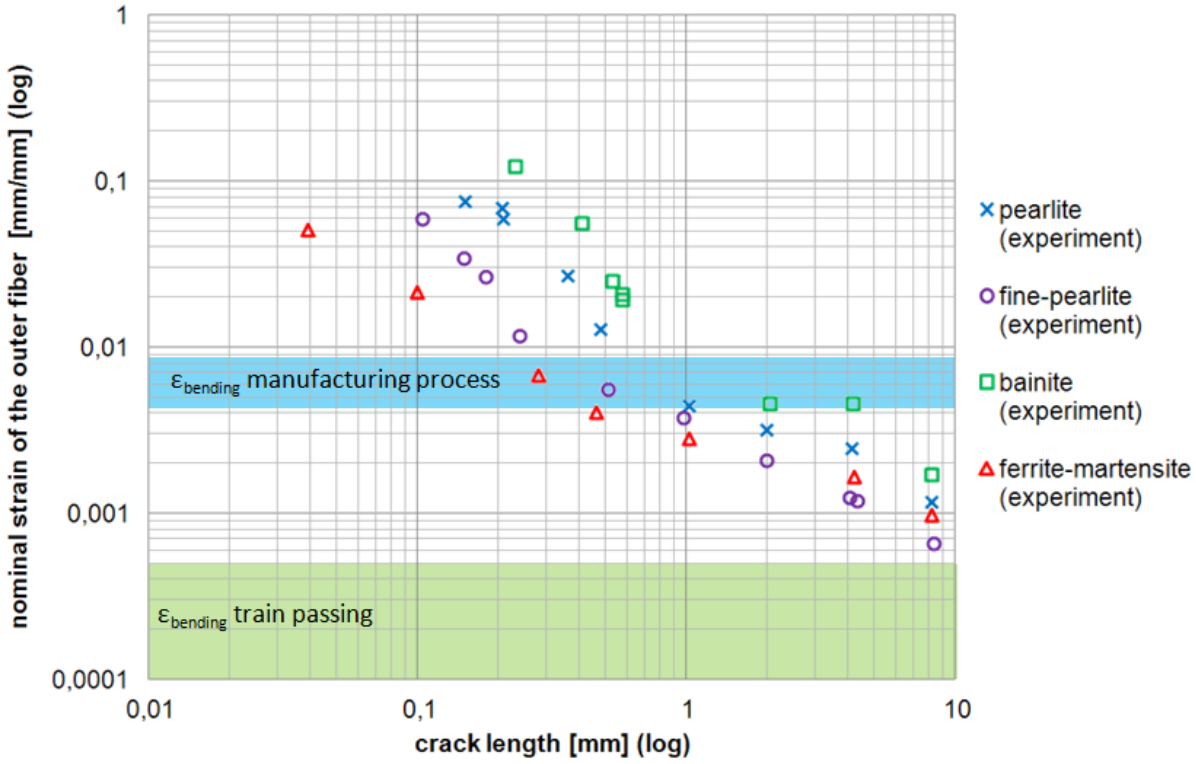

Fig. 22.: Nominal strain at failure at the outer fiber (calculated by numerical simulation using the maximum load from the experiments) against the crack length. Additionally typical strains are displayed for the bending process and when a train is passing the switch.

The theoretical approach is shown in Fig. 23; a distinction into two regions can be explained by the validity of linear-elastic fracture mechanics (LEFM, grey area) and the *K*-concept for long cracks down to a certain transition length a_{pl}, from where on the *J*-concept of elastic-plastic fracture mechanics (EPFM, green area) has to be used. For even shorter cracks the fracture strain is nearly equivalent to the strain of un-cracked and polished specimens (left area).

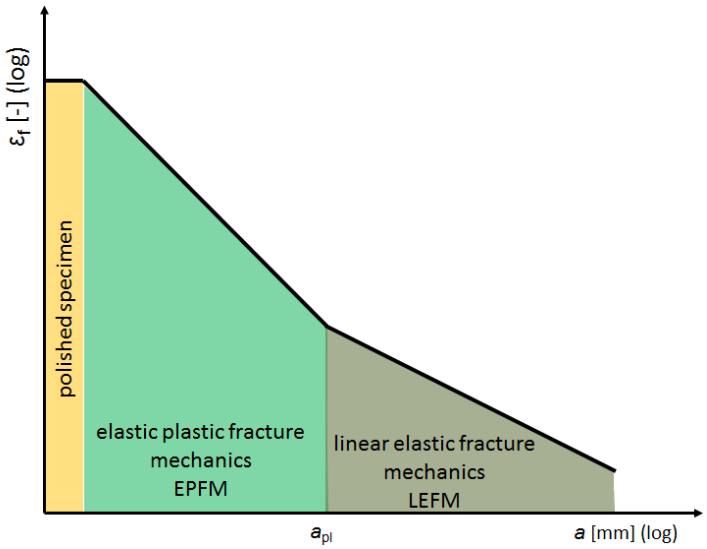

Fig. 23.: Schematic of theoretical approach for the failure strain in the static strain based Kitagawa-Takahashi diagram.

To calculate the failure curve in the LEFM area, the stress intensity factor K from Eq. 1.11 is equated to the fracture toughness K_{Ic},

$$K = \sigma_b \cdot \sqrt{\pi \cdot a} \cdot Y\left(\frac{a}{W}\right) = K_{Ic} \,. \tag{2.1}$$

The geometry factor $Y(a/W)$ is estimated from the function $f(a/W)$,

$$Y\left(\frac{a}{W}\right) = \frac{2}{3} \cdot \sqrt{\frac{W}{\pi \cdot a}} \cdot f\left(\frac{a}{W}\right) \tag{2.2}$$

with the geometry function $f(a/W)$ for the three-point bending specimen [62]

$$f(a/W) = \frac{3 \cdot (a/W)^{1/2} \cdot \left[1.99 - (a/W) \cdot (1 - a/W) \cdot \left(2.15 - 3.93 \cdot a/W + 2.7 \cdot a^2/W^2\right)\right]}{2 \cdot (1 + 2 \cdot a/W) \cdot (1 - a/W)^{3/2}} \,. \tag{2.3}$$

In consideration of linear-elastic material behavior (Hooke´s law), $\sigma = E \cdot \varepsilon$, the fracture strain $\varepsilon_{f\text{-}LEFM}$ can be obtained from Eq. 2.1 as

$$\varepsilon_{f-LEFM} = \frac{K_{Ic}}{\sqrt{\pi \cdot a} \cdot E \cdot Y\left(\frac{a}{W}\right)} \,. \tag{2.4}$$

Due to the fact that the fracture toughness K_{Ic} and Young´s modulus E are constants, one obtains a slope of -1/2 in the log-log diagram of fracture strain *vs.* crack length,

$$\log(\varepsilon_{f-LEFM}) \propto -\frac{1}{2}\cdot\log(a) - Y\left(\frac{a}{W}\right). \qquad 2.5$$

For short cracks, $a < a_{pl}$, the *K*-concept is not valid anymore, and the *J*-integral has to be used as a fracture criterion. The critical *J*-integral can be calculated based on the strain energy density *w* [34], [35], for J_{pl} with Eqns. 1.22 and 1.23.

Finally the plastic strain ε_{pl} can then be expressed by Eq. 1.22 and 1.23. Due to the assumed integration limits where plastic strain starts at $\varepsilon_{pl} = 0$, the elastic strain energy density w_{el} at the yield point ε_0 has to be subtracted:

$$\varepsilon_{pl} = \varepsilon_{f-LEFM} = \left\{\left[\frac{J_c}{2\cdot\pi\cdot a\cdot Y\left(\frac{a}{W}\right)^2\cdot\left(1-\nu^2\right)} - w_{el}(\varepsilon_0)\right]\cdot f(n)\cdot\left[\frac{\alpha\cdot\varepsilon_0}{{\sigma_0}^n}\right]^{1/n}\cdot\frac{(1+n)}{n}\right\}^{\frac{n}{1+n}} \qquad 2.6$$

where $w_{el}(\varepsilon_0)$ is derived from Eq. 1.21,

$$w_{el}(\varepsilon_0) = \frac{{\varepsilon_0}^2\cdot E}{2}\ . \qquad 2.7$$

The transition between LEFM and EPFM, denoted with a_{pl} in Fig. 5, is defined at $\varepsilon_f = \varepsilon_0$ and the maximum strain is assumed conservatively as the fracture strain from the tensile tests. Finally the fracture strain of the cracked specimens can be calculated with Eq. 2.8.

$$\varepsilon_f = \begin{cases} \dfrac{K_{Ic}}{\sqrt{\pi\cdot a}\cdot E\cdot Y\left(\frac{a}{W}\right)} & \text{for} \quad 0 \le \varepsilon_f, \varepsilon_0 \\ \left\{\left[\dfrac{J_c}{2\cdot\pi\cdot a\cdot Y\left(\frac{a}{W}\right)^2\cdot\left(1-\nu^2\right)} - \dfrac{{\varepsilon_0}^2\cdot E}{2}\right]\cdot f(n)\cdot\left[\dfrac{\alpha\cdot\varepsilon_0}{{\sigma_0}^n}\right]^{1/n}\cdot\dfrac{(1+n)}{n}\right\}^{\frac{n}{1+n}} + \varepsilon_0 & \text{for} \quad \varepsilon_0 \le \varepsilon_f \le \varepsilon_{f,exp} \\ \varepsilon_{f,exp} & \text{for} \quad \varepsilon_f \ge \varepsilon_{f,exp} \end{cases} \qquad 2.8$$

In Fig. 24, the failure curves determined analytically from Eq. 2.8 are compared with the experimental results. A good correlation is observed in the LEFM regime, where, due to the geometry function (Eqns. 2.2 and 2.3), the slope of the failure line steepens for longer cracks.

In the EPFM regime the failure curve is too conservative for all materials. Considering short cracks, fracture is significantly affected by the stress in the process zone and not by the local strain and therefore the *Q*-stress has to be considered like in the constraint based diagrams [41], [42] or similar work [27].

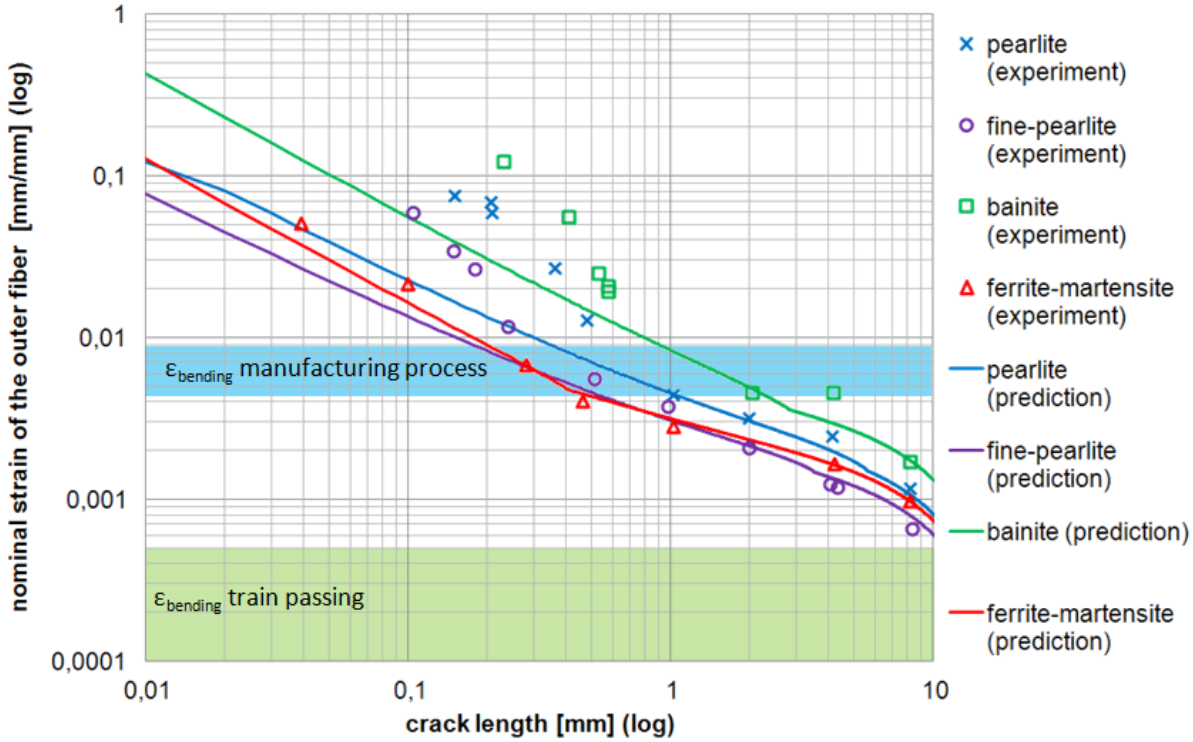

Fig. 24.: Prediction of failure curves with constant K_{Ic} and J_c and comparison with the experimental results. Additionally typical strains are displayed for the bending process and when a train is passing the switch.

In order to address the behavior of the increasing nominal strain at failure for very short cracks, the constraint effect due to plasticity has to be considered.

To this end, the HRR field from Eq. 1.13 can be calculated using the Ramberg-Osgood Eq. 1.14 and the parameters from Table 1 and the material constants I_n and $\tilde{\sigma}_{ij}(\theta,n)$ from the tables of Shih [24] for plane strain condition.

For numerical calculations, the FE-solver ABAQUS was used, including large deformations under plane strain condition. On this basis, FE simulations have been performed for each individual experiment (i.e. for each crack length a and maximum load F_{max}) to determine the J-integral and the stress in the crack opening direction at the point of failure. An exemplary numerical model is shown in Fig. 25. The loading and support cylinder was modelled by a 2D rigid part. The focus is set on the refinement of the crack tip with a maximum element size depending on the crack length of $a^{(e)} = a/100$ and a linear shape function following the recommendations in [63] and [64].

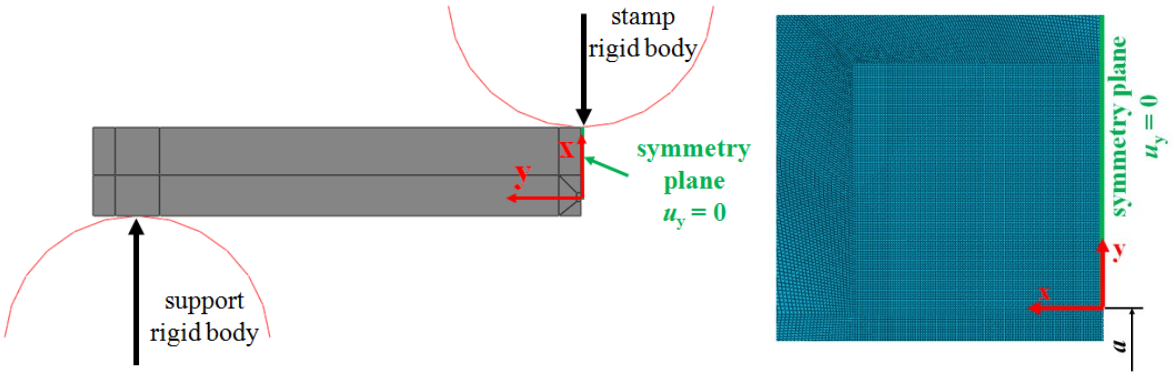

Fig. 25.: Exemplary model of the meshed crack in plane strain condition for the calculation of the J-integral and the stress in crack opening direction to determine the Q-stress.

The Q-stress [27], [28], [29] is defined by Eq. 1.15 as the difference between the actual stress field (computed by numerical simulation) and the approximate HRR field at the dimensionless distance $r/(J\cdot\sigma_0)$ and is calculated at $r/(J\cdot\sigma_0) = 2$, as recommended in the literatures.

The analytical (HRR) approach provides higher stresses due to lower constraint effects in the numerical simulation. The negative Q-stress determined with Eq. 1.15 is plotted in Fig. 26 with inverted signs so that the Q-stress is positive, as used in Eq.1.32.

The trend of the Q-stress, as plotted in Fig. 26, can be described by a functional dependence on the crack length; the respective parameters are listed in Table 2.

$$-Q(a) = D \cdot a^{k} \qquad 2.9$$

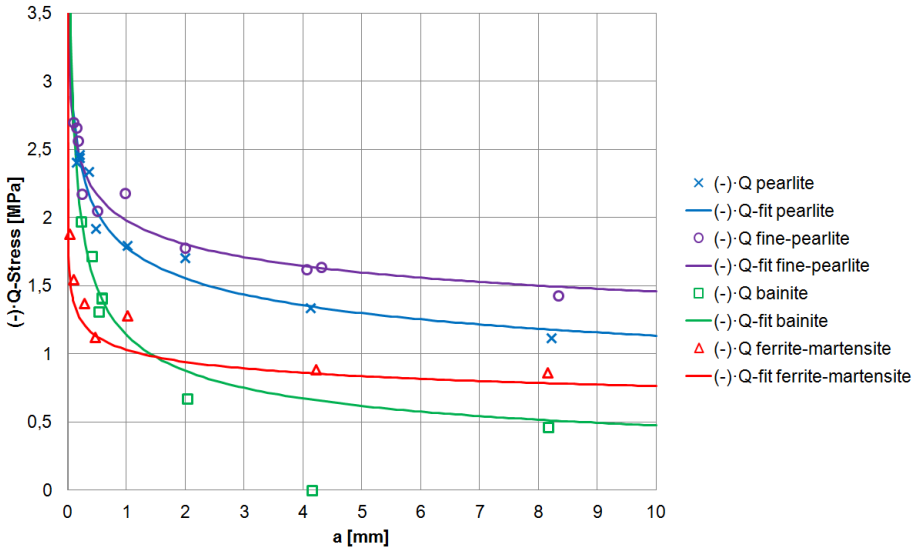

Fig. 26.: *Q*-stress vs. crack length; experimental results and approximation by Eq. 2.9.

Table 2: Parameters of Eq. 2.9 for the prediction of the *Q*-stress depending on the crack length.

material	***D***	***k***
pearlite	1.78	-0.20
fine-pearlite	1.98	-0.13
bainite	1.14	-0.38
ferrite-martensite	1.03	-0.13

The *J*-integral at failure, extracted from the performed numerical simulations, can be plotted against the *Q*-stress [28]. An approximate prediction of the dependence of the critical *J*-integral on the *Q*-stress is given by a function similar to Eq. 1.32, whose parameters are listed in Table 3.

$$J_c = J_{mat} \cdot \left[1 + \eta \cdot \left(Q(a)\right)^h\right] \qquad 2.10$$

where J_{mat} can be estimated from the fracture toughness K_{Ic} (Eq. 1.18).

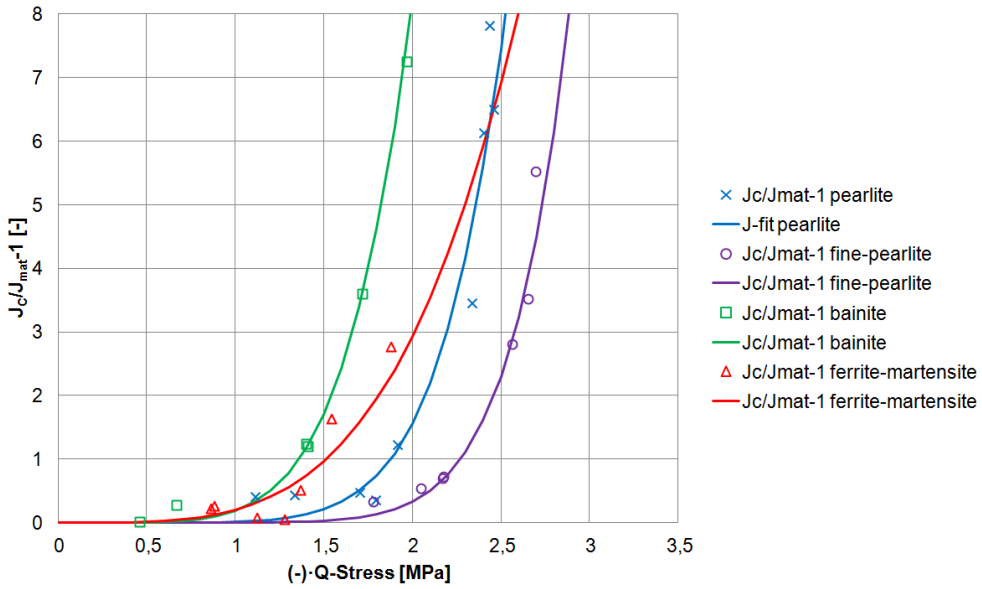

Fig. 27.: Critical *J*-integral against *Q*-stress extracted from the numerical simulations by using the maximum load from the experiments and its approximate prediction by Eq. 2.10 for the different materials.

Table 3: Parameters of Eq. 2.10 for the approximate prediction of the critical *J*-integral depending on the Q-stress.

material	η	h
pearlite	0.0121	7.01
fine-pearlite	0.0008	8.69
bainite	0.1856	5.47
ferrite-martensite	0.2032	3.85

The higher the positive *Q*-stress is, the higher is the critical *J*-integral. Inserting Eq. 2.9 in Eq. 2.10, the critical *J*-integral at failure can be predicted as a function of the crack length *a*:

$$J_c = J_{mat} \cdot \left[1 + \eta \cdot \left(D \cdot a^k\right)^h\right] \qquad 2.11$$

In Fig. 28 the calculated critical *J*-integral from the experiments is plotted against the crack length together with the prediction from Eq. 2.11.

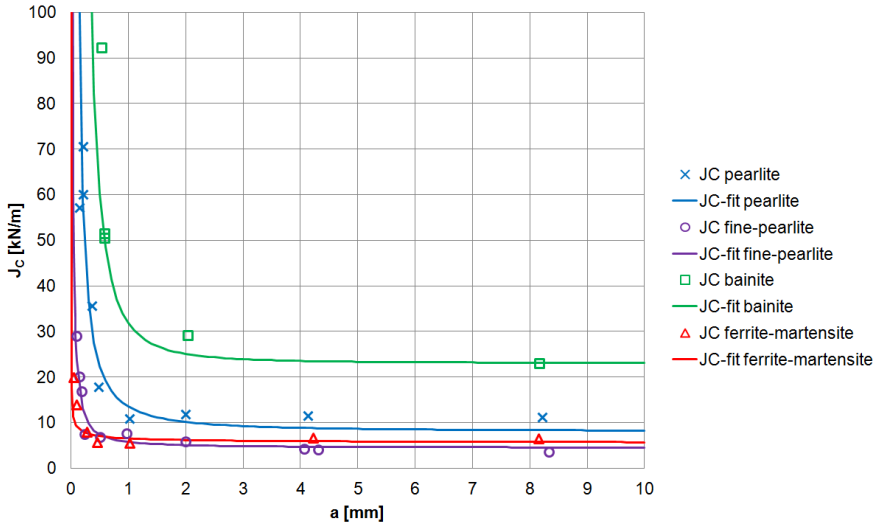

Fig. 28.: Critical *J*-integral depending on the crack length *a* from the numerical simulations using the maximum load from the experiments and its approximate prediction by Eq. 2.11 for the different materials.

Using Eq. 2.11 describing J_c and Eq. 2.8, the predicted failure curves can be calculated for the regimes of LEFM, EPFM and virtually flawless specimens. For validation, the result of this calculation is plotted together with the experimental results in Fig. 29.

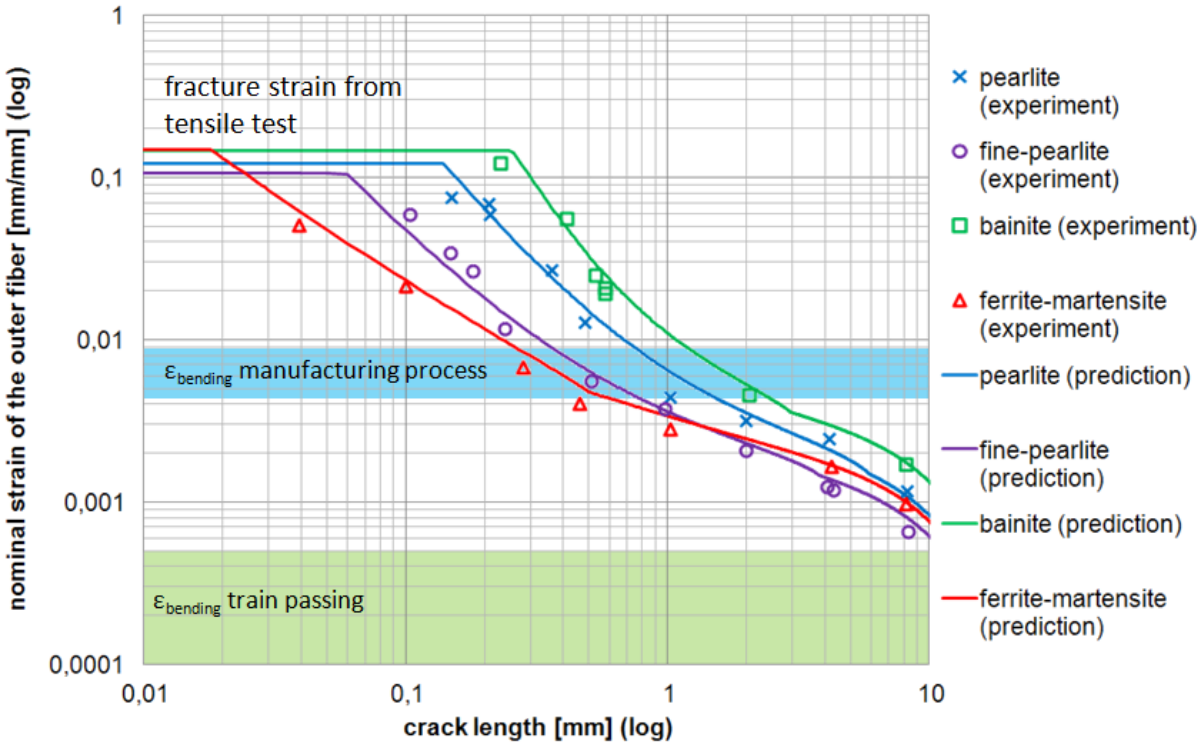

Fig. 29.: Failure strain in the static Kitagawa-Takahashi diagram using the *J*-*Q* concept. Additionally typical strains are displayed for the bending process and when a train is passing the switch.

It can be seen that the failure curves show a good correlation with the experimental data. Therefore, this method provides a good prediction of the failure strain depending on the flaw size with only a few experiments needed. This means that by combination of a tensile experiment to estimate the Ramberg-Osgood parameters as well as the fracture toughness and bending experiments with very short cracks to obtain the *Q*-stress dependency, the failure line can be determined completely.

In addition, Fig. 29 represents the strain range of the three-point bending process (blue area) during manufacturing and the resulting strains (green area) when a train is passing through the switch.

2.4. Proof of *J*-integral determination based on strain energy density

A proof of the validity of the used strain energy based determination of *J* by Shih and Hutchinson [34] and the extension of Dowling [35] (Eqns. 1.19 - 1.26) is done for single edge notch tension (SENT) specimens for various hardening materials in [4].

Special attention on this study is devoted to the effect of hardening and when the estimation breaks down. In this work, the geometry function is estimated by a polynomial function from [65] for a trough thickness crack in a tension specimen.

$$Y\left(\frac{a}{W}\right) = 1.12 - 0.231 \cdot \left(\frac{a}{W}\right) + 10.55 \cdot \left(\frac{a}{W}\right)^2 - 21.72 \cdot \left(\frac{a}{W}\right)^3 + 30.39 \cdot \left(\frac{a}{W}\right)^4 \qquad 2.12$$

Four different hardening exponents *n*, following the Ramberg Osgood material law, and also an ideal-plastic material is calculated by FE simulations.

All materials have been calculated with a Young's modulus of $E = 210$ GPa, a Poisson ratio of $\nu = 0.3$ and the material constants $\sigma_0 = 500$ MPa and Eq. 2.13 for α (cf. Eq. 1.14).

$$\alpha = \frac{\varepsilon_{0.2} \cdot E}{\sigma_0} \qquad 2.13$$

with $\varepsilon_{0.2} = 0.002$.

The ideal-plastic material behavior is defined by the following true stress- strain data points, listed in Table 4, where a slight gradient beyond the yield point is used in order to provide numerical stability.

Table 4: Stress strain data points defining the ideal-plastic and small strain softening material behavior.

material	σ_{pl} **[MPa]**	ε_{pl} **[-]**
ideal-plastic	500	0
	520	2

The ideal-plastic material is then compared with four different strain hardening materials. All materials are shown in Fig. 30, where the colours denote the different material hardening behaviors for $n = 5$, $n = 6$, $n = 12$, $n = 15$ and ideal-plastic behavior.

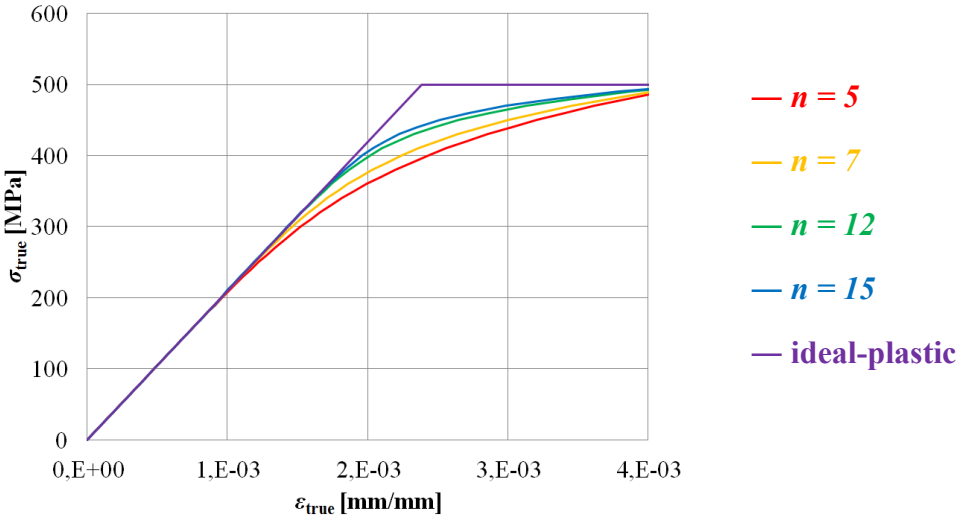

Fig. 30.: Comparison of the different material behaviors, n = 5, n = 7, n = 12, n = 15 and ideal-plastic material behavior in the true stress-strain diagram.

2.4.1. Finite element (FE) simulations

The underlying geometry of the following calculations by the FE solver ABAQUS is a displacement controlled tension sample in plane strain conditions. In Fig. 31 a) the geometry of the upper half of the specimen and its partitions are shown. The half-height of the specimen is $H/2 = 50$ mm, the specimen width $W = 50$ mm. The crack length is varying for $a/W = 2/100$, $a/W = 1/10$ and $a/W = 1/5$. The upper red line represents the boundary condition for the displacement in y direction $u_y/2$ and the lower red line represents the symmetry, representing the ligament, defined by $u_y = 0$. The applied displacement of the half-specimen is $u_y/2 = 0.2$ mm and implies a total strain of about 0.4 %.

In Fig. 31 b) the global and refined mesh in the vicinity of the crack tip is shown. The focus is set on the refinement of the mesh on crack tip with a maximum element size depending on the crack length of $a^{(e)} = a/100$ and the refinement of the shear band by an element sizes $a^{(e)} = 100\mu m$. All elements denote a linear shape function following the recommendations [63] and [64].

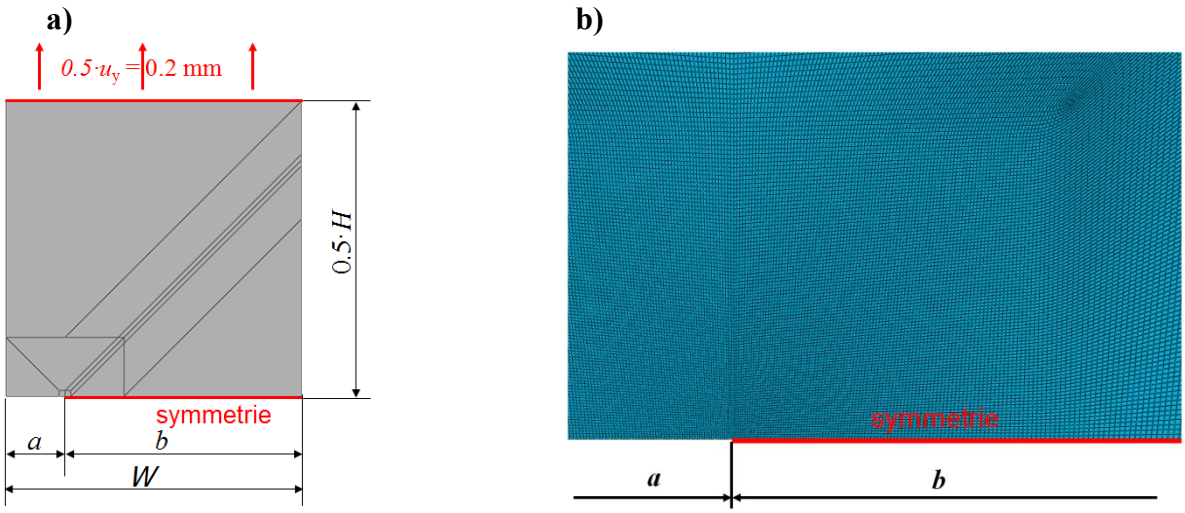

Fig. 31. Numerical model of the half-specimen with boundary conditions and in a) the geometry and the partitions and in b) detail of the refinement on the crack tip.

To set the different material hardening behaviors, the command *deformation plasticity* in ABAQUS is used, which represents the Ramberg-Osgood material law.

Furthermore, the *J*-integral is calculated by the path independent line integral J_Γ with Eq. 1.12, implemented in *ABAQUS*.

2.4.2. Results of FE simulations and analytical determination of *J*

In the following diagrams, the results from the numerical simulations and strain based method for *J* are plotted and compared for each crack length in a) a = 1mm, b) a = 5 mm and c) a = 10mm. Again, different colours denote different material hardening resp. softening behaviors (n = 5, n= 7, n = 12, n = 15 and ideal-plastic).

In Fig. 32 the ratio of the total reaction force F in the symmetry line (Fig. 31) to the specimen thickness B is plotted over the displacement u_y.

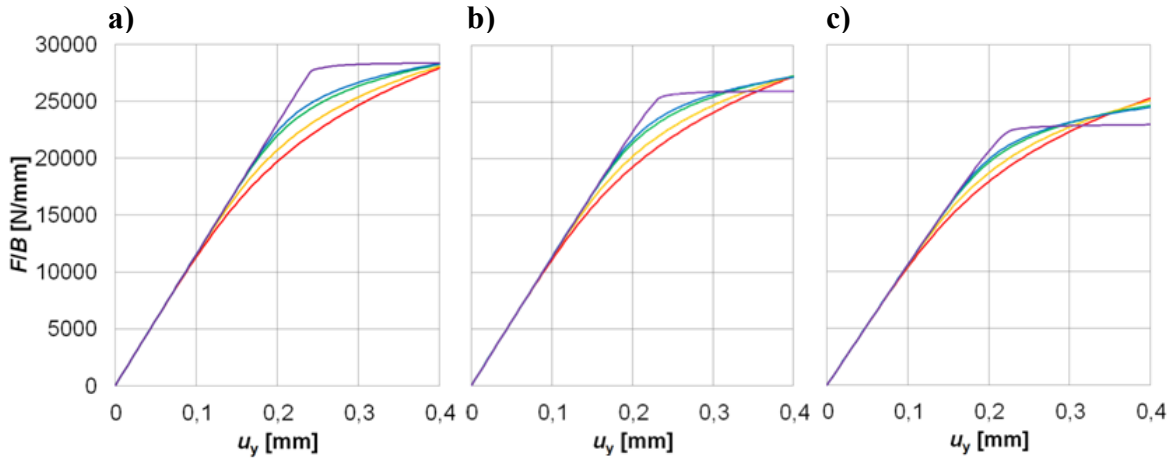

Fig. 32.: Force to specimen thickness ratio F/B over the displacement u_y for the different hardening exponents $n = 5$, $n = 7$, $n = 12$, $n = 15$ and ideal-plastic behavior for the different crack lengths a) a = 1mm, b) a = 5 mm and c) a = 10mm.

The curves correlate for each crack length with the material law from Fig. 30. The ideal-plastic material clearly shows the different global forces at the yield point, depending on the crack length a due to varying ligament lengths ($b = W - a$).

The J-integral J_Γ, using the results from the line integral of the FE simulations, is plotted as a function of the displacement u_y in Fig. 33.

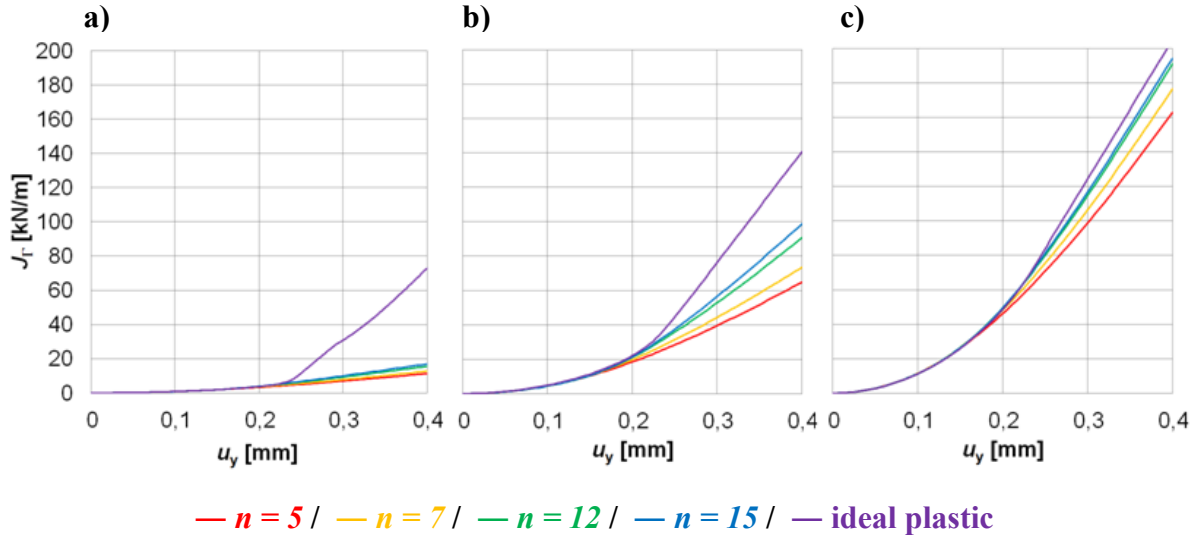

Fig. 33.: J-integral J_Γ determined from the finite element simulation as a function of the displacement u_y for the different hardening exponents $n = 5$, $n = 7$, $n = 12$, $n = 15$ and ideal-plastic behavior for the different crack lengths a) a = 1mm, b) a = 5 mm and c) a = 10mm.

The *J*-integral for all material types is equal until the onset of large scale yielding, which defines the regime of small scale yielding. In the following large scale yielding region, a nearly linear increase of J_Γ as a function of the displacement is observed as expected and is proportional to *n*. Moreover, considering an ideal-plastic behavior, J_Γ is increasing significantly for small crack lengths as a result of higher deformations at the crack tip in the regime of large and full scale yielding for these material behaviors.

In the plot of Fig. 34 the *J*-integral $J(w)$, calculated from strain energy density w using Eqns. 1.19 - 1.26 and 2.12, is plotted as a function of the line integral J_Γ derived from FE simulations. For the calculation of the strain energy density, ε_{pl} and σ_{pl} are derived from the FE results.

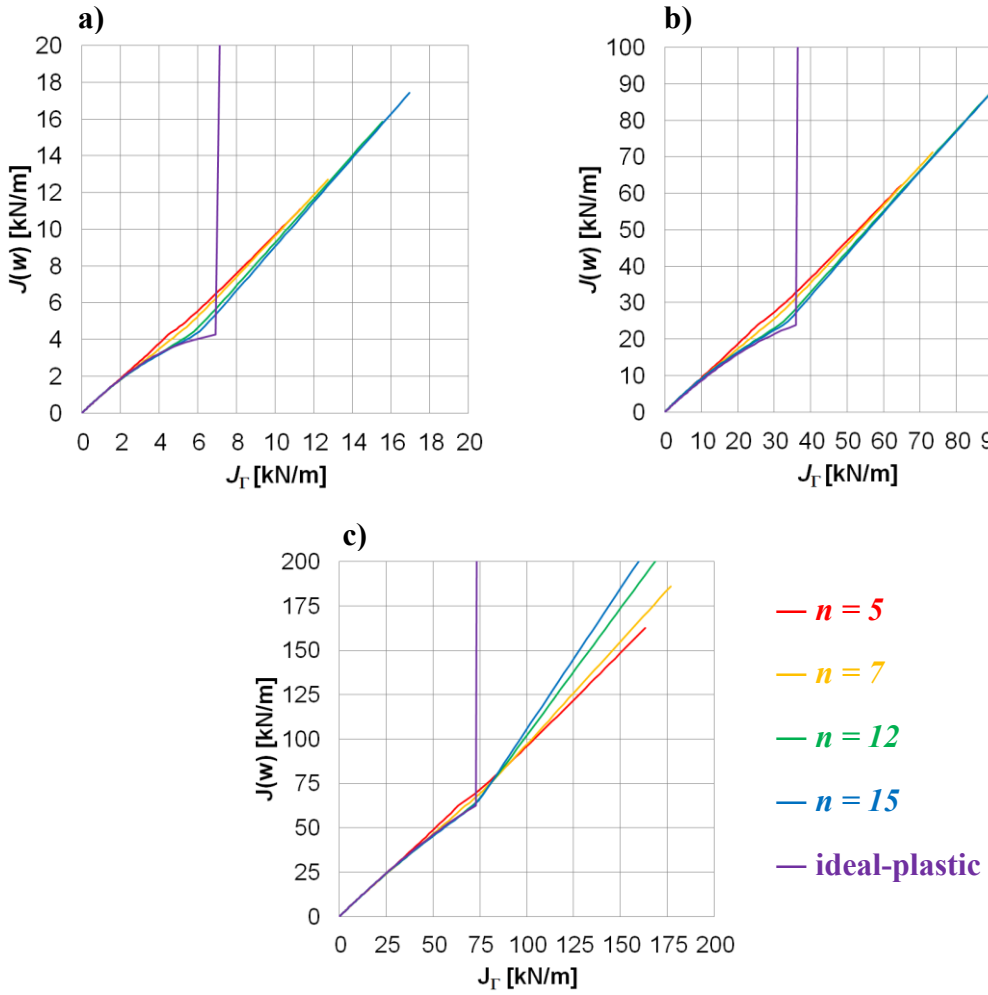

Fig. 34.: *J*-integral determined from w and the stress-strain curves and a variable function $f(n)$, over the *J*-integral J_Γ determined from the finite element simulation for the different hardening exponents $n = 5$, $n = 7$, $n = 12$, $n = 15$ and ideal-plastic behavior for the different crack lengths a = 1mm, b) a = 5 mm and c) a = 10mm.

Estimating the strain based $J(w)$ reproduces the line integral J_Γ for short cracks up to a/W = 1/10 and a hardening exponent n. Nevertheless, for long cracks, shown in Fig. 34 c), $J(w)$ is over-estimating J_Γ with increasing hardening exponent n. Furthermore, for ideal-plastic material behavior $J(w)$ is infinity, due to Eq. 1.23, beyond the yield strength in the regime of full scale yielding, shown in [34].

Nevertheless, those simple calculations, prove the good correlation of the strain energy based J-integral which is used as crack driving force in the static strain based Kitagawa-Takahashi diagram resulting in Fig. 29. Further conclusion to the strain based J-integral, especially to non-hardening materials can be found in [4].

3. Endurance limit as a design criterion

For cyclically loaded components the endurance limit is commonly used as a design criterion. In this chapter two different approaches for calculation of the endurable stress are presented: a stress based design and a fracture mechanics approach, following the article [1]. The focus is on plain fatigue, excluding issues related to rolling contact fatigue (RCF) in the region of the running tread.

3.1. Stress based design concept

For the estimation of the endurance limit under tension/compression loading, the ultimate tensile stress σ_{UTS} is reduced by a fatigue strength factor f_e following FKM [14]. Furthermore the endurance limit depends on the stress ratio R. Hence, the endurance limit can be calculated by Eq.1.2 where $K_m(R)$ is the mean stress factor which can be calculated with Eq. 1.3.

As already mentioned, rails are exposed to bending loads. Therefore, the endurable stress amplitude is higher than for a tension/compression loading. This is considered by the elastic support factor n_σ for cyclic loading (Eq.1.5) and the plastic support factor n_{pl} factor for static loading (Eq. 1.6).

The endurance limit in the stress based analysis is reduced by several factors such a notches, surface roughness etc.. Hence, regarding rail production and the resulting surface roughness in the as-rolled condition, a reduction factor $K_{surface}$, following FKM [14] has to be taken into account by Eq. 1.8.

In the rail industry, for the stress based analysis, the Smith diagram is commonly used for prediction of the endurance limit. This diagram is exemplarily displayed for the pearlitic material in Fig. 35 for one material under tension/compression (cyan line), bending load (light blue line) and bending load including an assumed surface roughness of the rolling skin (blue line). In addition, the black dotted line represents the mean stress and the dashed lines the different stress ratios R.

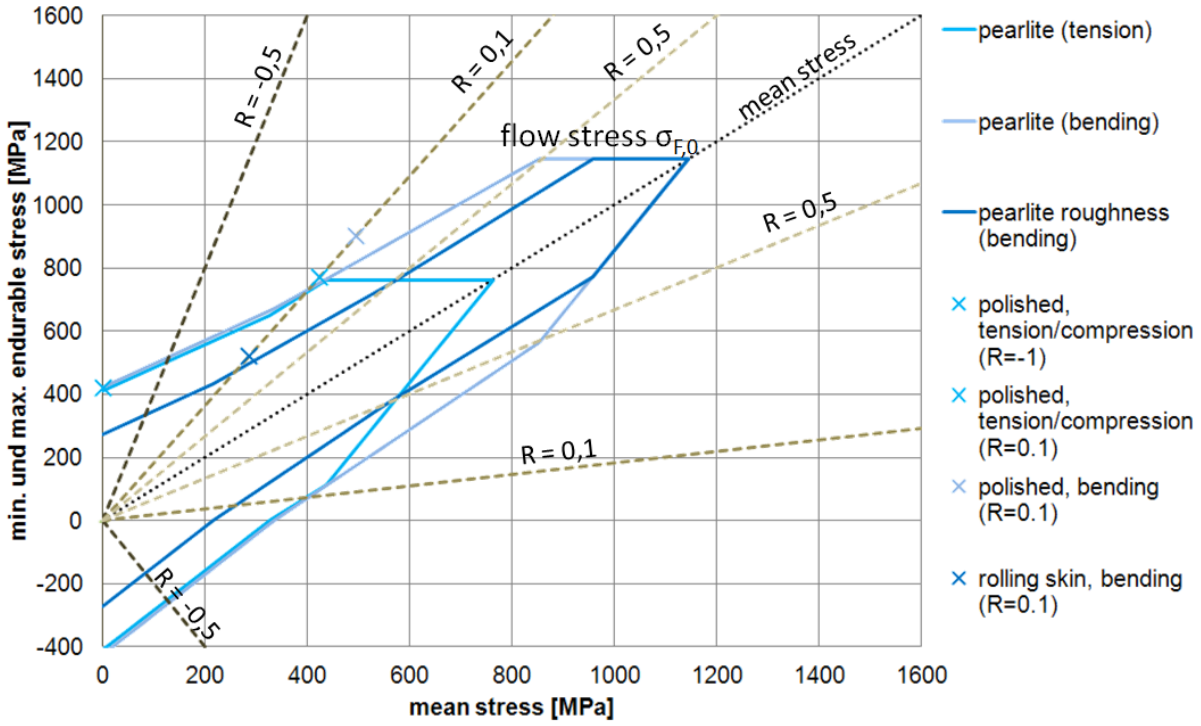

Fig. 35.: Smith diagram of the pearlitic material for tensile load (cyan line) and bending load (light blue line) assuming polished surface condition, for bending including an assumed surface roughness from the rolling skin (blue line) and fatigue strength experiments (crosses).

To validate the predicted endurable stress amplitudes, several fatigue experiments to determine the endurance limit have been done by voestalpine. Specimens are loaded in tension/compression and bending at different stress ratios. Additionally the influence of the surface roughness on the endurance limit has been tested. Therefore, the endurance limit of polished specimens and samples with the real rolling skin were analyzed. The experimental results are additionally displayed by crosses in the Smith diagram in Fig. 35.

For tension/compression loading at stress ratios of R = -1 and R = 0.1 the prediction correlates almost perfectly with the experiments. However, the predicted light blue line for the bending load is lower than the experimental result. Nevertheless, the difference is in an acceptable range and implies a conservative prediction. Also the prediction and the experiment for the endurance limit with the surface roughness correlate well.

Finally, Fig. 36 shows the predictions for all different materials investigated under bending including the influence of the surface roughness.

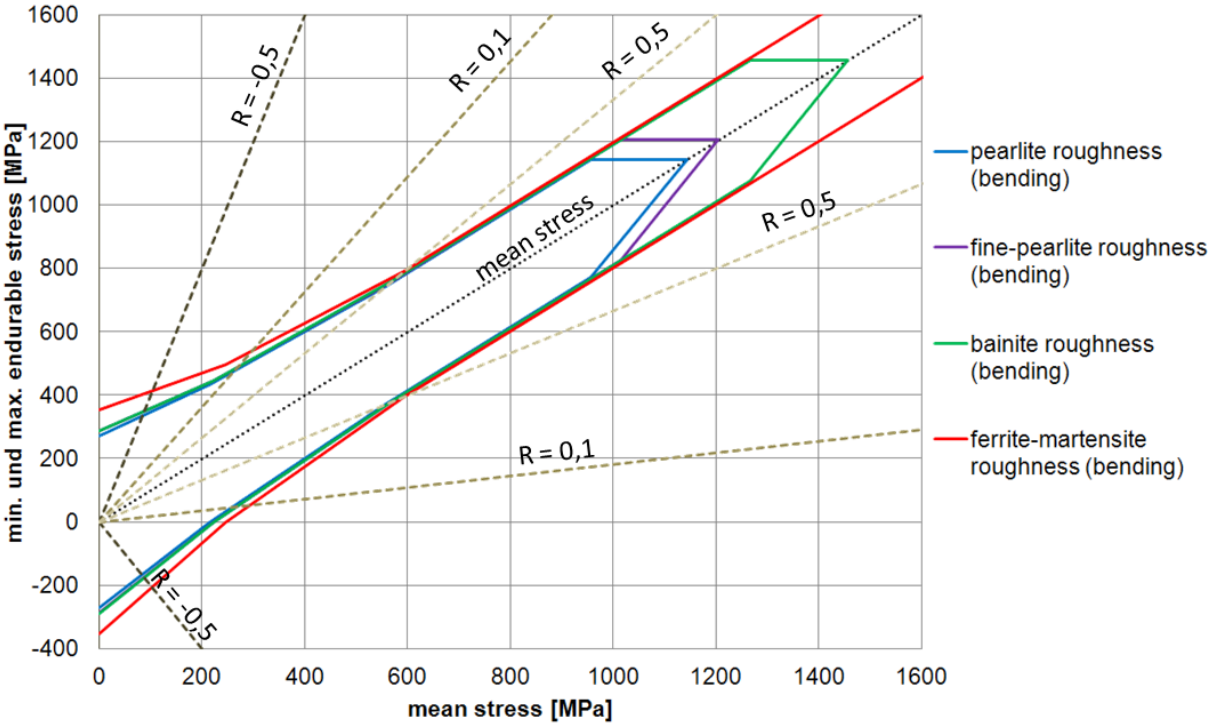

Fig. 36.: Comparison of all considered different materials for bending load and surface roughness in the as-rolled condition in the Smith diagram.

3.2. Experimental results of the crack resistance for the threshold and fatigue crack growth curves.

If notches are very sharp and hence can be considered as cracks, the stress based design is not valid anymore and a fracture mechanics approach has to be used as a design criterion. The stress intensity factor range ΔK of the crack can be calculated by Eq. 1.38.

Several parameters are necessary for application of design concepts based on the cyclic fracture mechanics approach, as already explained in section 1.3.3. Therefore, the cyclic crack growth behavior is determined by using single edge notch bending (SENB) specimens in a four point bending device (Fig. 15), starting from an initial crack length. Using the load increasing method at different stress ratios R, explained in chapter 1.3.3.3, the cyclic crack resistance curve (R-curve) and the long crack threshold $\Delta K_{th,lc}$ for each material have been measured. The results provide the necessary information for the admissible stress range $\Delta\sigma$, depending on the crack length Δa in the Kitagawa-Takahashi diagram.

In Fig. 37 the experimental results of the crack growth resistance curve are plotted for each material: a) pearlite, b) fine-pearlite, c) bainte and d) ferrite-martensite. Different colours denote different stress ratios: purple R = -1, blue R = 0.1 and green R = 0.7. Each symbol represents an applied load ΔK at a crack length Δa, where the crack arrests due to closure mechanisms (shown in Fig. 12).

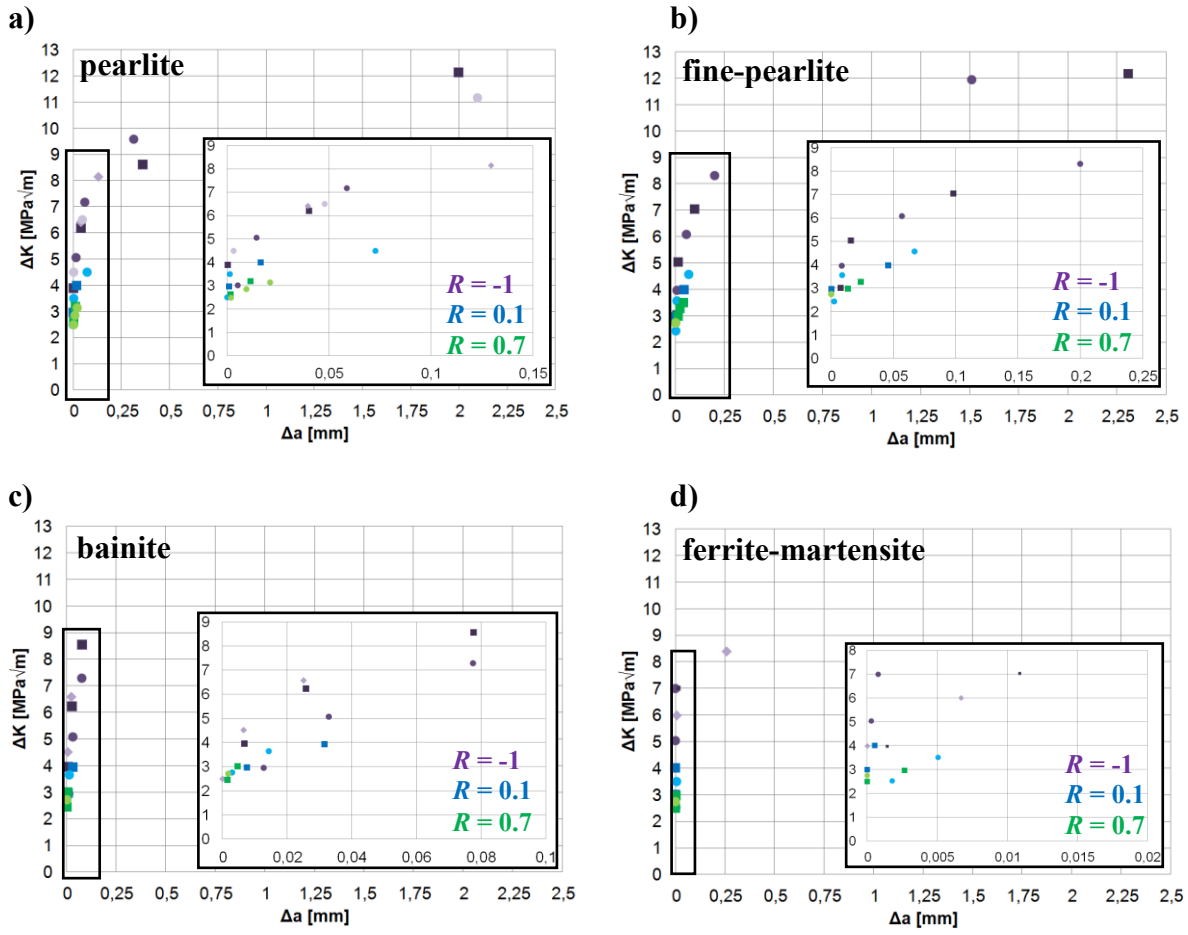

Fig. 37.: Comparison of the experimental results of the crack resistance curves for the different materials in a) pearlite, b) fine-pearlite, c) bainite and d) ferrite-martensite. The purple symbols denote the stress ratio R = -1, the blue symbol R = 0.1 and green symbol R = 0.7.

The experimental results of the R-curve for ΔK_{th} in Fig. 37 represent the increase of threshold as a function of crack extension depending on the material type. The pearlite in a) and fine-pearlite in b) represents a typical tendency of an R-curve (Fig. 12), from the effective threshold ΔK_{eff} (~2.5 MPa√m) to the long crack threshold $\Delta K_{th,lc}$, explicitly for R = -1, where $\Delta K_{th,lc}(R = -1) \approx$ 12-13 MPa√m. However, the initial gradient $\Delta K_{th,lc}/\Delta a$ of the bainitic and ferrite-martensitic material is steeper and $\Delta K_{th,lc}(R = -1) \approx$ 9-10 MPa√m.

The different $\Delta K_{th,lc}$, exhibit a linear dependency on R as already shown in Eq. 1.40. At the stress ratio R = 0.7 almost no closure effects occur which means $\Delta K_{th,lc} \approx \Delta K_{eff}$ and hence is nearly independent of the material type.

The differences of the short crack behavior, the gradient of the slope and $\Delta K_{th,lc}$, denoted by the cyclic crack resistance curve of each material type, can be explained by the different closure mechanisms as a result of the different hardening behavior and the differences in the microstructures.

Beyond the long crack threshold $\Delta K_{th,lc}$, the crack growth behavior is commonly calculated with the NASGRO equation (Eqns. 1.42 and 1.48). Therefore, several parameters have to be determined by fracture mechanics experiments, again with SENB specimens. In Fig. 38 the experimental results of the crack growth da/dN is plotted as a function of ΔK for the different materials; a) pearlite, b) fine-pearlite, c) bainte and d) ferrite-martensite. The different colours again denote different stress ratios: purple R = -1, blue R = 0.1 and green R = 0.7.

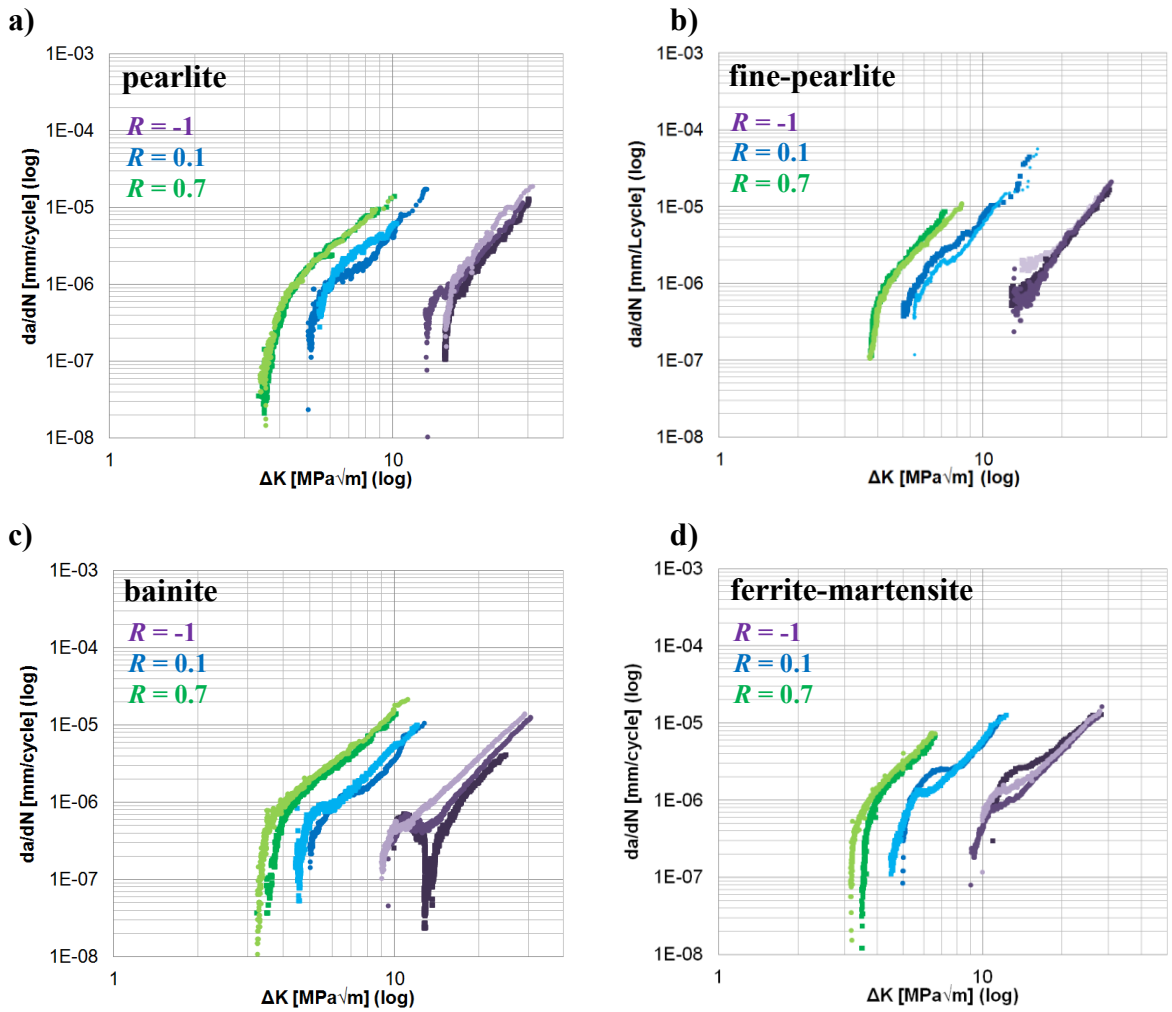

Fig. 38.: Comparison of the experimental results of the crack growth curves for the different materials in a) pearlite, b) fine-pearlite, c) bainite and d) ferrite-martensite. The purple dots correspond to the stress ratio R = -1, the blue dots to R = 0.1 and green dots to R = 0.7.

In the diagrams of Fig. 38 the almost vertical slopes at $da/dN < 10^{-7}$ represent approximately the long crack threshold $\Delta K_{th,lc}$. Nevertheless, the gradient in the Paris regime (shown in Fig. 14) is nearly the same for each material. However, the transition from the $\Delta K_{th,lc}$ to the Paris regime, characterized by the value p in the NASGRO equation (Eq. 1.42) is different, depending on the material type.

3.3. Fracture mechanics approach

If notches are very sharp and hence can be considered as cracks, the stress based design is not valid anymore and a fracture mechanics approach has to be used as a design criterion. The stress intensity factor range ΔK of the crack is calculated by Eq. 1.38.

Using the Smith diagram, an endurance limit can be calculated, yet in the fracture mechanics approach it is based on the crack length and represented in the Kitagawa-Takahashi diagram [48], cf. Fig. 11.

For a simplified illustration of the behavior described by Eq. 1.41, the endurable stress range is calculated for a surface crack with $a_0 \rightarrow 0$ and a geometry factor $Y = 0.8$. The resulting Kitagawa-Takahashi diagram is displayed for the different materials in Fig. 5 at stress ratios $R = 0.1$ and $R = 0.7$.

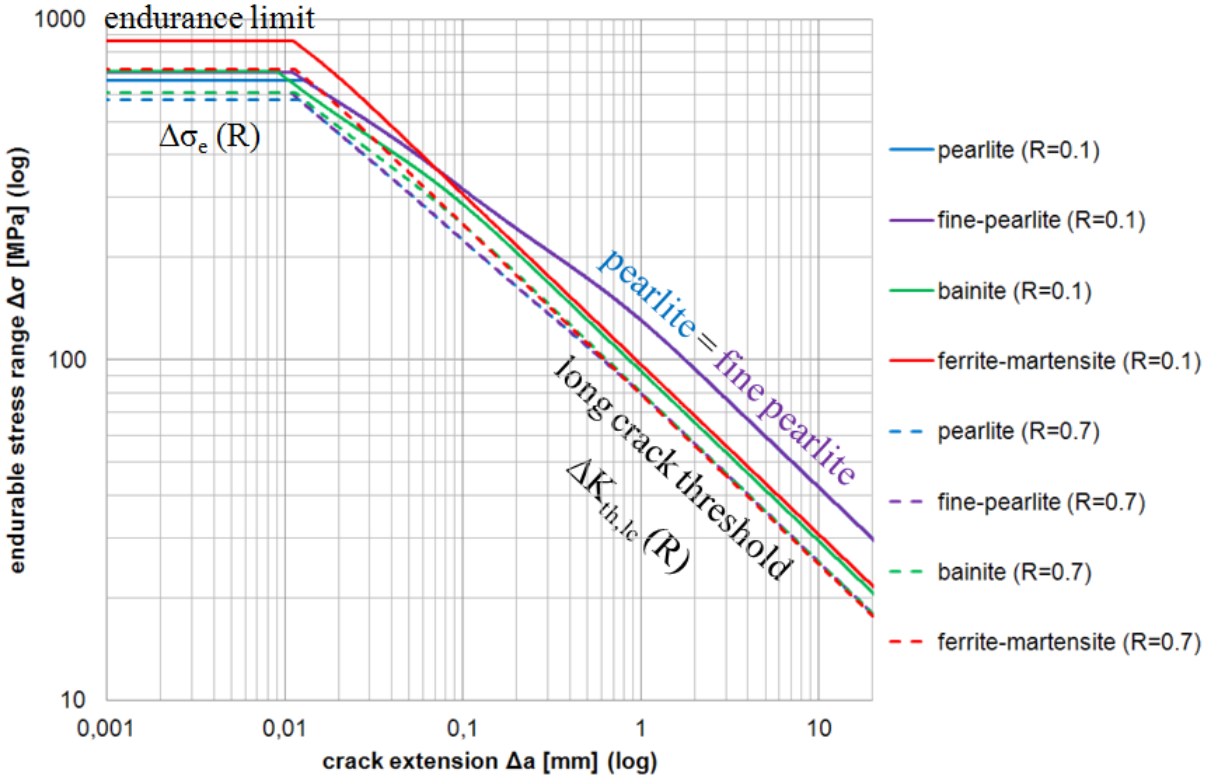

Fig. 39. Comparison of different materials in the Kitagawa-Takahashi diagram at stress ratios R of 0.1 and 0.7, for near surface cracks with $Y = 0.8$.

In consideration of a pre-cracked sample the pearlitic and fine-pearlitic materials denote the highest long crack threshold. The endurance limit for the ferrite-martensite material is the highest of all considered materials, whereas for crack lengths $a > 0.1$ mm the endurable stress range is smaller compared to the others.

For higher stress ratios, e.g. $R = 0.7$, shown by the dashed lines, the long crack threshold is roughly equal for all materials because closure is almost vanishing.

Furthermore, the experimental data of the endurance limit under bending with surface roughness (cf. green crosses in Fig. 35) can be displayed. For this the fracture surfaces, exemplarily shown in Fig 6 a) and b) were analyzed using an optical microscope. The initial notch, considered as a crack, is measured and approximated by a semi-elliptical shape (Fig. 40 c)).

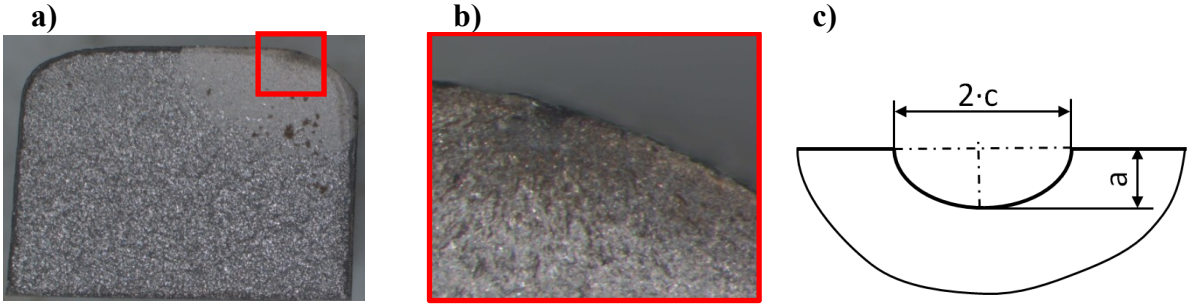

Fig. 40. Flaw size determination from the fatigue strength experiments: a) view of the total fracture surface, b) detailed view of the failure initiation point and c) schematic sketch of the measured, idealized flaw geometry.

In consideration of a semi-elliptical crack, ΔK can be calculated depending on the applied stress range from the experiment, the crack length and the geometry factor from Newman and Raju ([67], [68], [69]):

$$\Delta K = Y\left(\frac{a}{c}, \frac{a}{W}, \frac{a}{B}, \theta\right) \cdot \Delta\sigma \cdot \sqrt{\pi \cdot a} \,. \qquad 3.1$$

Using Eq. 3.1, the experimental data of the fatigue experiments at the load ratio $R = 0.1$ can then be displayed in the Kitagawa-Takahashi diagram (Fig. 41).

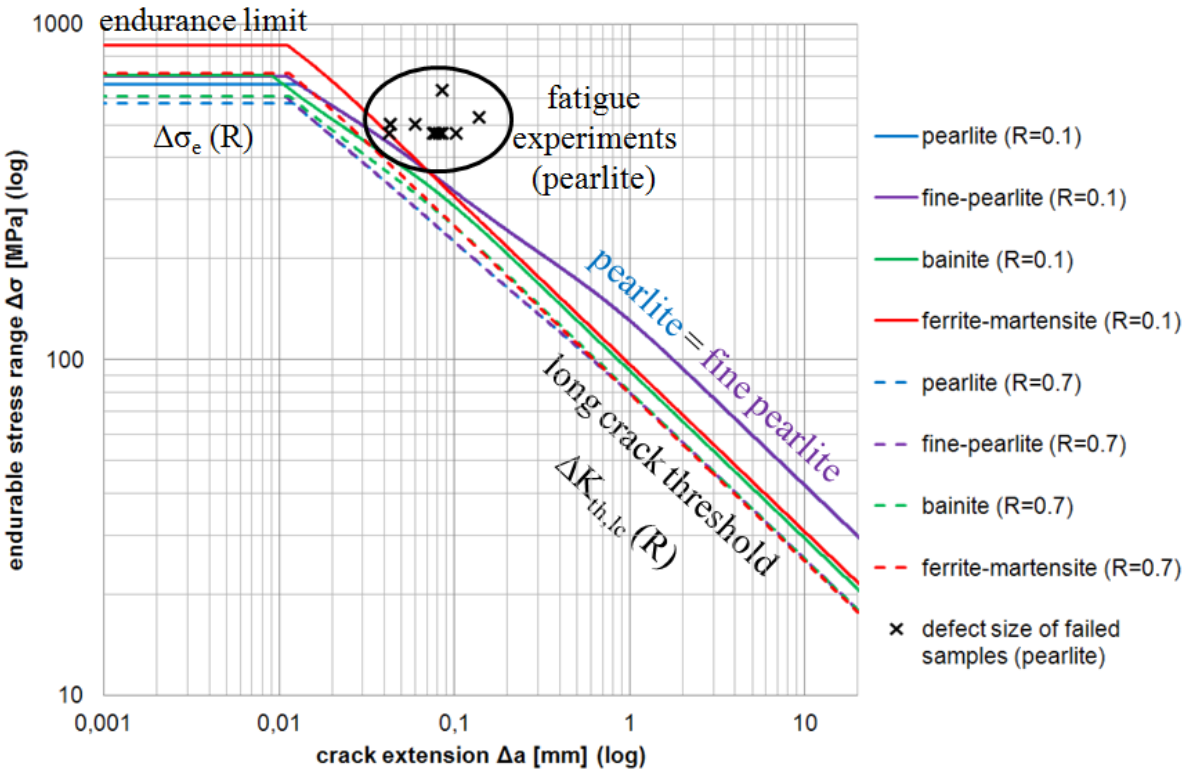

Fig. 41. Comparison of different materials in the Kitagawa-Takahashi diagram at stress ratios R of 0.1, for near surface cracks with $Y = 0.8$ and fatigue strength experiments.

It can be seen that the proposed approach gives a good, even though conservative estimation of the safe region.

Finally, instead of choosing the stress ratio R as a parameter for visualizing Eq. 1.41, one can also take the crack size. This leads to the crack size dependent Smith diagram displayed in Fig. 42, where the endurable stresses are plotted for crack lengths 0.1 mm $\leq a \leq$ 0.5 mm.

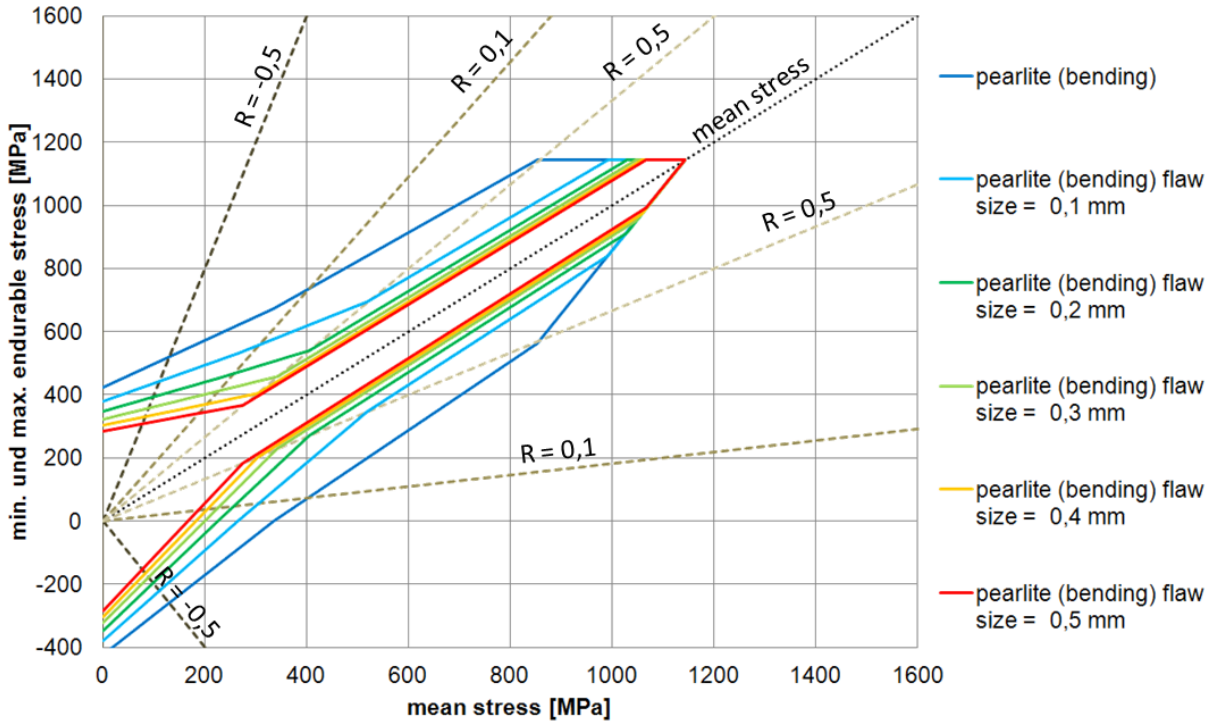

Fig. 42.: Endurable stress depending on the defect size from Eq. 16 plotted for the pearlitic material in the Smith diagram.

4. Fatigue strength vs. crack growth as a design criterion

For cyclically loaded components with applied stress ranges beyond the endurance limit, the fatigue strength has to be considered. Due to the information of the gradient k_f of the fatigue strength slope (cf. Fig. 6), the Miner rule is commonly used to calculate the end of life with Eq. 1.9 in a stress based design concept. Notches reduce the fatigue strength slope similar to the endurance limit by certain factors.

Considering cracks in the regime of LEFM with loads beyond the long crack threshold, the cracks will grow until failure and the propagation can be calculated by the NASGRO equation (Eq. 1.42).

4.1. Crack growth based on finite element simulations

Due to complex geometries and therefore accompanying challenges of calculating the stress intensity of cracks, numerical simulations are often used in combination with the NASGRO equation to calculate the crack growth.

Therefore, a load spectrum from measurements, classified in different load blocks is required (cf. Fig. 43 a)). Assuming a linear material behavior and an applied unit force, the stress intensity along the crack front can be extracted from FE simulations, shown in Fig. 43 b).

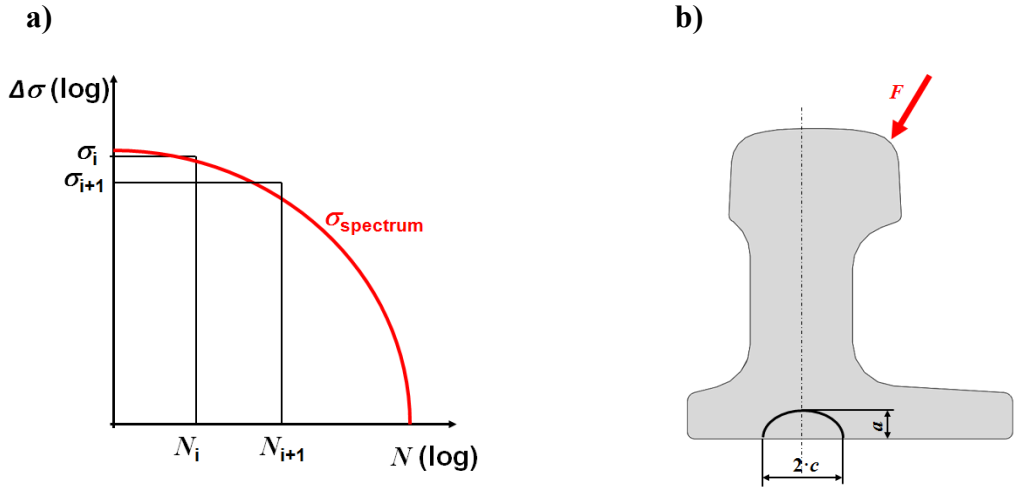

Fig. 43.: a) Schematically plotted load spectrum and b) a switch blade with a semi-elliptical crack front and applied unit load.

Nevertheless, the initial step has to be calculated using a starting crack length of $a = a_0$.

The threshold value $\Delta K_{th,i}$ along the crack front of each load block can then be calculated by the relationship of Eq. 4.1 assuming linear behavior.

$$\Delta K_{\mathrm{th,i}} = \Delta K_{\mathrm{FEM}} \cdot \frac{\Delta\sigma_i}{\sigma_{\mathrm{unit}}} \tag{4.1}$$

where σ_{unit} denotes the stress by an applied unit load, at the position of the measured load spectrum. The stress intensity ΔK_{FEM} along the crack front is extracted from FE simulations and $\Delta\sigma_i$ means the stress range from the load spectrum at the load block i. Using the information of the threshold and the number of cycles N_i of each block, the crack growth Δa_{i} can be calculated with Eqns. 1.42 - 1.45, which includes the modified NASGRO equation.

The main advantage of the crack growth calculation by using FE simulations, is the accuracy of K along the whole crack front. Nevertheless, FE simulation, especially for complex parts can be challenging due to numerical stability problems and hence may be time consuming.

4.2. Analytical estimation of the Crack growth

Analytical calculations of the stress intensity factor if available, considering different crack shapes and part dimensions circumvent the need of time consuming FE simulations.

The stress intensity factor in mode I, considering LEFM is calculated by

$$K_{\mathrm{I}} = \sigma_{\mathrm{appl}} \cdot Y\left(\frac{a}{c}, \frac{a}{W}, \frac{c}{B}\right) \cdot \sqrt{\pi \cdot a} \tag{4.2}$$

where σ_{appl} and the crack length a are known and K_{I} just depends on the geometry factor Y, which in turn depends on the crack depth a, the crack width $2 \cdot c$, the specimen thickness W and the specimen width $2 \cdot B$, see Fig. 44.

Early works [66] represent simple analytical equations of the geometry factor in 2D boundary problems and were extended in 3D geometries with a satisfying accuracy. Newman and Raju (NR) et al. [67], [68], [69] published approximate solutions for the geometry factor of semi-elliptical cracks under tension and bending (M_{x}), which are nowadays commonly used in the structural stress concept. For these calculations, a maximum difference to the FE results of $\pm 5\%$ is mentioned and is valid for ratios $0.2 \leqslant a/c \leqslant 1.0$, $c/B < 0.5$ and $a/W \leqslant 1.0$. Additionally, Newman [70] provided an enhanced formulation for higher c/B ratios ($c/B \leqslant 0.8$) under tensile loading with an accuracy of 5 %.

Based on the work by Newman and Raju a lot of investigations have been performed. Isida [71] uses the body force method to provide weight functions for a/W ratios $\leqslant 0.6$ and based on this work Fett et. al. [72] improves the angular dependency for the near surface points. Furthermore, Wang and Lambert [73] provide stress intensity functions depending on the stress distribution for ratios $a/W \leqslant 0.8$ and a comparison with the investigations from

Shiratori [74], which can be found in the stress intensity factor handbook by Murakami [20]. Vainshtock [75] pointed out the different validities and accuracies of commonly used geometry factor formulations for center, semi-elliptical and corner edge cracks by several FE simulations. While commonly available results assume a Poisson's ratio of $\nu = 0.3$ typical for metals, Strobl [76] provides an analytical function for different ν, valid for a/W and $c/B \leqslant 0.5$.

These works depend on different crack shapes and specimen dimensions with straight boundaries (prism). Additionally several articels provide stress intensity factors for cylindrical specimens like pipes or shafts ([77], [78]) and also for the consideration of the root stress concentration when a crack starts from a notch ([79], [80]). For welded joints different solutions depending on the crack shape and boundary dimensions are available ([81], [82]) including, e.g., the situation in a Francis turbine runner [83].

Nevertheless, all equations denote a limiting range of validity with respect to the relation of the crack to specimen boundary dimensions and therefore an enhanced approximate solutions for the stress intensity factor under tension and bending around two axes have been proposed in [5]. The proposed formulas extend the range of validity and comprise cases where the crack width $2 \cdot c$ and the crack depth a are close to the specimen width $2 \cdot B$ and the specimen thickness W, respectively.

In Fig. 44 the dimensions of a specimen with a semi-elliptical surface crack are illustrated. Additionally, the applied loads on the specimen are sketched, which are the tensile force F_z, bending around the horizontal x-axis with the moment M_x and additionally bending around the vertical y-axis with the moment M_y. With these load types all possible external loadings occurring in the structural stress concept can be covered using superposition, i.e., unsymmetrical bending (M_x and M_y) and membrane (tensile) loading (F_z).

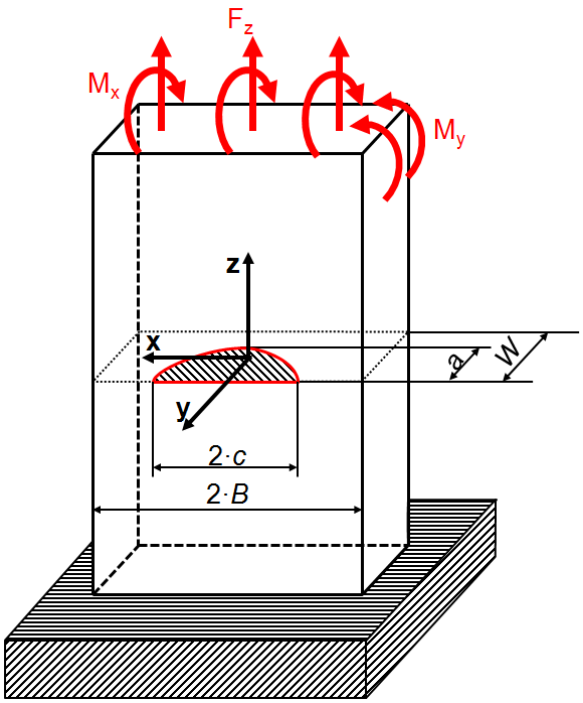

Fig. 44.: Dimensions of the specimen and the semi-elliptical surface crack.

As mentioned, the geometry factor Y depends on the geometry of the specimen and the geometry of the crack front. For given crack and specimen dimensions a, c, W, B and the applied stress σ, the stress intensity factor K_I has been computed by a finite element (FE) simulation, the geometry factor Y can subsequently be calculated by transforming Eq. 4.2 into

$$Y\left(\frac{a}{c},\frac{a}{W},\frac{c}{B}\right)=\frac{K_I}{\sigma\cdot\sqrt{\pi\cdot a}} \qquad 4.3$$

Newman and Raju (NR) published approximate solutions for the geometry factor of semi-elliptical cracks under tension and bending (M_x), which are nowadays commonly used in the structural stress concept. For these calculations, an accuracy of the FE results of ±3% is mentioned. Furthermore, to keep the approximate solutions sufficiently simple, a difference to the FE results of ±5% was accepted. Overall, this gives a total precision of about ±8%. The NR formulation is valid for ratios $c/B \leq 0.8$ and $a/W \leq 0.8$ and can be used from Appendix A.

The goal is to enhance the NR formulation for larger ratios of crack to specimen width (c/B) and crack length to specimen thickness (a/W). Moreover a geometry factor solution for bending around the vertical axis (M_y) will be developed.

Referring to Fig. 44 a new empirical solution for the geometry factor has been developed for the following ranges of validity:

- ratio of crack semi-axes a vs. c: $0.2 \leq a/c \leq 1.0$
- ratio of crack length a vs. specimen thickness W: $0.01 \leq a/W \leq 0.9$
- ratio of crack width $2 \cdot c$ vs. specimen width $2 \cdot B$: $0.01 \leq c/B \leq 0.9$.

4.2.1. Determination of the geometry factor by finite element simulations

The nominal stress for an un-cracked specimen can be calculated using the conventional equations for a beam with rectangular cross section $(2 \cdot B) \times W$ (see Fig. 45) under tension and bending:

$$\sigma_{\text{tension}} = \frac{F_z}{2 \cdot B \cdot W} \tag{4.4}$$

$$\sigma_{\text{bending-x-x}} = \frac{M_x}{I_x} \cdot e_y = \frac{M_x}{\frac{2 \cdot B \cdot W^3}{12}} \cdot \frac{W}{2} = \frac{3 \cdot M_x}{B \cdot W^2} \tag{4.5}$$

$$\sigma_{\text{bending-y-y}} = \frac{M_y}{I_y} \cdot e_x = \frac{M_y}{\frac{W \cdot (2 \cdot B)^3}{12}} \cdot \frac{2 \cdot B}{2} = \frac{3 \cdot M_y}{2 \cdot W \cdot B^2} . \tag{4.6}$$

The mode I stress intensity factor K_I is calculated by using the FE package *ABAQUS* assuming linear-elastic material behavior for steel (E = 210000 MPa, ν = 0.3). For the crack front, the J-integral is computed via the virtual crack extension method [84]. From this information the stress intensity K_I can be calculated, assuming plane strain conditions with Eq. 1.18.

K_I is calculated at the deepest point and at the surface points of the crack front as shown in Fig. 45, i.e., A ($\phi = 90°$), C_1 ($\phi \approx 0°$) and C_2 ($\phi \approx 180°$). For accuracy reasons discussed in detail in [77], points C_1 and C_2 are positioned not directly at the free surface of the specimen but as close as possible, which means $\phi \leq 1.40°$ for point C_1 and $\phi \geq 178.60°$ for point C_2.

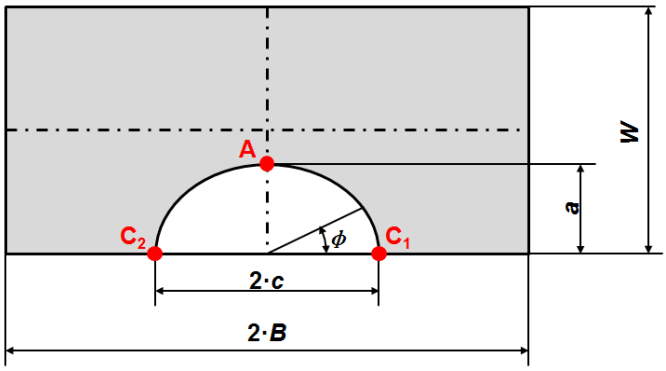

Fig. 45.: Section view for the dimensions of specimen, crack front and related positions of the deepest and surface points of the crack.

The geometry factor Y depending on the crack shape can then be calculated by using Eqns. 4.3 - 4.6 and the results of the FE simulations.

The accuracy of the geometry factor depends crucially on the mesh quality. Therefore obtaining a high quality mesh has to be the main focus of FE model preparation. To calculate the line integral (Eq. 1.12), the semi-elliptical crack is modelled with a fan-shaped structured mesh swept along the crack front and discretized with 35 elements in radial direction. The semi-ellipse is subdivided into 150 elements along the crack front. The crack tip is modelled with 8-node hexahedral elements and in the center with 6-node wedge elements.

In Fig. 46 an exemplary mesh for a/c = 0.8, a/W = 0.9 and c/B = 0.9 is shown. Generating an accurate mesh for such high ratios a/W and c/B is very challenging as can be guessed from this figure.

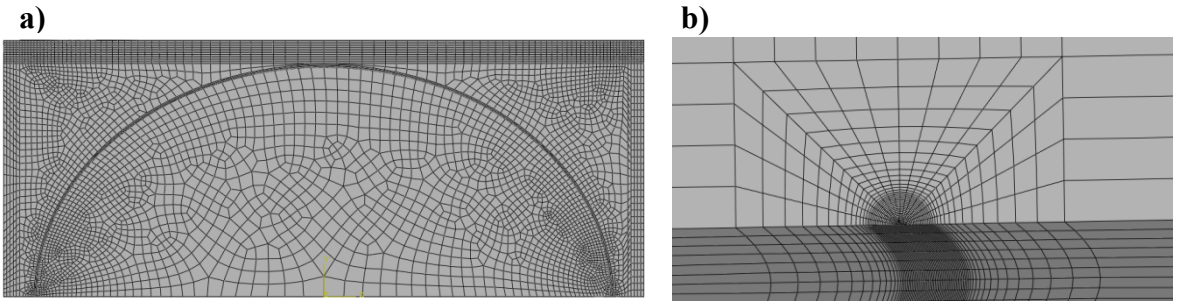

Fig. 46.: Example of the FE-mesh for a/c = 0.8, a/W = 0.9 and c/B = 0.9. a) front view of the specimen and crack front; b) detailed view of the meshed crack front.

At points A, C_1 and C_2, 20 contour integrals were calculated for each load. The J-integral was regarded as correct when the minimum error of 5 successive contours was within a difference of ±0.1 % related to the maximum value.

In Table 5 all considered geometry parameters are listed; FE simulations were performed for all 240 parameter combinations. The focus on high a/W and c/B ratios is evident.

Table 5: Considered geometry parameters

a/c	a/W	c/B
0.2	0.01	0.01
0.3	0.3	0.5
0.5	0.5	0.6
0.6	0.7	0.7
0.7	0.9	0.8
0.8		0.9
0.9		
1.0		

4.2.2. Results and comparison with the Newman-Raju approximation

In Fig. 47 and Fig. 48 the results of the FE simulations (horizontal axis) are compared with the Newman-Raju approximate solution [67], [68], [69], [70] (vertical axis) of each combination from Table 5, for loading in pure tension and by a bending moment M_x at points A ($\phi = 90°$) and C (in these cases, C_1 at $\phi \approx 0°$ and C_2 at $\phi \approx 180°$ give identical results). The full line represents the exact solution, which means that the analytical approximation is equal to the FE result. The dashed and dotted lines represent 10% and 20% over- and under-prediction with respect to the FE solution, respectively.

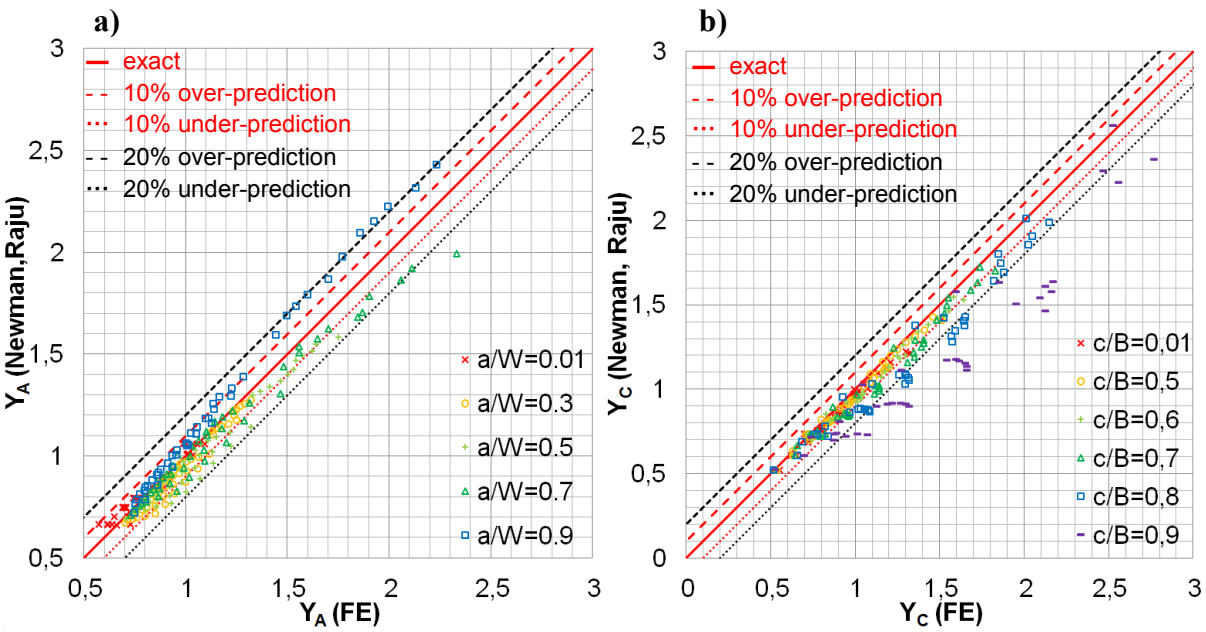

Fig. 47.: Comparison of the FE results with the approximate solution by Newman and Raju for pure tension F_z a) all results for point A, color/symbol distinction of a/W; b) all results for point C ($C = C_1 = C_2$), color/symbol distinction of c/B.

In Fig. 47 a) the comparison of the Y factors for point A is plotted for all parameter combinations. The different marks represent different a/W ratios, as the a/W ratio will have the highest influence on the geometry factor at point A. It can be seen that the NR solution fits almost perfectly to the FE results for $a/W \leq 0.5$; however, for $a/W \geq 0.7$ the FE results are under- and for $a/W \geq 0.9$ over-predicted.

Fig. 47 b) shows the comparison for point C. In this figure, the different marks represent different c/B ratios indicating how far point C approaches the specimen boundary. It can be observed that the NR approach again fits perfectly inside the original range of validity, but under-predicts the FE results for $c/B \geq 0.5$, outside the original range of validity.

The results in Fig. 48 for the specimen loaded by a bending moment M_x also exhibit good agreement with the NR formulation fitting acceptably well up to $a/W = 0.5$ for point A and $c/B = 0.5$ for point C.

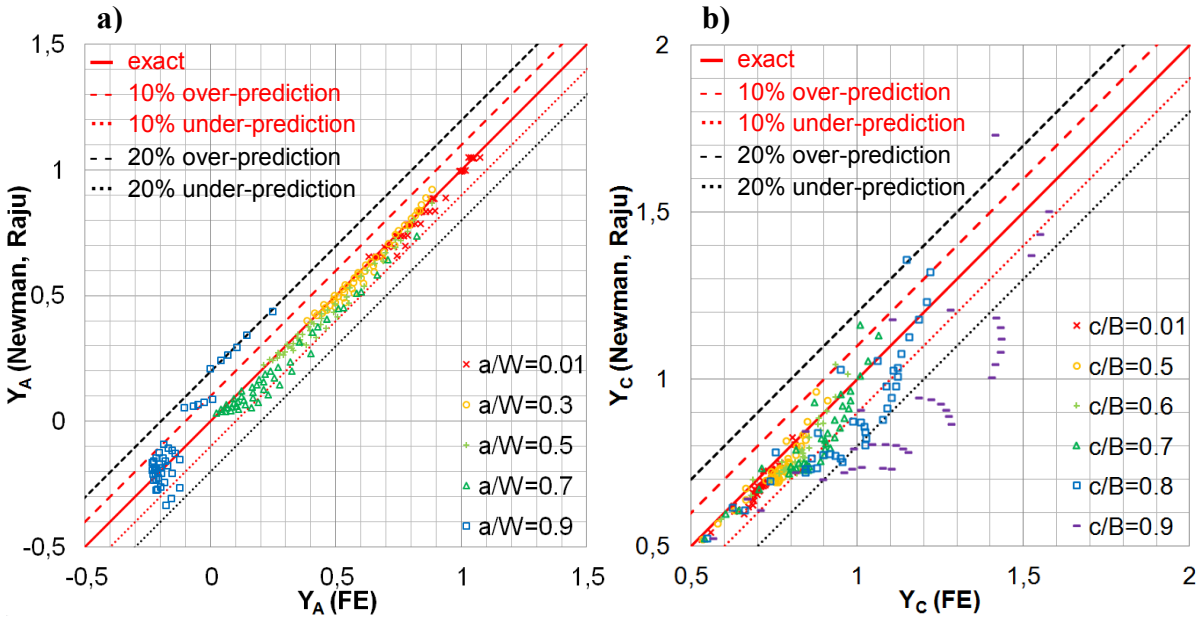

Fig. 48.: Comparison of the FE results with the approximate solution by Newman and Raju for bending M_X a) all results for point A, color/symbol distinction of a/W; b) all results for point C (C = C_1 = C_2), color/symbol distinction of c/B.

In general, the results of the FE simulations compared to the NR approach for tension and bending around the x-axis M_x show an acceptable prediction for all a/c ratios and small a/W and c/B ratios, respectively, up to 0.5. For higher values of a/W and c/B the NR approximation over-predicts Y_A and under-predicts Y_C. For this reason the development of an alternative approximate solution suitable for higher a/W and c/B ratios is required.

For a bending moment M_x, the stress intensity factor at point A becomes negative for $a/W \sim 0.8$ (which was excluded in the original Newman-Raju approximation), slightly depending on the a/c and c/B ratios, due to the bending stress distribution (Fig. 49 a).

For a bending moment M_y, the existing solution for a quarter-elliptical crack [20], [19] is not usable due to the anti-symmetric stress distribution. For this bending load, Y_A is zero due to symmetry as point A marks the neutral axis (shown in Fig. 49b). Another result due to symmetry is $Y_{C1} = -Y_{C2}$, where Y_{C1} is positive regarding the convention of a positive moment M_y around the y-axis (Fig. 49b).

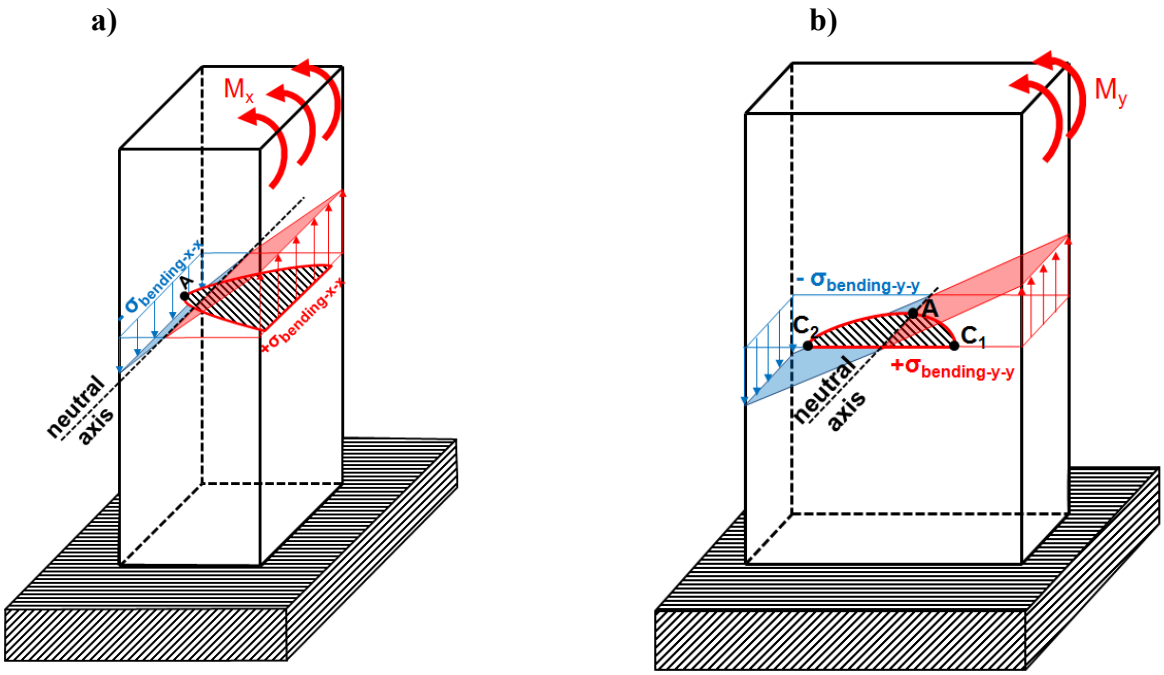

Fig. 49.: a) Compression at point A due to stress distribution for a bending moment M_x and high a/W ratio; b) tension resp. compression for Y_C at point C_1 resp. C_2 due to the stress distribution for a bending moment M_y.

4.2.3. Development of a new prediction for the geometry function *Y*

Based on the good agreement between the NR equations and the FE simulations for the ratios $a/W \leq 0.5$, $c/B \leq 0.5$ and $a/c \leq 1.0$, new equations only have to be developed for higher ratios. This is illustrated in Fig. 7a where the grey area represents the range of validity of the NR approach; the blue area and green areas display the regions for which enhanced formulations for the geometry function will be developed in the following sections.

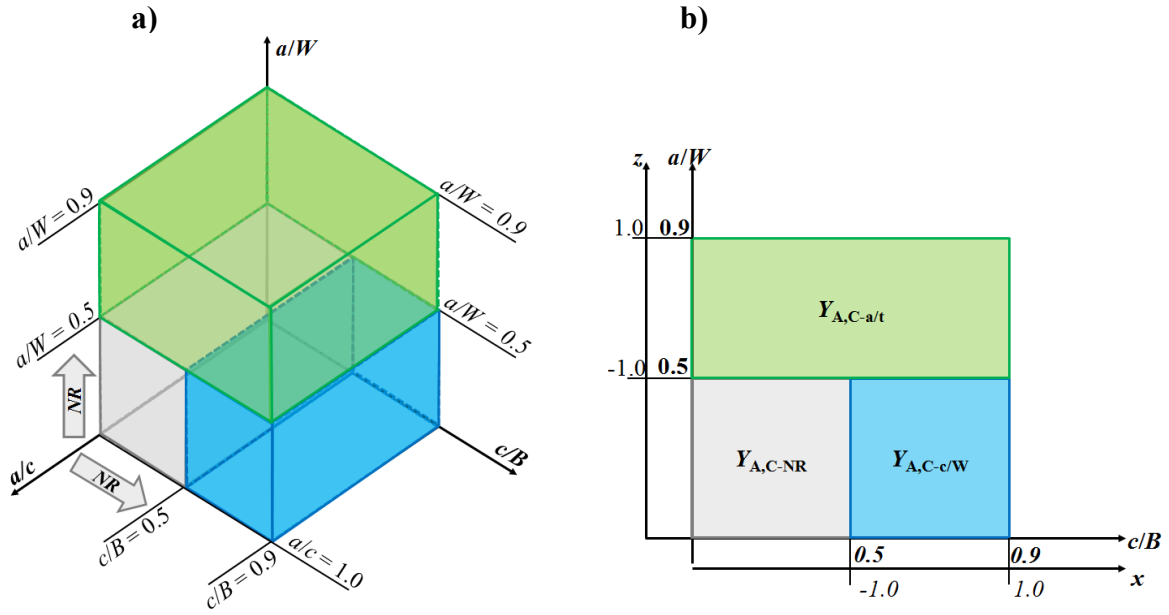

Fig. 50.: Area of validity and enhancement of the geometry function depending on the a/c, a/W and c/B ratios and introduction of the auxiliary variables x and z characterizing the boundaries.

To this purpose, two auxiliary variables x and z are introduced for simplicity, each ranging from -1 to 1 for the relevant c/B and a/W ranges, cf. Fig. 50 a).

In Fig. 50 b) the geometry function Y depends on the ratios a/W and c/B. The extension of c/B (blue area) follows the characterization variable x which is -1 for $c/B = 0.5$ at the boundary of the NR equation and 1 for $c/B = 0.9$ (the highest c/B value for which FE results are available).

To consider high a/W ratios (green area), the characterization variable z is introduced, equaling -1 at $a/W = 0.5$ and 1 at $a/W = 0.9$.

To generate a new prediction for the geometry function Y for different loadings, depending on all geometry ratios shown in Table 5, a statistical analysis with a linear regression model [85] and the method of least squares is conducted. The results of the empirical equations for different loadings are specified below (Sections 4.2.3.1 - 0, Eqns. 4.6 - 4.35).

4.2.3.1. Tension F_z

Enhancement for high ratios 0.5 < c/B ≤ 0.9

The geometry function is decomposed into a linear interpolation $Y_{\mathrm{A,C\text{-}lin\text{-}c/B\text{-}Fz}}$ and a higher order term $\Delta Y_{\mathrm{A,C\text{-}c/B\text{-}Fz}}$ for $0.5 < c/B < 0.9$,

$$Y_{\mathrm{A,C-c/B-Fz}} = Y_{\mathrm{A,C\text{-}lin\text{-}c/B\text{-}Fz}} + \Delta Y_{\mathrm{A,C\text{-}c/B\text{-}Fz}} \,. \tag{4.7}$$

For the linear interpolation between the NR approach and the solution at $c/B = 0.9$, the auxiliary variable x (Eq. 4.9) is used:

$$Y_{\mathrm{A,C-lin-c/B-Fz}} = Y_{\mathrm{A,C\text{-}NR\text{-}Fz}} \cdot \left(\frac{1-x}{2}\right) + Y_{\mathrm{A,C\text{-}Fz}}\left(\frac{c}{B} = 0.9\right) \cdot \left(\frac{1+x}{2}\right) \tag{4.8}$$

$$x = 4 \cdot \frac{c}{B} - \frac{7}{2} \,. \tag{4.9}$$

Here, the solutions at the boundaries are given by the NR solution (shown in the Appendix A) $Y_{\mathrm{A,C\text{-}NR\text{-}Fz}}$ at $x = -1$(i.e., $c/B = 0.5$) and by the following approximation functions determined by linear regression from the FE results at $x = -1$ (i.e., $c/B = 0.9$):

$$\begin{aligned} Y_{\mathrm{A\text{-}Fz}}\left(\frac{c}{B} = 0.9\right) = {} & 1.31 - 1.42 \cdot \frac{a}{c} + 0.94 \cdot \left(\frac{a}{c}\right)^2 + 4.9 \cdot \left(\frac{a}{W}\right)^2 - 3.73 \cdot \left(\frac{a}{W}\right)^3 - \\ & 4.66 \cdot \left(\frac{a}{c}\right)^2 \cdot \left(\frac{a}{W}\right)^2 + 3.77 \cdot \left(\frac{a}{c}\right)^3 \cdot \left(\frac{a}{W}\right)^3 \end{aligned} \tag{4.10}$$

$$\begin{aligned} Y_{\mathrm{C\text{-}Fz}}\left(\frac{c}{B} = 0.9\right) = {} & 0.25 + 1.47 \cdot \frac{a}{c} - 0.72 \cdot \left(\frac{a}{c}\right)^2 + 2.21 \cdot \left(\frac{a}{W}\right)^2 + 1.04 \cdot \frac{a}{c} \cdot \frac{a}{W} - \\ & 1.76 \cdot \left(\frac{a}{c}\right)^2 \cdot \left(\frac{a}{W}\right)^2 \end{aligned} \tag{4.11}$$

The higher order terms $\Delta Y_{\mathrm{A\text{-}c/B\text{-}Fz}}$ and $\Delta Y_{\mathrm{C\text{-}c/B\text{-}Fz}}$ for point A (Eq. 4.12) and C (Eq. 4.13) are fitted by polynomial functions whose parameters are determined by means of linear regression from the difference between FE results and linear approximation for $0.5 < c/B < 0.9$.

$$\Delta Y_{\mathrm{A-c/B\text{-}Fz}} = \left(x^2 - 1\right) \cdot \left(\frac{a}{W}\right)^2 \cdot 0.15 \tag{4.12}$$

$$\Delta Y_{\mathrm{C-c/B\text{-}Fz}} = \left(x^2 - 1\right) \cdot \left(\frac{a}{c}\right)^2 \cdot 0.12 + \left(x^2 - 1\right) \cdot \left(\frac{a}{W}\right)^2 \cdot 0.59 \tag{4.13}$$

Enhancement for high ratios 0.5 < a/W ratios ≤ 0.9

Similar to the enhanced formulation for higher c/B ratios, the extension is here done for the range $0.5 < a/W \leq 0.9$. Using the values from Eqns 4.7 - 4.13 for $a/W = 0.5$ and a statistically determined function for $Y_{\mathrm{A,C\text{-}Fz}}$ (a/W = 0.9) extracted from the FE results, the geometry function can then be calculated as follows:

$$Y_{\mathrm{A,C-a/W-Fz}} = Y_{\mathrm{A,C\text{-}lin\text{-}a/W-Fz}} + \Delta Y_{\mathrm{A,C\text{-}a/W\text{-}Fz}} \tag{4.14}$$

$$Y_{\mathrm{A,C-lin-a/W-Fz}} = Y_{\mathrm{A,C\text{-}c/B\text{-}Fz}} \cdot \left(\frac{1-z}{2}\right) + Y_{\mathrm{A,C\text{-}Fz}}\left(\frac{a}{W} = 0.9\right) \cdot \left(\frac{1+z}{2}\right) \tag{4.15}$$

with the variable z

$$z = 5 \cdot \frac{a}{W} - \frac{7}{2} \tag{4.16}$$

and the statistically determined functions at a/W = 0.9 for points A (Eq. 4.17) and C (Eq. 4.18).

$$Y_{\mathrm{A-Fz}}\left(\frac{a}{W} = 0.9\right) = 2.8 - 6.35 \cdot \frac{a}{c} + 7.28 \cdot \left(\frac{a}{c}\right)^2 - 2.95 \cdot \left(\frac{a}{c}\right)^3 + 0.56 \cdot \left(\frac{c}{B}\right)^3 - 0.46 \cdot \left(\frac{a}{c}\right)^2 \cdot \left(\frac{c}{B}\right)^2 \tag{4.17}$$

$$Y_{\mathrm{C-Fz}}\left(\frac{a}{W} = 0.9\right) = 0.96 + 2.34 \cdot \frac{a}{c} - 4.62 \cdot \left(\frac{a}{c}\right)^2 + 2.8 \cdot \left(\frac{c}{B}\right)^2 + 2.34 \cdot \left(\frac{a}{c}\right)^3 - 7.7 \cdot \left(\frac{c}{B}\right)^3 + 7.23 \cdot \left(\frac{c}{B}\right)^4 \tag{4.18}$$

Finally, the higher order terms for the ranges $0.5 < a/W \leq 0.9$, $0 < c/B \leq 0.9$ and $0 < a/c \leq 1.0$ can then be described for points A (Eq. 4.19) and C (Eq. 4.20) as

$$\Delta Y_{\mathrm{A-a/W\text{-}Fz}} = \left(z^2 - 1\right) \cdot \left(\frac{a}{c}\right)^2 \cdot 0.18 - \left(z^2 - 1\right) \cdot \left(\frac{a}{c}\right)^3 \cdot 0.19 - \left(z^2 - 1\right) \cdot \left(\frac{c}{B}\right)^3 \cdot 0.06 \tag{4.19}$$

$$\Delta Y_{\mathrm{C-a/W-Fz}} = \left(z^2 - 1\right)\cdot 0.19 - \left(z^2 - 1\right)\cdot\left(\frac{a}{c}\right)^2 \cdot 0.72 + \left(z^2\text{-}1\right)\cdot\left(\frac{a}{c}\right)^3 \cdot 0.52 + \left(z^2 - 1\right)\cdot\left(\frac{c}{B}\right)^3 \cdot 0.29 \quad 4.20$$

Regarding pure tension and symmetry, points C_1 and C_2 have the same applied stress and hence the same value for the geometry factor.

4.2.3.2. Bending M_x

The same approach as above is used for bending around the x-axis for $0.5 < c/B \leq 0.9$ and $0.5 < a/W \leq 0.9$:

Enhancement of 0.5 < c/B ≤ 0.9

$$Y_{\mathrm{A,C-c/B-M}x} = Y_{\mathrm{A,C\text{-}lin\text{-}c/B-Mx}} + \Delta Y_{\mathrm{A,C\text{-}c/B\text{-}Mx}} \quad 4.21$$

$$Y_{\mathrm{A,C-lin-c/B-M}x} = Y_{\mathrm{A,C\text{-}NR\text{-}Mx}} \cdot \left(\frac{1-x}{2}\right) + Y_{\mathrm{A,C\text{-}Mx}}\left(\frac{c}{B} = 0.9\right)\cdot\left(\frac{1+x}{2}\right) \quad 4.22$$

$$Y_{\mathrm{A\text{-}Mx}}\left(\frac{c}{B} = 0.9\right) = 1.23 - 0.81\cdot\frac{a}{c} - 1.13\cdot\frac{a}{W} + 0.37\cdot\left(\frac{a}{c}\right)^2 + 2.91\cdot\left(\frac{a}{W}\right)^2 - 2.88\cdot\left(\frac{a}{W}\right)^3 - 1.79\cdot\left(\frac{a}{c}\right)^2\cdot\left(\frac{a}{W}\right)^2 + 1.81\cdot\left(\frac{a}{c}\right)^3\cdot\left(\frac{a}{W}\right)^3 \quad 4.23$$

$$Y_{\mathrm{C\text{-}Mx}}\left(\frac{c}{B} = 0.9\right) = 0.12 + 2.77\cdot\frac{a}{c} - 0.28\cdot\frac{a}{W} - 3.07\cdot\left(\frac{a}{c}\right)^2 + 2.54\cdot\left(\frac{a}{W}\right)^2 + 1.3\cdot\left(\frac{a}{c}\right)^3 - 1.34\cdot\left(\frac{a}{W}\right)^3 - 0.65\cdot\left(\frac{a}{c}\right)^2\cdot\left(\frac{a}{W}\right)^2 \quad 4.24$$

$$\Delta Y_{\mathrm{A-c/B\text{-}Mx}} = -\left(x^2 - 1\right)\cdot\left(\frac{a}{c}\right)^2 \cdot 0.02 + \left(x^2 - 1\right)\cdot\left(\frac{a}{W}\right)^2 \cdot 0.1 + \left(x^2 - 1\right)\cdot\left(\frac{c}{B}\right)^2 \cdot 0.04 \quad 4.25$$

$$\Delta Y_{\mathrm{C-c/B\text{-}Mx}} = \left(x^2 - 1\right)\cdot\left(\frac{a}{c}\right)^2 \cdot 0.07 + \left(x^2 - 1\right)\cdot\left(\frac{a}{W}\right)^2 \cdot 0.33 \quad 4.26$$

Enhancement of 0.5 < a/W ≤ 0.9

$$Y_{\mathrm{A,C-a/W-Mx}} = Y_{\mathrm{A,C\text{-}lin\text{-}a/W-Mx}} + \Delta Y_{\mathrm{A,C\text{-}a/W\text{-}Mx}} \tag{4.27}$$

$$Y_{\mathrm{A-lin-a/W-Mx}} = Y_{\mathrm{A,C\text{-}c/B\text{-}Mx}} \cdot \left(\frac{1-z}{2}\right) + Y_{\mathrm{A,C\text{-}Mx}}\left(\frac{a}{W} = 0.9\right) \cdot \left(\frac{1+z}{2}\right) \tag{4.28}$$

$$Y_{\mathrm{A-Mx}}\left(\frac{a}{W} = 0.9\right) = 0.11 - 0.8 \cdot \frac{a}{c} - 0.09 \cdot \frac{c}{B} + 0.47 \cdot \left(\frac{a}{c}\right)^2 + 0.55 \cdot \left(\frac{c}{B}\right)^2 - 0.89 \cdot \frac{a}{c} \cdot \left(\frac{c}{B}\right)^2 + 0.49 \cdot \left(\frac{a}{c}\right)^2 \cdot \left(\frac{c}{B}\right)^2 \tag{4.29}$$

$$Y_{\mathrm{C-Mx}}\left(\frac{a}{W} = 0.9\right) = 0.8 - 0.66 \cdot \left(\frac{c}{B}\right)^2 - 0.13 \cdot \left(\frac{a}{c}\right)^3 + 1.69 \cdot \left(\frac{c}{B}\right)^3 \tag{4.30}$$

$$\Delta Y_{\mathrm{A-a/W\text{-}Mx}} = -\left(z^2 - 1\right) \cdot 0.27 + \left(z^2 - 1\right) \cdot \left(\frac{a}{c}\right)^2 \cdot 0.13 \tag{4.31}$$

$$\Delta Y_{\mathrm{C-a/W\text{-}Mx}} = -\left(z^2 - 1\right) \cdot \left(\frac{a}{c}\right)^2 \cdot 0.08 + \left(z^2 - 1\right) \cdot \left(\frac{c}{B}\right)^3 \cdot 0.14 \tag{4.32}$$

4.2.3.3. Bending M_y

For bending around the y-axis, a new function for the geometry factor has to be developed. Based on the symmetry shown in Fig. 49 b), Y_A is situated on the neutral axis under the bending load M_y and therefore is consequently zero, independent of the geometry ratio:

$$Y_{\mathrm{A\text{-}My}} = 0 \tag{4.33}$$

Assuming a positive bending moment M_y, point C_1 is under tensile and point C_2 is under compressive stress, shown in Fig. 49 b). The distance of both points to the neutral axis is equal; therefore the magnitude is also the same, only the sign changes from positive to negative.

$$Y_{C2\text{-}My} = -Y_{C1\text{-}My} \tag{4.34}$$

$$Y_{C1\text{-}My} = 0.128 \cdot \left(\frac{a}{c}\right)^2 + 1.165 \cdot \left(\frac{c}{B}\right)^2 - 0.126 \cdot \left(\frac{a}{c}\right)^3 - 0.587 \cdot \left(\frac{c}{B}\right)^3 + 0.307 \cdot \left(\frac{a}{W}\right)^2 \cdot \left(\frac{c}{B}\right)^2 - 0.303 \cdot \left(\frac{a}{c}\right)^2 \cdot \left(\frac{a}{W}\right)^2 \cdot \left(\frac{c}{B}\right)^2 \tag{4.35}$$

The residual standard errors for the new empirical equations appear acceptable for all different loadings. On this basis, the new geometry functions are now compared with all FE results in order to verify their range of validity.

4.2.4. Comparison of results for the new approximate geometry factor solutions

In Fig. 51 -Fig. 53, the new approximate solutions for Y are compared to the FE results. The different marks denote different ratios a/W for Y_A and c/B for Y_C the same way as in section 4.2.2. The full lines represent again the exact prediction, the dashed lines 10% and 20% over-prediction and the dotted lines 10% resp. 20% under-prediction respectively.

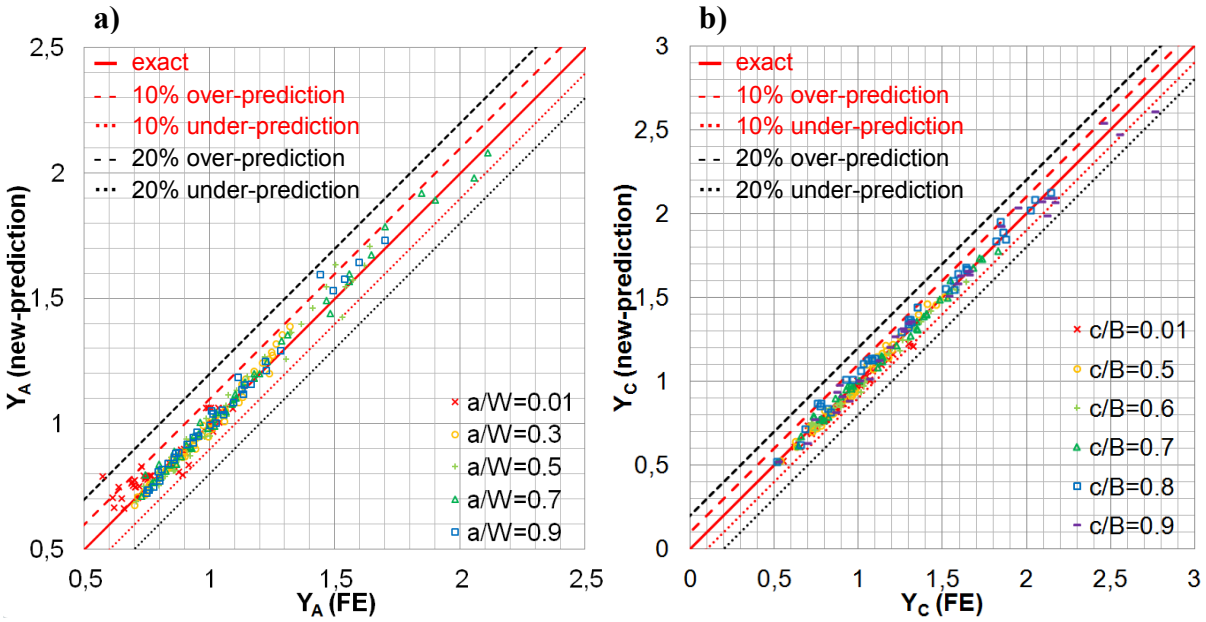

Fig. 51.: Comparison of the FE results with the new approximate solution for pure tension F_z a) all results for point A and color/symbol distinction of a/W; b) all results for point C (C = C_1 = C_2) and color/symbol distinction of c/B.

Due to the region-wise approximation, the prediction in the original region of validity ($0 \leq c/B \leq 0.5$ and $0 \leq a/W \leq 0.5$) is unchanged by the NR equations. For higher c/B and a/W ratios the prediction is now more precise and lies within an error band of ±20% for all and ±10% for most cases.

Fig. 52 shows that the new formulas give a very satisfactory estimate of the FE results for a bending moment M_x. Most importantly, the new prediction works well for high a/W ratios, where point A is beyond the neutral axis.

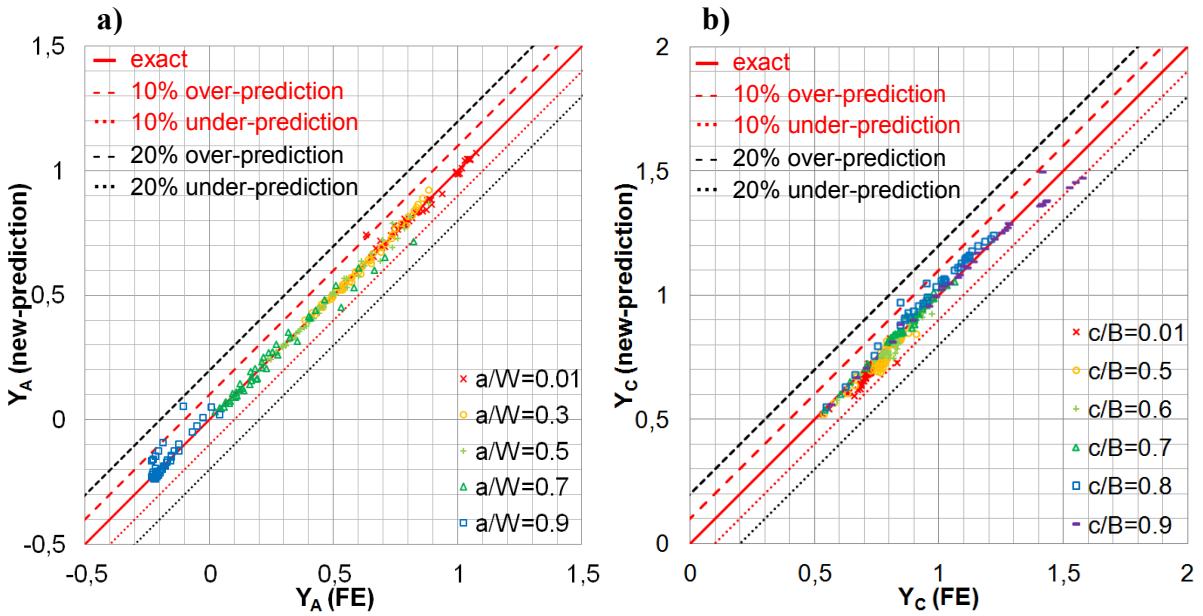

Fig. 52.: Comparison of the FE results with the new approximate solution for bending M_x a) all results for point A and color/symbol distinction of a/W; b) all results for point C ($C = C_1 = C_2$) and color/symbol distinction of c/B.

In Fig. 52 it can be observed that for bending with the moment M_y, the prediction for point C fits within a maximum error of ±5% to the FE results. As mentioned, Y_A is constantly zero due to the position of point A on the neutral axis (Fig. 49 b).

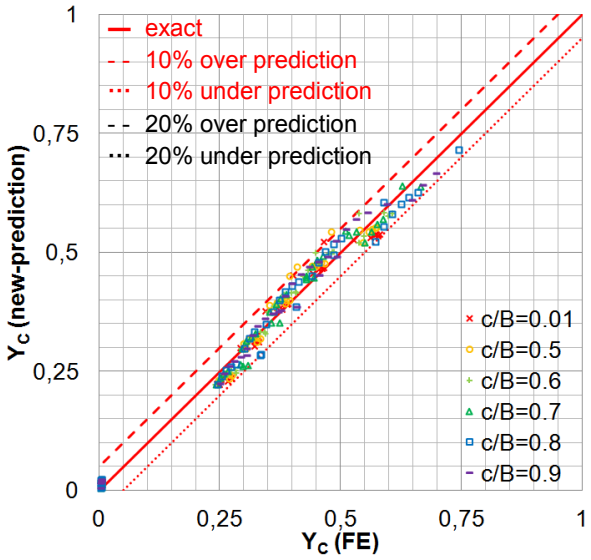

Fig. 53.: Comparison of the FE results with the new approximate solution for bending M_y for point C (C = C_1 = C_2) and color/symbol distinction of c/B.

In this way the crack growth in a rails can so analytically be estimated with the enhanced formulation, even for cracks close to the boundary of the rail and different loading conditions.

5. Influence of the notch parameter on crack growth

The estimation of the lifetime of notched components is an important technical issue. Notches significantly reduce the lifetime of cyclically loaded components with cracks due to their stress concentration and early crack initiation. The lifetime can be subdivided into a crack initiation and a crack growth period. In order to specify inspection intervals, the information about the initiation and crack growth periods will be essential.

For this purpose, single edge notched bending (SENB) specimens are manufactured with two different notch geometries and two different load levels are applied until failure. For measuring the crack length during the experiment, the direct current potential drop (DCPD) technique was used. In [6] and [7] a method is proposed to determine the crack initiation as well as the crack growth lifetime within a conventional fracture mechanics setup.

The influence of notches on the fatigue limit and crack propagation have been studied since years. An interesting work on this topic, considering circumferential notched bars in torsion and tension is presented by Tanaka [86]. In this study the crack initiation and end of lifetime is determined for different notch radii using the DCPD method for the measurement of the crack length. The results indicate, the higher the notch radius is the lower is the lifetime and the lower is the crack propagation in the first stage. Berto [87] reanalyzed the results using the strain energy density method of Lazzarin and Zambardi [88]and provides a good prediction of the experimental results of Tanaka.

The consequences of the notch concentration on the endurance limit and Woehler curves is presented by Atzori [89], where approaches of the general notch mechanic and fracture mechanics are compared. Based on the suggestions of Glinka [90], Atzori [91] provides analytical equations of the stress distribution of U- and V-shaped notches, considering bending and tension loads.

The DCPD method is commonly used to determine the initiation and propagation of cracks. Nevertheless, the change of the electrical potential depends on the measuring position, the specimen and notch geometry and calibrations based on experimental results [92], [93] or using finite element simulations [94] are recommended.

5.1. Fatigue experiments of notched specimens

SENB specimens with two different notch geometries are tested at two different load levels $\Delta\sigma_{notch}$, each in a four-point bending device, shown in Fig. 15.

The stress range $\Delta\sigma_{notch}$ at the notch tip is given by the applied bending stress range $\Delta\sigma_{appl}$ and the notch shape factor α_k from Eq. 1.14.

$$\Delta\sigma_{notch} = \Delta\sigma_{appl} \cdot \alpha_k \qquad 5.1$$

The tested material is a pearlitic steel with a tensile strength of 1070 MPa. The height of the specimens is $W = 20$ mm, the width $B = 0.15 \cdot W$ and the length $L = 5.5 \cdot W$. Due to a different notch width $2 \cdot \rho$, the measuring distance $2 \cdot y$ for the electric potential drop ΔU varies depending on the notch radius (Fig. 1).

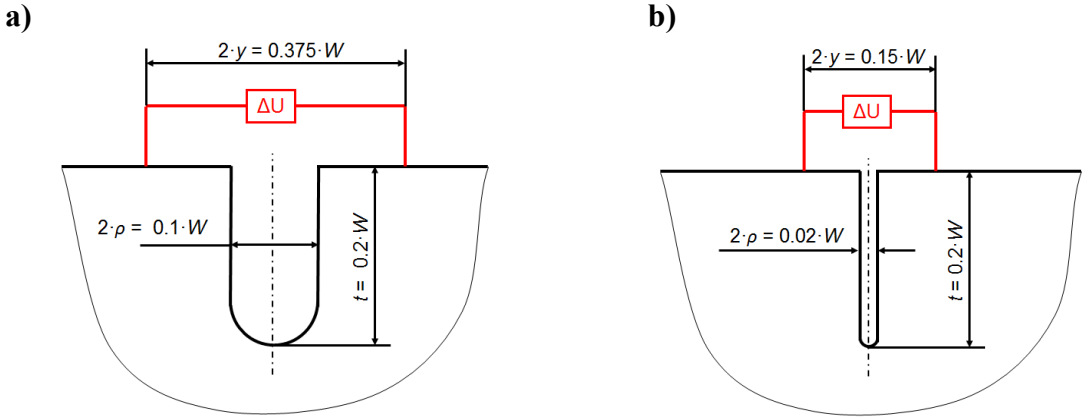

Fig. 54.: Schematic representation of the notch geometries and distances of the measuring points of the DCPD method. a) mild notch and b) sharp notch.

In Fig. 54 a) the *mild* notch with a depth $t = 0.2 \cdot W$, a notch radius $\rho = 0.05 \cdot W$ and a measuring distance $2 \cdot y = 0.375 \cdot W$ and in Fig. 54 b) the *sharp* notch with a depth $t = 0.2 \cdot W$, a notch radius of $\rho = 0.01 \cdot W$ and measuring distance $2 \cdot y = 0.15 \cdot W$ mm are displayed.

All specimens were subjected to cyclic loading with a constant load ratio $R = 0.1$. By using the direct current potential drop (DCPD) method and the formulation of Johnson [60] and Schwalbe [61] assuming a straight through-thickness crack, the crack length can be computed.

In Fig. 55 the experimental results for the crack length as a function of the number of cycles are displayed for the different notch geometries.

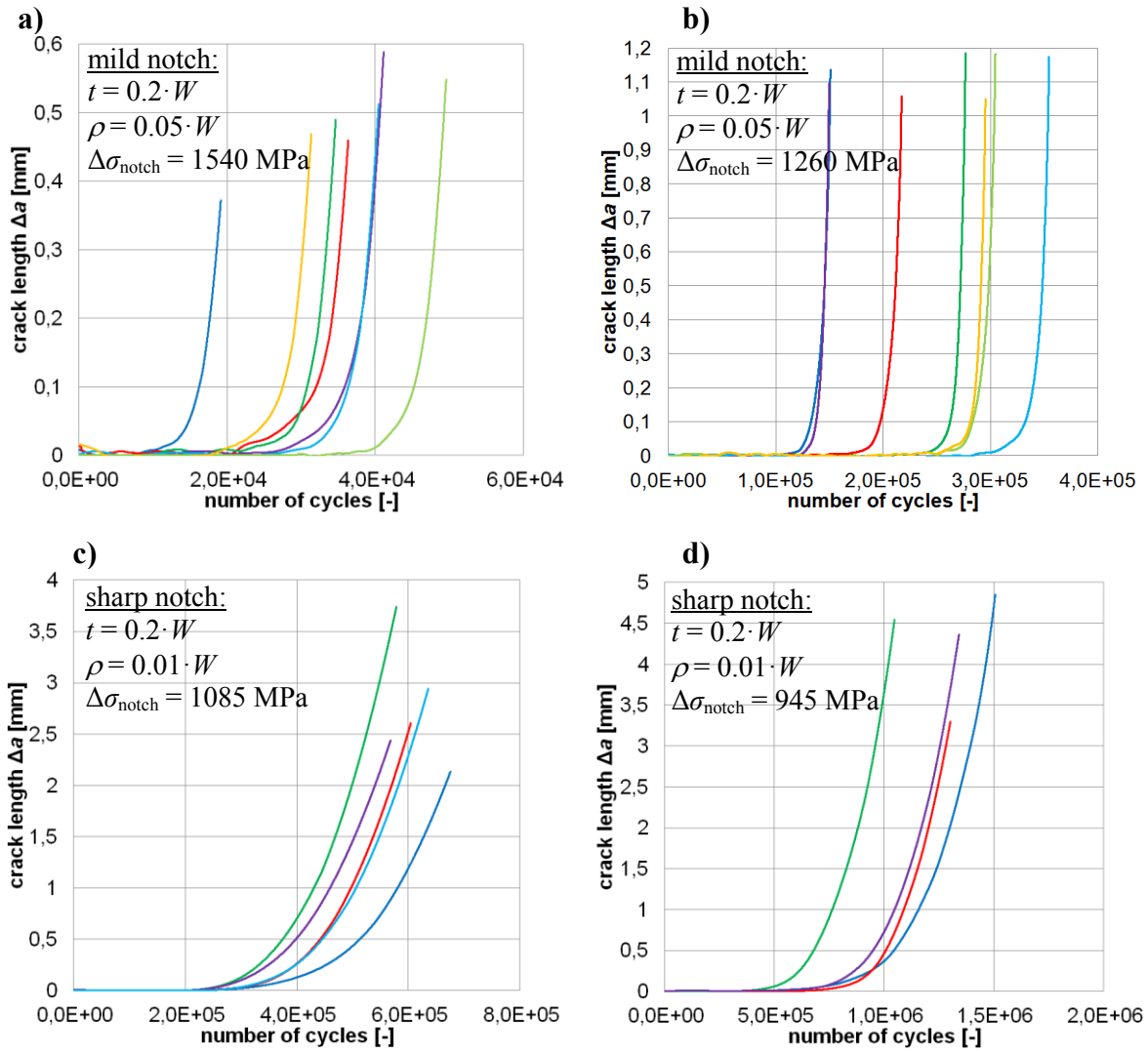

Fig. 55.: Crack growth curves between initiation and failure: (a) $\rho = 0.05 \cdot W$, $t = 0.2 \cdot W$ and $\Delta\sigma_{notch}$ = 1540 MPa; (b) $\rho = 0.05 \cdot W$, $t = 0.2 \cdot W$ and $\Delta\sigma_{notch}$ = 1260 MPa; (c) $\rho = 0.01 \cdot W$, $t = 0.02 \cdot W$ and $\Delta\sigma_{notch}$ = 1085 MPa; (d) $\rho = 0.01 \cdot W$, $t = 0.02 \cdot W$ and $\Delta\sigma_{notch}$ = 945 MPa.

It can be seen that in general the crack growth period for a given notch geometry and applied stress is nearly the same. The crack initiation varies within the same notch geometry and applied load, supposedly depending on the initiation site. Judging from these results – obtained by assuming a straight through-thickness crack, the initiation period is a major part of the total lifetime.

5.2. The shape of the crack and deviation from the Johnson approach

Using the DCPD method with the Johnson equation [60] assumes a straight through-thickness crack front. Nevertheless, experiments stopped at some cycles, show a semi-elliptical crack front on the fracture surface. To estimate the short crack growth behavior, starting with a semi-elliptical crack shape, several experiments have been conducted and stopped at crack lengths $\Delta a \leq a_f$, where a_f denotes the crack length at failure. The analyzed fracture surfaces of selected experiments are displayed in Fig. 56, where the dimensions of approximated semi-elliptical cracks of depth Δa and width $2 \cdot c$ are shown.

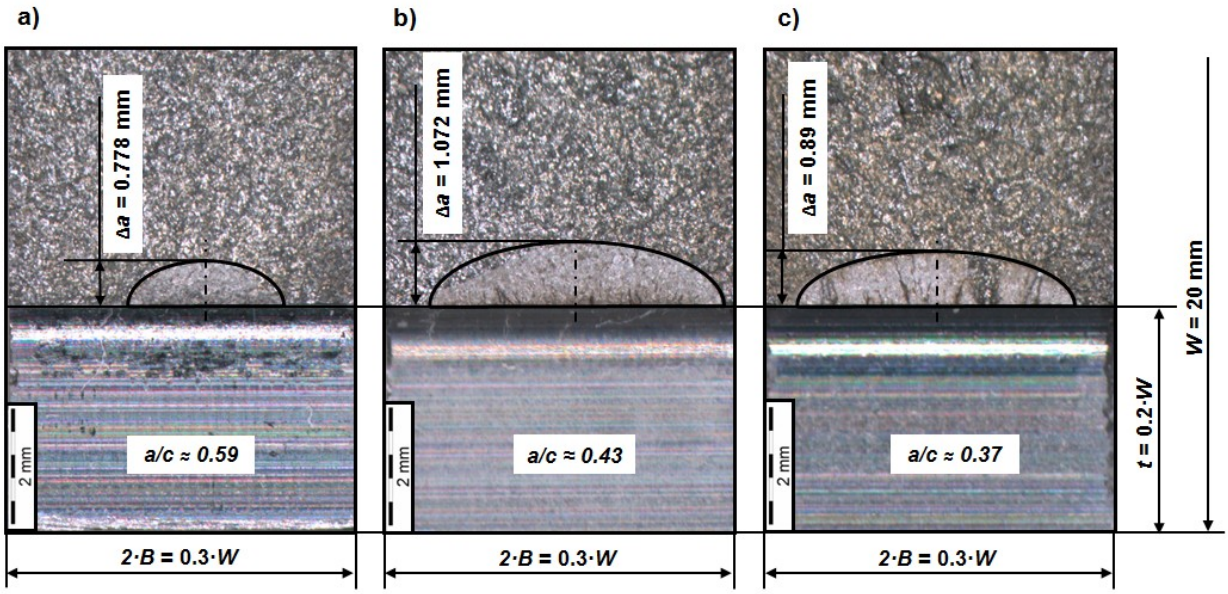

Fig. 56.: Light microscopic fracture surface analysis of interrupted experiments and measured crack length for a) $\Delta a_{Johnson} = 0.1$ mm, b) $\Delta a_{Johnson} = 0.25$ mm and c) $\Delta a_{Johnson} = 0.2$ mm, the fractographs clearly illustrate the very large underestimation of the crack length by the Johnson approximation.

The experiments have been stopped at different pre-defined lengths of a fictitious straight through-thickness cracks as estimated by the DCPD method and the Johnson equation [60]; here, for Fig. 56 a) 0.1 mm, Fig. 56 b) 0.25 mm and Fig. 56 c) 0.2 mm. In comparison to the analyzed real crack shape, the estimated straight crack length from the Johnson equation is markedly smaller than the actual depth of the semi-elliptical crack.

The influence of different crack shapes and the resulting measured potential drop ΔU was already investigated for different configurations by Riemelmoser [95]. Extending this work, several finite element (FE) simulations were performed to determine the potential drop ΔU for different configurations of semi-elliptical cracks with respect to the specimen dimensions,

where the focus was set on different ratios $\Delta a/c$ and c/B to estimate the transition from the semi-elliptical to the straight (through-thickness) crack front. In addition, the difference between the crack growth of a single and a double semi-elliptical crack is worked out.

In Fig. 57 the schematic cross sections for determination of the normalized potential drop $\Delta U/U_0$ is displayed. The geometry configurations were performed for different crack lengths for ratios in-between $0.3 \leq \Delta a/c \leq 1.0$, $0 \leq c/B \leq 1.0$ and $0.1 \leq t/W \leq 0.3$.

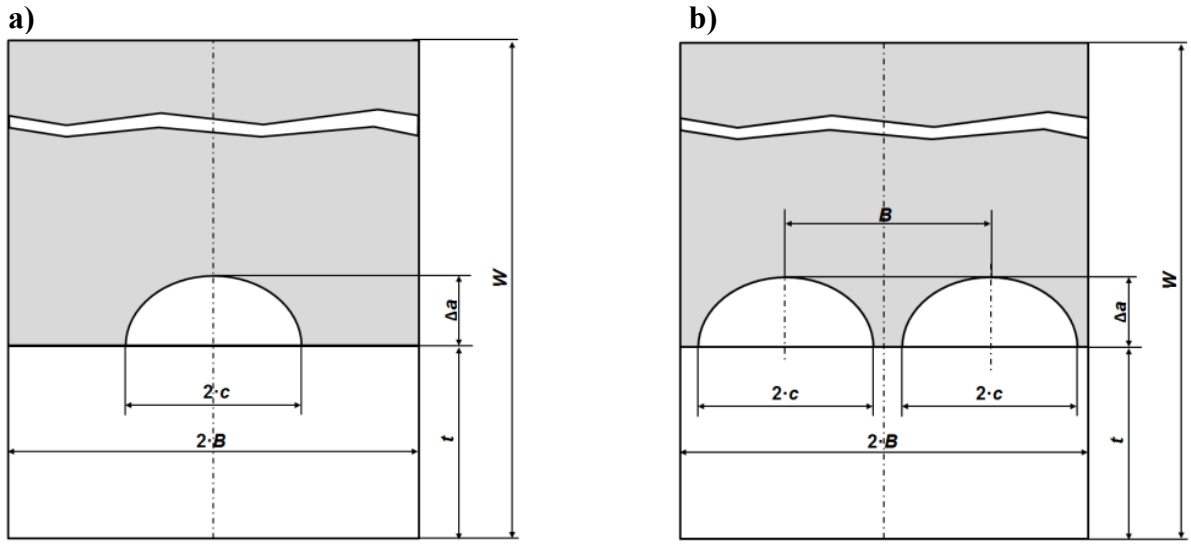

Fig. 57.: Schematic sections in the crack plane for the determination of the normalized potential drop $\Delta U/U_0$ in the DCPD method: a) single, b) double ellipse.

In Fig. 58 the results of the normalized potential drop $\Delta U/U_0$ as a function of the crack length Δa are exemplarily displayed for the notch geometries from the experiments ($t/W = 0.2$ and $\rho/W = 0.05$ resp. $\rho/W = 0.01$); a) for the *mild* notch and a single crack, b) for the *sharp* notch and a single crack, c) for the *mild* notch and a double crack and d) for the *sharp* notch and a double crack. The different marks represent different $\Delta a/c$ ratios and for comparison, the black circles show the results for the straight through-thickness crack. Additionally the solution from the Johnson equation is displayed by the dashed black lines.

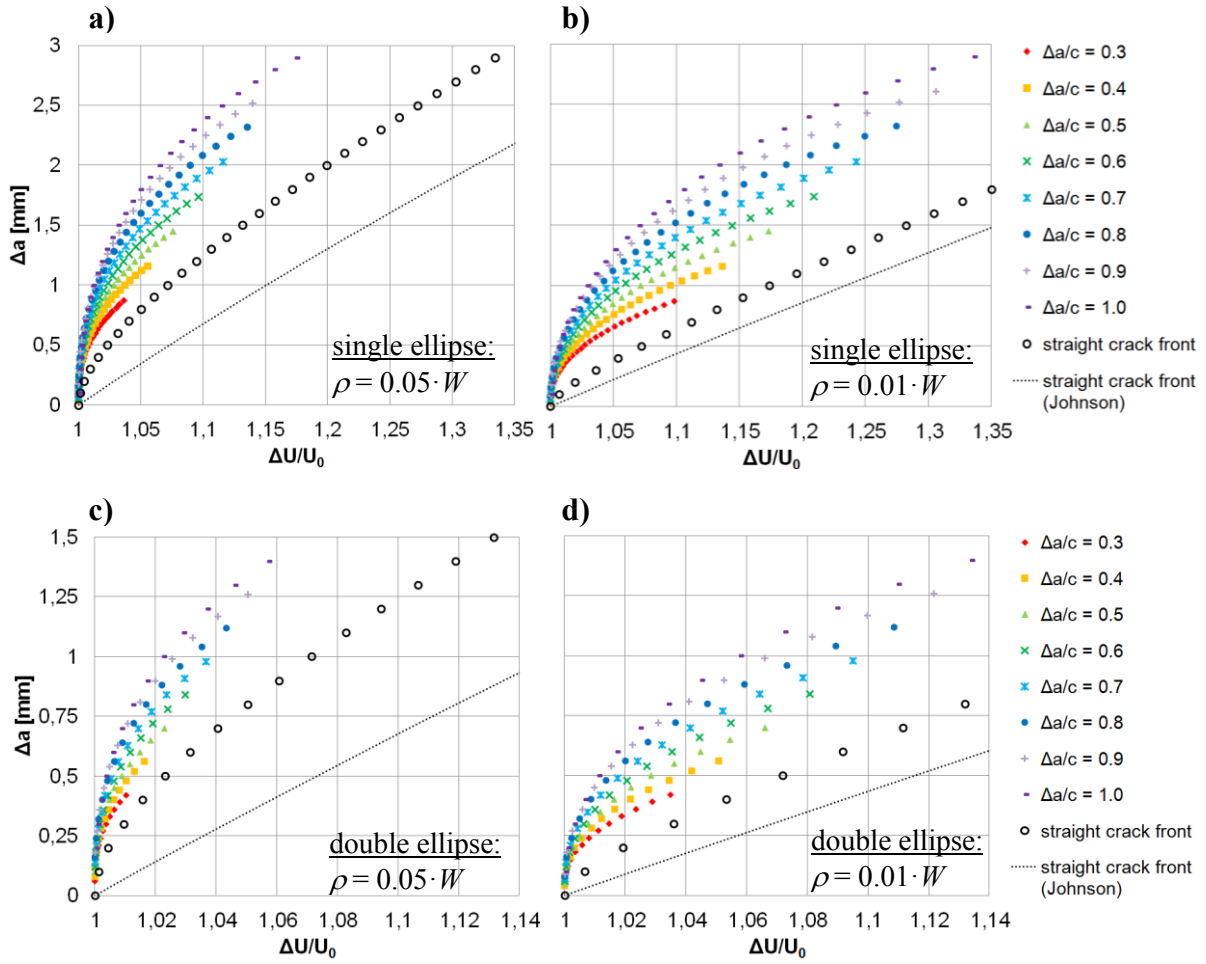

Fig. 58.: Comparison of the normalized potential drop for different crack and specimen geometries with a straight crack front and the solution derived from the Johnson equation. Exemplarily shown for different ratios $\Delta a/c$ and $t/W = 0.2$ a) for $\rho/W = 0.05$ and b) $\rho/W = 0.01$, both for a single crack; c) for $\rho/W = 0.05$ and d) $\rho/W = 0.01$, both for a double crack.

The different combinations in Fig. 58 clearly show that the fictitious straight crack length clearly underestimates the actual crack depth. Even with the straight crack front a difference between FE results (black cycles) and Johnson's prediction (black dots) is recognizable because the latter is only valid for an ideally sharp cracks and does not account for the notch radius and the distance of the notch flanks.

For designing a prediction of the potential $\Delta U/U_0$, a model based on linear regression model was devised [85]. The equations for different ratios ($\Delta a/c$, a/W, c/B, and t/W) can then be calculated by Eqns. 5.2 - 5.4 for the semi-elliptical crack and Eqns. 5.3- 5.5 for the straight crack front by using the parameters shown in Table 6.

The potential drop across the semi-elliptical crack or the two semi-elliptical cracks, respectively, is

$$\frac{\Delta U}{U_0} = 1 + C_1 \cdot q \cdot \frac{c}{B} + C_2 \cdot q \cdot \frac{t}{W} + C_3 \cdot q \cdot \frac{a}{W} + C_4 \cdot q \cdot \left(\frac{t}{W}\right)^2 + C_5 \cdot q \cdot \left(\frac{a}{W}\right)^2 + C_6 \cdot q \cdot \left(\frac{c}{B}\right)^3 + C_7 \cdot q \cdot \left(\frac{a}{W}\right)^3 \quad 5.2$$

where

$$q = \left(\frac{a}{W} - \frac{t}{W}\right) \quad 5.3$$

and a describes the added notch and crack length consisting of the fatigue crack extension Δa and the initial notch depth t,

$$a = \Delta a + t\,. \quad 5.4$$

The potential drop across the straight through-thickness crack is

$$\frac{\Delta U}{U_0} = 1 + C_1 \cdot q + C_2 \cdot q \cdot \frac{t}{W} + C_3 \cdot q \cdot \frac{a}{W} + C_4 \cdot q \cdot \left(\frac{t}{W}\right)^2 + C_5 \cdot q \cdot \left(\frac{a}{W}\right)^2 + C_6 \cdot q \cdot \left(\frac{a}{W}\right)^3. \quad 5.5$$

The range of validity of Eqns 5.2 and 5.5 is $0.1 \le a/W \le 0.7$, $0.1 \le t/W \le 0.3$, $0 \le c/B \le 1$.

Table 6: Parameters for prediction of the potential drop for a single and double semi-elliptical and a straight crack front.

Parameter	**mild notch ($\rho/W = 0.05$)**			**sharp notch ($\rho/W = 0.01$)**		
	1 ellipse	**2 ellipses**	**straight**	**1 ellipse**	**2 ellipses**	**straight**
C_1	0.53	0.49	0.92	2.07	3.11	8.19
C_2	-5.06	-7.72	-13.90	-24.46	-30.79	-59.83
C_3	3.85	6.53	17.21	27.94	32.52	20.47
C_4	4.58	6.12	11.63	49.18	61.19	88.65
C_5	0	0	-25.14	-86.88	-87.82	-32.62
C_6	0.48	3.15	16.51	0.80	6.10	23.00
C_7	-6.14	-9.62	-	76.26	61.00	-

In Fig. 59 the comparison of the FE results (horizontal axis) and the analytical prediction by Eqns 5.2 and 5.5 (vertical axis) is displayed. Here the blue marks represent the prediction for the *mild* notch and the red resp. yellow marks the *sharp* notch in a) for a single and a double semi-elliptical crack front and in b) for the straight crack front. Furthermore, the full black line represents the exact and the dashed and dotted lines the 2.5% in a) and 10% in b) over- and under- prediction of the FE results, respectively.

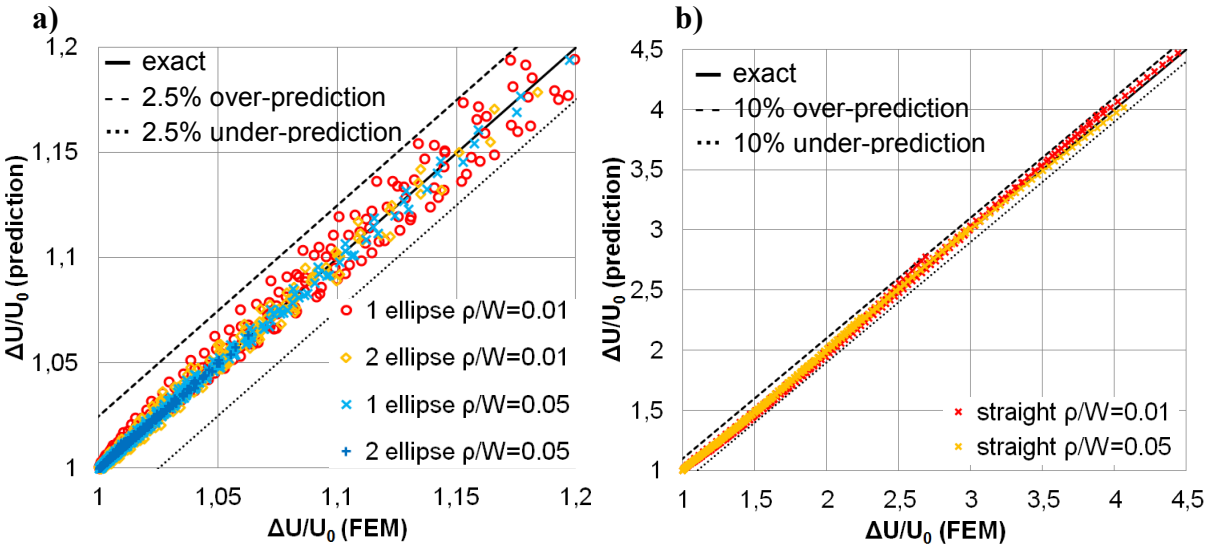

Fig. 59.: Comparison of the analytical prediction of the potential drop with the FE results and the 2.5%/10% over- and under-prediction scatter lines, respectively, in a) for the semi elliptical crack shape and b) the straight (through thickness) crack.

The comparison between the approximation and the FE results of the potentials in Fig. 59 shows an acceptable residual error of less than 2.5% for the single and double semi-elliptical cracks and 10% for the straight through-thickness crack.

To validate this approach, the new prediction is compared with the experiments depicted in Fig. 56. The depth of the semi-elliptical crack is computed from the potential drop via Eq. 5.2 using the $\Delta a/c$ ratio from the micrograph, and then compared with the actual crack length determined from the fracture surface (Fig. 60 and Table 7).

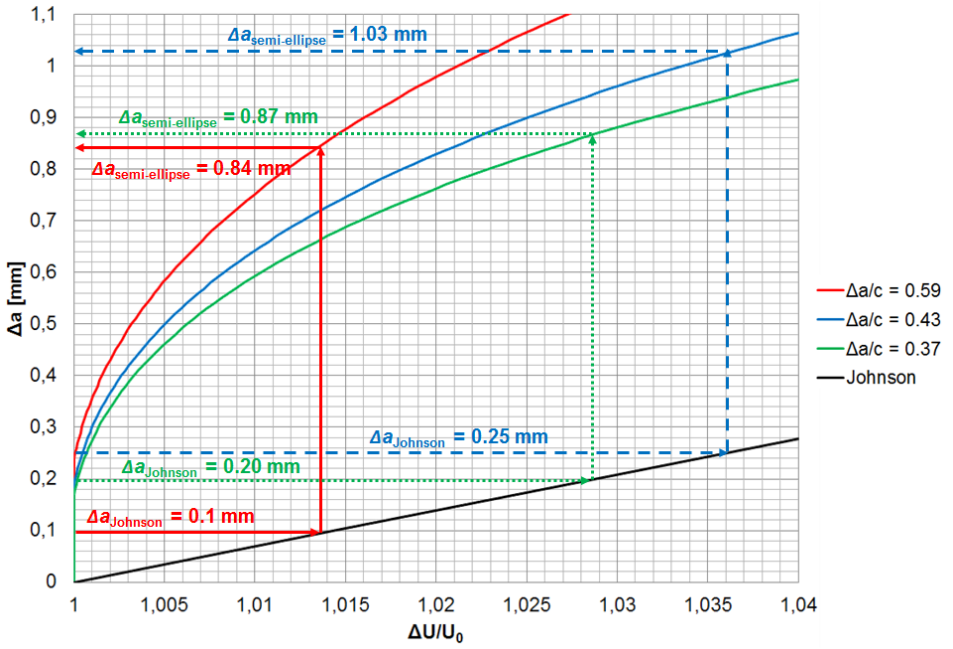

Fig. 60.:Comparison of crack lengths as estimated by the Johnson formula and by Eq. 5.2 for a semi-elliptical crack with $\Delta a/c$ from the micrograph Fig. 56.

Table 7: Comparison of crack lengths as estimated by the Johnson formula, by Eq. 5.2 and as determined from experiment.

sample	$\Delta a_{\text{Johnson}}$ **[mm]**	$\Delta a_{\text{semi-ellipse}}$ **[mm]**	$\Delta a_{\text{experiment}}$ **[mm]**
Fig. 56 a)	0.10	0.84	0.778
Fig. 56 b)	0.25	1.03	1.072
Fig. 56 c)	0.20	0.87	0.890

The predicted crack lengths using Eq. 5.2 are acceptably close to the actual crack lengths determined from the micrographs. Hence, Eqns. 5.2-5.4 will be used for the numerical prediction of the crack growth.

5.3. Numerical prediction of the crack growth from initiation to failure

5.3.1. Fracture mechanics experiments

After initiation, the fatigue crack growth can be calculated by commonly used fracture mechanics approaches. Here, the crack growth is described by a modified NASGRO equation (Eq. 1.42) and the NASGRO parameters are necessary. Therefore several fracture mechanics experiments with SENB specimens have been conducted and analysed statistically.

In Fig. 61 the results of cyclic fracture mechanics experiments of the pearlitic material, already shown in Fig. 38 and their statistical evaluation are shown. Different colors mark different load ratios R. Experimental results are illustrated by single dots, whereas the continuous and dashed lines represent the mean estimate as well as the upper and lower predictions (denoted by COV-up and COV-low) obtained by combining the respective upper (97.5%) and lower (2.5%) confidence limits of the parameters.

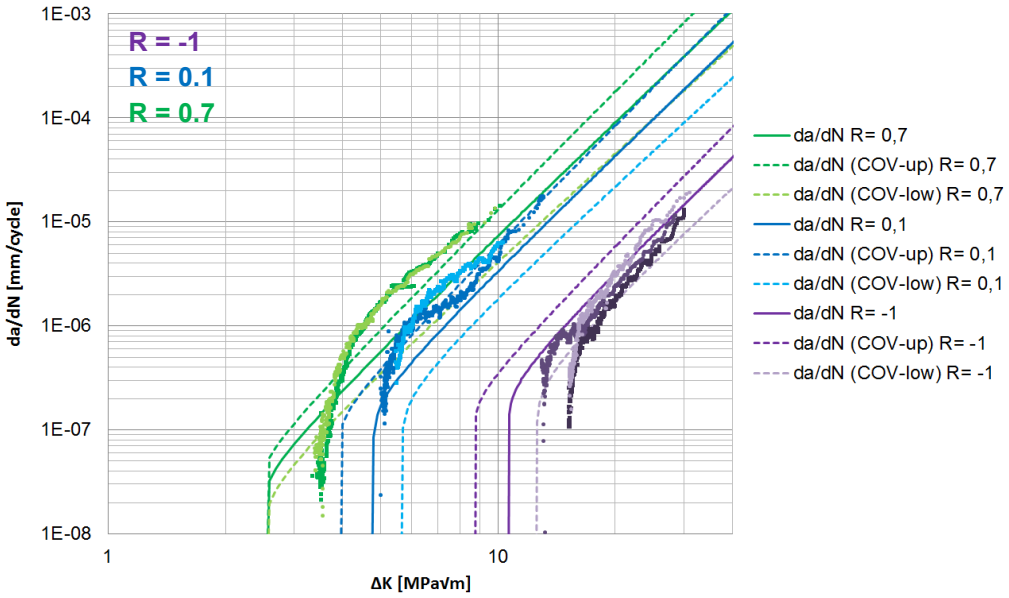

Fig. 61.: Experimentally determined and fitted da/dN-curves for different stress ratios.

It can be observed that the statistical analysis gives a good correlation at R = -1 but the resulting long crack threshold $\Delta K_{th,lc}$ is lower compared to the experiments. In this case the lower COV-curve fits best. In consideration of the stress ratios R = 0.1 and R = 0.7 the upper COV-curve represents the best estimate for the experimental results although the long crack threshold is lower compared to the experiments. For R = 0.1 the estimated long crack threshold fits best to the experiments.

To describe the crack growth threshold of physically short cracks, the cyclic crack resistance curve by Eq. 1.39 is used. The experimental results of the pealitic material, already shown in Fig. 37 and the analytical prediction are shown in Fig. 62. For the analytical description the proposal by Maierhofer [51] (Eq. 1.39) is used.

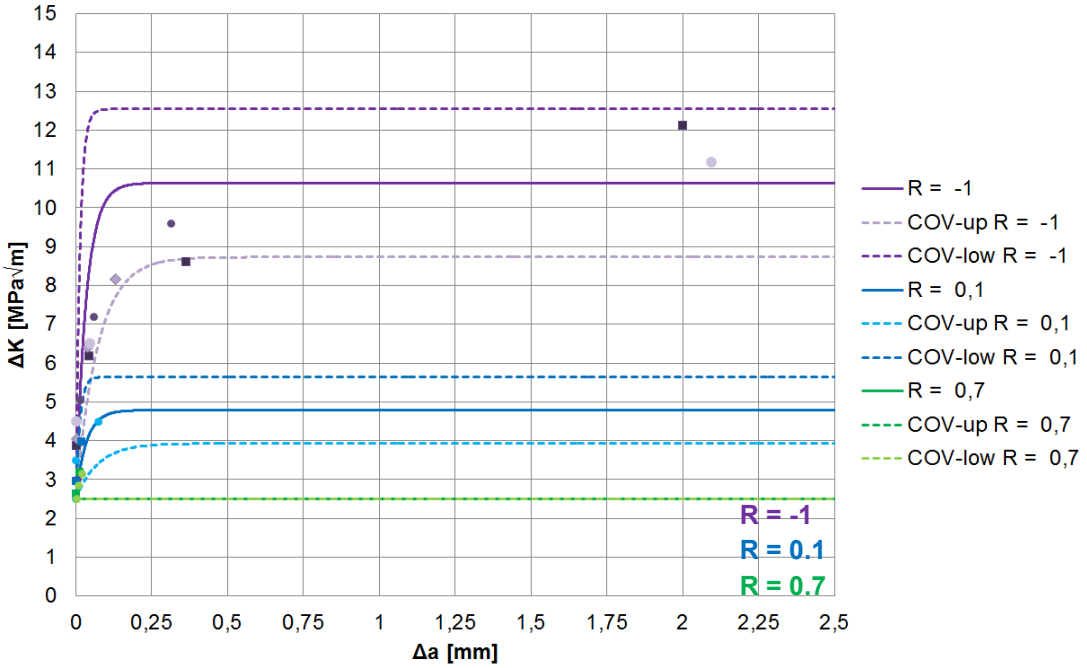

Fig. 62.: Experimentally determined and fitted cyclic crack resistance curves for the threshold of stress intensity factor range for different stress ratios.

The analytical estimate with mean curve and confidence limits is again represented by continuous and dashed lines. For the stress ratio $R = 0.1$, the mean curve fits well, whereas at $R = -1$ the lower confidence limit gives the best result in comparison to the experiments.

The parameters of the NASGRO equation obtained by the statistical analysis are listed in Table 8 and will be used for the further calculations of the crack propagation.

Table 8: NASGRO parameters of the statistical determination of the fatigue crack growth experiments:

Parameter	mean	COV upper	COV lower
$\Delta K_{th,lc}(R = 0)$ [MPa√m]	5.318	4.365	6.271
C [mm/cyc]	2.02E-9	2.42E-9	1.69E-9
m [-]	3.581	3.748	3.414
p [-]	0.198	0.149	0.248
l_1 [mm]	0.034	0.072	0.013

5.3.2. Crack growth of a notched specimen

The calculation of a crack starting from a notch is somewhat different from the one for a crack in a smooth specimen. As long as the crack extension is small and the crack tip is near the notch root, the crack tip loading is fully governed by the stress concentration at the notch root; as the crack propagates further, it grows out of the notch stress concentration, which leads to a reduction of the crack tip load.

Depending on the notch depth t and radius ρ, the geometry factor can be calculated by the approach from Neuber [96] for a straight crack. For a semi-elliptical shape, the equation has to be modified as follows:

$$Y_N(a) = Y_{A,C} \cdot \left\{ 1 + \left[(\alpha_k - 1)^{-2.5} + \left(\sqrt{\frac{t + \Delta a}{\Delta a}} - 1 \right)^{-2.5} \right]^{-0.4} \right\} \qquad 5.6$$

Here, $Y_{A,C}$ denotes the geometry factor for the semi-elliptical crack front at points A and C, respectively (cf. Fig. 45) and with the notch stress concentration factor from Eq. 1.7.

Therefore, the enhanced solution of the geometry factor for $0.5 \leq c/B \leq 0.9$ from point 4.2 which represents [5] is used.

5.3.3. Consideration of the load ratio R

As can be seen from Fig. 61 and Fig. 62, the load ratio R has a marked influence on the crack growth rate. In the notched specimens, cyclic plastic deformation at the notch root causes a long-range residual stress field in front of the notch whose extension depends on the notch acuity t/ρ. This residual stress field influences the local load ratio at the crack tip until the crack has grown beyond its range (the short-range crack tip plastic zone of the standard SENB specimens is accounted for already by Eqns. 1.40 and 1.42 - 1.45). In the experiments the two different notch types were loaded at the applied stress ratio R = 0.1, each with two different applied stresses $\Delta\sigma_{appl}$. These conditions were simulated by using the Finite Element Method (FEM). It is assumed that the plastic zone is stabilized after 10 cycles. The resulting local stress ratio R as a function of the distance from the notch root is shown in Fig. 63.

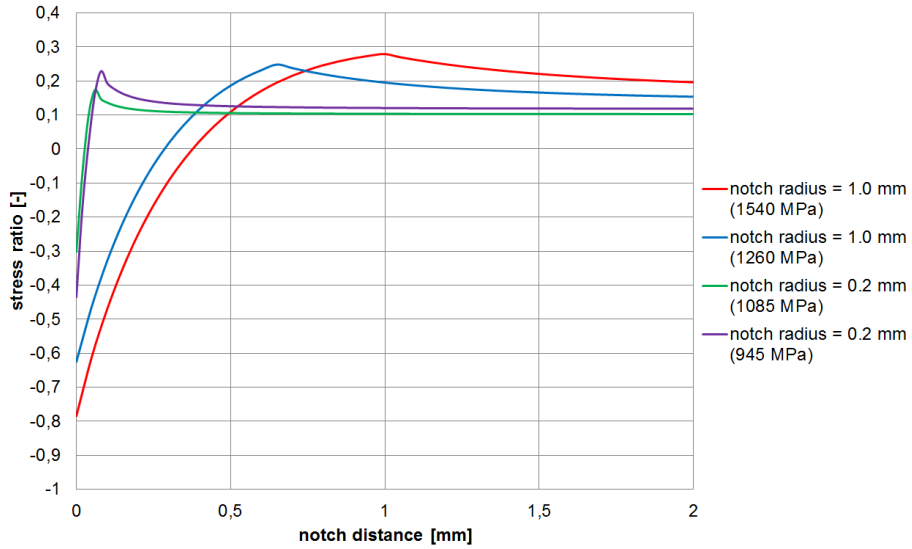

Fig. 63.: Local stress ratio in front of the notch for different geometries and notch stress levels for a global stress ratio R = 0.1

It can be observed that the plastic zone depends on the notch geometry as well as on the externally applied notch root stress range. The local stress ratio starts for all specimens at a negative value at the notch root and changes to a positive value after a certain distance. This varying stress ratio has to be considered when using Eq. 1.42 for calculating the crack growth.

5.3.4. Calculation of crack growth

In summary, the crack growth and the evaluation of the crack shape can be predicted with the modified NASGRO equation, the enhanced geometry factor in combination with the stress concentration in front of the notch and the varying local stress ratio.

To calculate the crack growth, a forward integration with a semi-elliptical starting crack shape and an initial crack length depending on the effective threshold $\Delta K_{\mathrm{th,eff}}$ is suggested. The initial crack length $\Delta a_{\mathrm{start}}$ is depending on the applied notch stress, the effective threshold and the crack shape.

$$\Delta a_{\mathrm{start}} = \left(\frac{\Delta K_{\mathrm{th,eff}}}{\Delta \sigma_{\mathrm{notch}} \cdot Y_{\mathrm{N}}(\Delta a)} \right)^2 \cdot \frac{1}{\pi} \qquad 5.7$$

This estimation assumes the lowest possible starting crack. This should be a good estimation for the smaller load amplitude, where the stress range $\Delta\sigma$ is near the endurance limit $\Delta\sigma_{\mathrm{e}}$.

As mentioned in chapter 4.2, the enhanced geometry function is valid up to c/B = 0.9. Assuming that the crack growth from c/B = 0.9 to c/B = 1.0 and the subsequent transformation into a straight crack front will take comparatively few cycles, this phase is approximated as follows: the geometry function is extrapolated up to c/B = 1.0; directly afterwards, the crack is assumed to exhibit a straight crack front. The geometry factor of a straight through-thickness crack can then be calculated by an existing solution from Tada [20].

In addition to the information of the crack shape and the specimen dimensions, the normalized potential drop $\Delta U/U_0$ can then be calculated by Eqns. 5.2 and 5.5 and converted into the fictitious straight through-thickness crack length computed from the DCPD measurements using the Johnson equation.

In Fig. 64 the crack growth of point A and the $\Delta a/c$ ratio (vertical right axis) is displayed as a function of the number of cycles for the case $\Delta a/c_{\mathrm{start}}$ = 0.6, t/W = 0.2, ρ/W = 0.05 and $\Delta\sigma_{\mathrm{notch}}$ = 1260 MPa. Additionally, the growth of a single semi-elliptical crack (black) is compared with that of a double semi-elliptical crack (blue). The full lines represent the calculated crack growth and the dotted lines the crack lengths as estimated from the DCPD measurements by Eqns. 5.2 - 5.4. Furthermore the growth of the semi-elliptical crack is compared with the resulting growth of a straight through-thickness crack (full red line).

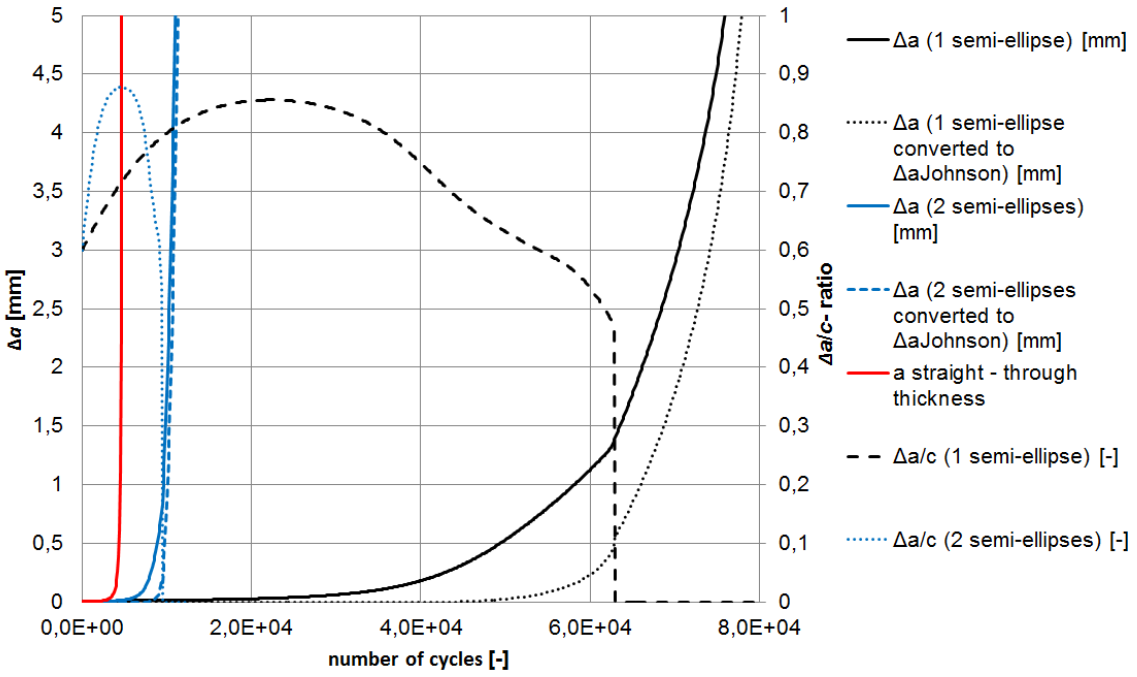

Fig. 64.: Crack growth and evolution of the $\Delta a/c$ ratio for single and double semi-elliptical cracks and corresponding fictitious crack lengths from the Johnson equation for a single and double semi-elliptical crack front and a straight through-thickness crack; for $\Delta a/c = 0.6$, $t/W = 0.2$, $\rho/W = 0.05$ and $\Delta\sigma_{notch} = 1260$ MPa.

Starting at $\Delta a/c = 0.6$, extracted from Fig. 56 a), the $\Delta a/c$ ratio increases rapidly nearly to 0.9 and then decreases due to the higher stress intensity factor at point C. At a crack length $\Delta a \sim 1.3$ mm, the crack width $2c$ reaches the specimen width and the crack is assumed to continue as a straight through-thickness crack.

Compared to the single ellipse, the crack growth of the double semi-elliptical crack is about 6 times faster and the transition point from the semi-elliptical shape to the straight crack front occurs at a crack length Δa of approximately 0.8 mm.

The straight crack grows much faster than the semi-elliptical crack due to a higher stress intensity factor at the crack tip. In comparison to the actual crack dimensions, the estimates from the DCPD measurements using the Johnson equation (dashed lines) underestimate the actual crack growth behavior in the early stage.

The differences in total lifetime depend markedly on the failure initiation site. Assuming that failure initiation occurs at a microstructural flaw of a certain size, this behavior can be modelled by assuming different initial crack lengths corresponding to different microstructural flaw sizes. In Fig. 65 the crack growth is exemplarily calculated for $\Delta a/c$ = 0.6, t/W = 0.2, ρ/W = 0.05 and $\Delta\sigma_{notch}$ = 1260 MPa and different initial crack lengths Δa_{start} from 10 µm up to 100 µm.

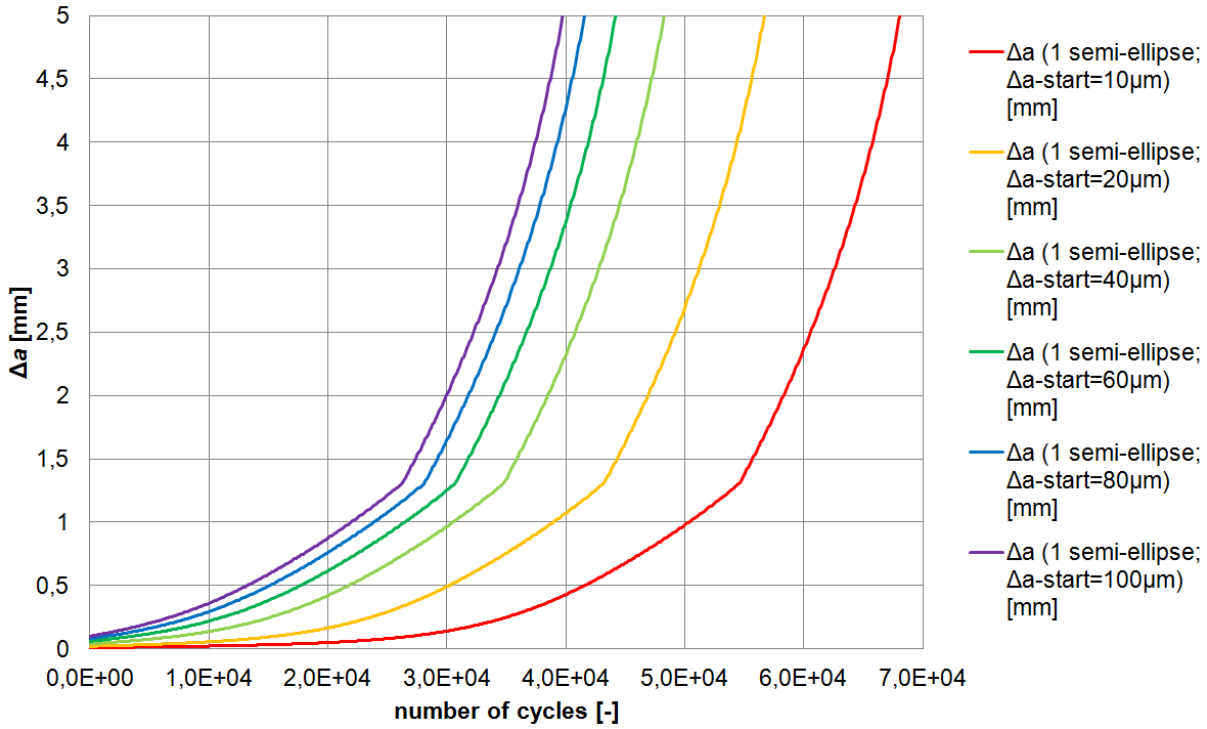

Fig. 65.: Comparison of the crack growth behavior for different initial crack sizes $10 \leq \Delta a_{start} \leq 100$ µm exemplary shown for $\Delta a/c$ = 0.6, t/W = 0.2, ρ/W = 0.05 and $\Delta\sigma_{notch}$ = 1260 MPa and assuming a single semi-elliptical crack front.

The crack growth curves show clearly that the lifetime can be about two times higher if the initial flaw is about 10 times smaller. This explains well the scatter in the curves from Fig. 55.

Starting from a given initial crack length and shape, the crack growth is calculated for different notch geometries and various applied stresses and displayed in Fig. 66. The colored lines represent the experimental data from the DCPD measurements and the Johnson equation (cf. Fig. 55); the black dashed and dotted lines describe the growth of a single and a double semi-elliptical shape, resp. converted to the length of a fictitious straight through-thickness crack equal to the Johnson approach. Due to the fact that the number of cycles at initiation depends on the microstructural flaw size, the experimentally determined crack growth curves where shifted such that they result in the same number of cycles at failure.

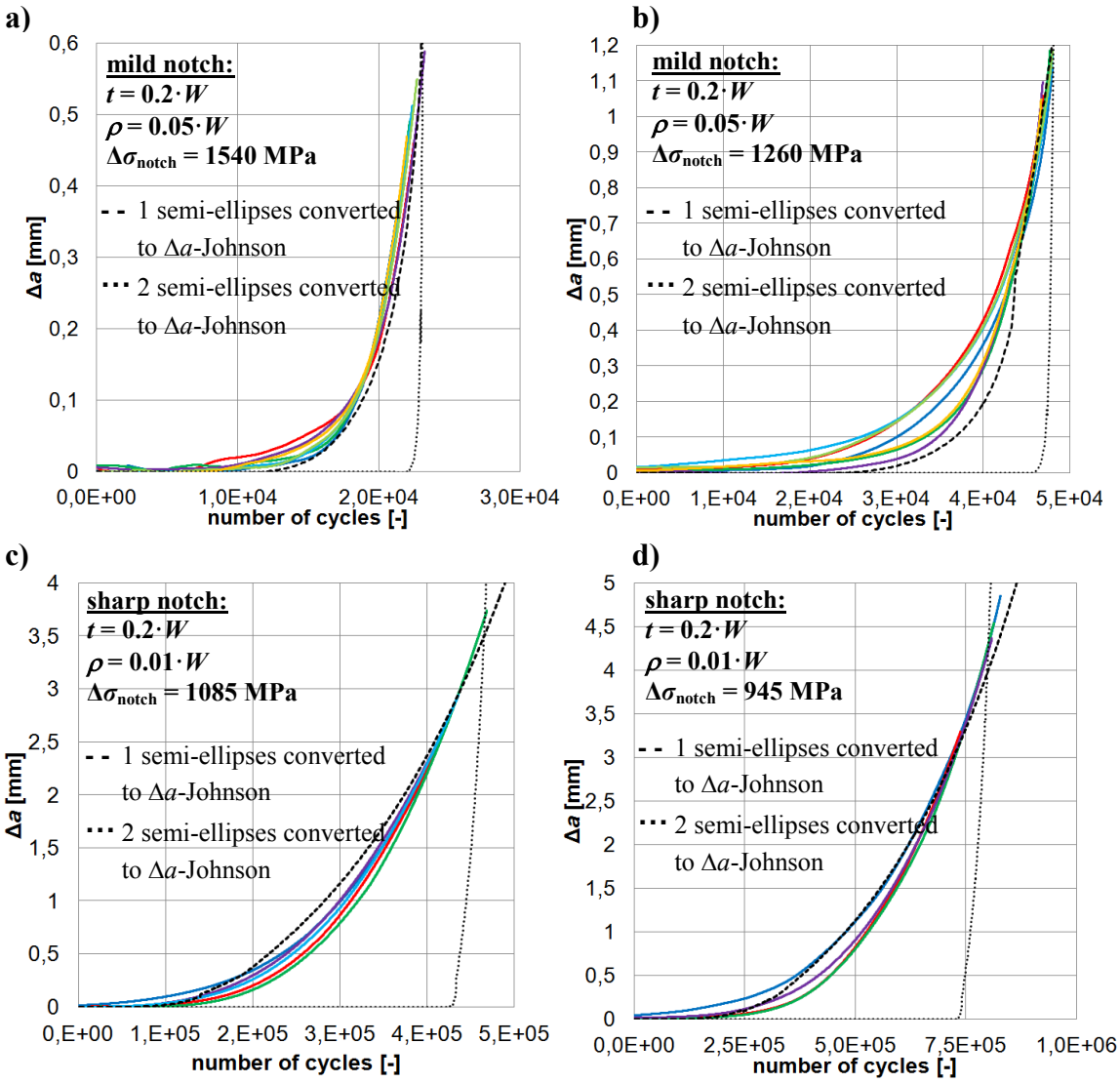

Fig. 66.: Crack growth curves (full lines: experiment, dashed lines: single semi-elliptical crack, dotted lines: double semi-elliptical crack): (a) $\rho = 0.05 \cdot W$, $t = 0.2 \cdot W$ and $\Delta\sigma_{notch} = 1540$ MPa; (b) $\rho = 0.05 \cdot W$, $t = 0.2 \cdot W$ and $\Delta\sigma_{notch} = 1260$ MPa; (c) $\rho = 0.01 \cdot W$, $t = 0.2 \cdot W$ and $\Delta\sigma_{notch} = 1085$ MPa; (d) $\rho = 0.01 \cdot W$, $t = 0.2 \cdot W$ and $\Delta\sigma_{notch} = 945$ MPa;

The prediction with a single semi-elliptical crack growth fits acceptably to the experimentally determined crack growth curves, whereas the double semi-elliptical crack overestimates the crack growth. The remaining differences between the predicted and the measured crack growth are quite small and may be explained by deviations from the idealized semi-elliptical shape and a possible initiation of several cracks with different shapes.

This study clearly indicates that the number of cycles for crack initiation of a previously damaged component is very small compared to the number of cycles at failure. A significant portion of the life time is attributable to the crack initiation, as those may be assumed from a first examination of these experiments, is required for crack propagation from few 10 µm to few 100 µm.

6. Summary and Conclusions

In this thesis, different methods for the evaluation of high strength materials in railway switch components, especially switch blades, have been presented. The analysis distinguishes between a static failure during the manufacturing process and dynamic failure during the in-service application in the track.

During manufacturing, the bending process of the rail curvature leads to high strains at the outer fiber of the rail. Considering small flaws in rails, the failure strain of tensile experiments cannot be used as a design criterion anymore. Therefore, different options using the R6 method are available in standards. Nevertheless, a direct connection between the failure criterion and manufacturing loads are difficult in engineering approaches. For this case, a static strain based Kitagawa-Takahashi diagram is introduced to describe the nominal failure strain in the outer fiber depending on the crack length.

For long cracks, the fracture toughness K_{IC} is used as strength limit. Considering small cracks the J-integral is used as a crack driving force and the failure strain is estimated in combination with the strain energy density. For an accurate prediction, depending on the hardening behavior, the Q-stress has to be used to describe the in-plane constraint effect for very short cracks.

Hence, the important material parameter for the manufacturing process is not the fracture strain in tension but the fracture toughness.

Afterwards, using the strain energy density, the calculation of the J-integral was tested by using a single edge-notched tension specimen. This is done by comparing an analytical estimation of the J-integral based on the strain energy density with the line integral calculated from finite element simulations for materials with different hardening exponents and additionally for an ideal plastic material behavior.

For positive hardening exponents and short crack lengths, the analytical solution for the J-integral based on the strain energy density corresponds perfectly with the line integral and confirms the correct estimation of the failure strain in the bending experiments. However, for an ideal plastic material, the J-integral is infinity, which is due to the plastic correction factor.

For cyclic loading in service, two different approaches are compared. In the stress based design approach, the Haigh or the commonly used Smith diagram is used to describe the endurable stress range, depending on the mean stress. Here, the endurable stress is denoted by the material strength, estimated from tensile experiments. Notches or surface conditions reduce the endurance limit which is accounted for by correction factors.

It was shown that a good correlation between the fatigue experiments and the estimated endurance limit can be determined. In the stress based approach, high strength materials exhibit a higher endurance limit.

In consideration of cracks, the Kitagawa-Takahashi diagram is used to calculate the endurable stress range depending on the crack length. For long cracks, the long crack threshold is used as a limiting factor, for physically short cracks the cyclic crack resistance curve caused by different closure mechanisms has to be considered. Different stress ratios are presented by separate slopes. Again, the predicted curves correlate in an acceptable range with the experiments. Considering higher stress ratios R, the limiting curves are almost similar for long cracks.

Moreover, it has been shown, that the design curves of the endurance stress limit of the Kitagawa-Takahashi diagram can be transferred into the Smith diagram, where each crack length will correspond to an endurable stress curve.

Crack growth calculations in the linear elastic fracture mechanics (LEFM), estimated by finite element (FE) simulations, beyond the long crack threshold has been presented schematically and their disadvantages have been discussed. In addition providing a more appropriate solution, a new enhanced geometry function has been presented for the analytical calculation of the crack growth of a semi-elliptical crack for a/W and c/B ratios close to 1. Additionally, solutions for bending around the x-axis, where the crack tip crosses the neutral bending axis, as well as for bending around the y-axis have been provided in order to describe all possible loadings in Mode I occurring in the structural stress concept.

The derived equations are valid for the range $0.2 \leqslant a/c \leqslant 1.0$, $0.01 \leqslant a/W \leqslant 0.9$, $0.01 \leqslant c/B \leqslant 0.9$ with an error of typically less than $\pm 10\%$. These new approximate equations for the geometry factor are expected to allow an acceptable estimate of the crack tip loading even if the crack depth and width are close to the specimen thickness and width, respectively.

Finally, the influence of the stress concentration of a notch on the crack growth behavior has been investigated. For this case, fatigue experiments with two different notch geometries at two different applied stress ranges have been evaluated. It was shown that the crack starts with a semi-elliptical shape. Hence, the commonly used DCPD method with the Johnson

equation underestimates the real crack length. Therefore, a new method has been presented to estimate the crack length by considering the potential change, the crack shape and existing boundaries.

The experimental results of the crack length development as a function of the number cycles have then been compared with the analytical calculation of the crack growth using the modified NASGRO equation, the varying stress ratio and crack shape. The improved analytical calculation method correlates acceptably well to the experimental data. The higher the stress ratio, the earlier the transition from the semi-elliptical to the straight crack front occurs. It has been shown that the number of cycles at crack initiation highly depends on the size of the individual microstructural flaw and that the crack growth period dominates the total lifetime.

Concluding it can be said, that for a correct prediction of the lifetime of a switch rail, a suitable design concept has to be chosen as it highly depends on several factors such as flaw size, the loading (cyclic, static) and also of the material behavior itself. It is shown that for an accurate prediction it is necessary to create new or modify existing design concepts, as has was successfully been demonstrated in the present thesis.

7. Nomenclature

Roman alphabet

a	crack length [mm]
a_0	initial crack length [mm]
$a_{0,H}$	intrinsic crack length by El Haddad [mm]
$a^{(e)}$	size of the finite element [mm]
a_f	crack length at fracture [mm]
a_m	material constant for the mean stress sensitivity [-]
a_{pl}	transition point between LEFM and EPFM [mm]
Δa	crack extension [mm]
$\Delta a_{experiment}$	crack length from the fracture surface [mm]
Δa_{start}	initial crack length [mm]
$\Delta a_{Johnson}$	crack extension of a straight crack front as calculated by the Johnson formula [mm]
$\Delta a_{semi\text{-}ellipse}$	crack extension of a semi-elliptical crack front [mm]
$\Delta a_{straight}$	crack extension of a straight crack front [mm]
A_0	constant in Newman's crack opening function [-]
A_1	constant in Newman's crack opening function [-]
A_2	constant in Newman's crack opening function [-]
A_3	constant in Newman's crack opening function [-]
b	length of the ligament [mm]
b_m	material constant for the mean stress sensitivity [-]
B	thickness of the specimen [mm]
c	half of the crack width (major semi-axis of the semi-elliptical crack) [mm]
$c_{elliptical}$	crack width of a semi-elliptical crack [mm]
C	material constant describing the Paris slope in the NASGRO equation [-]
$C_1 \dots C_7$	constants to describe the potential drop depending on the crack geometry and specimen [-]
D	material constant to calculate the Q-stress depending on the crack length [-]

D_r	parameter in the failure assessment diagram [-]
e_x	distance between outer fiber and neutral x-axis [mm]
e_y	distance between outer fiber and neutral y-axis [mm]
E	Young's modulus [MPa]
D	damage in the Miner rule [-]
D_i	damage in the Miner rule of cycles each load cycle [-]
$f(a/W)$	geometry function [-]
$f(L_r)$	function to describe K_r in the FAD [-]
$f(n)$	plastic correction function of the J-integral beyond the yield strength [-]
$f(R,\Delta a)$	Newman's crack opening function [-]
f_e	endurance limiting constant [-]
$F(R,\Delta a)$	crack velocity factor in the NASGRO equation [-]
F_{max}	maximum applied force at failure [N]
F_z	tension force [N]
h	material constant to calculate the critical J-integral depending on the Q-stress [-]
H	height of the specimen [mm]
I_n	material constant of the HRR field [-]
I_x	axial moment of inertia around the x-axis [mm^4]
I_y	axial moment of inertia around the y-axis [mm^4]
J	J-integral [kN/m]
$J(w)$	J-integral denoted by strain energy density [kN/m]
J_c	critical J-integral [kN/m]
J_{el}	elastic part of the J-integral [kN/m]
J_{mat}	material dependent J-integral [kN/m]
J_{pl}	plastic part of the J-integral [kN/m]
J_Γ	J-integral denoted by the line integral [kN/m]
k	material constant for the Q-stress depending on the crack length [-]
k_f	gradient of the slope for the fatigue strength [-]

K	stress intensity factor [MPa√m]
K_I	stress intensity factor in fracture mode I [MPa√m]
K_{Ic}	fracture toughness [MPa√m]
$K_m(R)$	mean stress sensitivity factor [-]
K_{mat}	material dependent fracture toughness [MPa√m]
K_r	parameter in the failure assessment diagram [-]
$K_{surface}$	reduction factor due to surface condition [-]
ΔK	stress intensity factor range [MPa√m]
ΔK_{FEM}	stress intensity range from FE simulations [MPa√m]
ΔK_{th}	threshold value of the stress intensity factor range [MPa√m]
$\Delta K_{th,eff}$	intrinsic (effective) threshold value of the stress intensity factor range [MPa√m]
$\Delta K_{th,lc}$	long crack threshold value of the stress intensity factor range [MPa√m]
l_i	length scale for the build-up of crack closure [mm]
L	specimen length [mm]
L_r	parameter in the failure assessment diagram [-]
m	material constant describing the Paris slope in the NASGRO equation [-]
M_x	bending moment around x-axis [Nmm]
M_y	bending moment around y-axis [Nmm]
M_σ	mean stress sensitivity [-]
n	hardening exponent of the Ramberg-Osgood hardening equation [-]
n_{pl}	plastic support factor for static loading [-]
n_σ	elastic support factor for cyclic loading [-]
N	total number of cycles [-]
N_e	number of cycles at the intersection of the endurance limit and fatigue strength [-]
N_i	number of cycles each load block [-]
ΔN	number of cycles between crack initiation and failure [-]
N_f	number of cycles at failure [-]

p	material constant describing the transition from near threshold to Paris slope [-]
q	variable for the initial crack length [-]
Q	Q-stress [MPa]
r	distance from the crack tip [mm]
R	stress ratio [-]
s	distance between the load line and the support [mm]
t	notch depth [mm]
T_i	component of the traction vector [MPa]
U_0	initial electric potential drop [V]
ΔU	electric potential drop [V]
v	deflection [mm]
w	strain energy density [MPa]
w_{el}	elastic part of the strain energy density [MPa]
$w_{el}(\varepsilon_0)$	elastic part of the strain energy density at yield point [MPa]
w_{pl}	plastic part of the strain energy density [MPa]
W	specimen height [MPa]
x	characterization variable for $0.5 < c/B < 1.0$ enhancement [-]
Y	geometry factor [-]
$Y(a/W)$	geometry function [-]
$Y(a/c,a/W,c/B)$	geometry factor, analytical approximation [-]
$Y_{A,C\text{-}a/W\text{-}Fz}$	geometry factor for point A or C and pure tension, enhanced for $0.5 < a/W \leq 0.9$ [-]
$Y_{A,C\text{-}a/W\text{-}Mx}$	geometry factor for point A or C and bending around the x-axis, enhanced for $0.5 < a/W \leq 0.9$ [-]
$Y_{A,C\text{-}c/B\text{-}Fz}$	geometry factor point A or C and pure tension, enhanced for $0.5 < c/B < 1.0$ [-]
$Y_{A,C\text{-}c/B\text{-}Mx}$	geometry factor point A or C and bending around the x-axis, enhanced for $0.5 < c/B < 1.0$ [-]
$Y_{A,C\text{-}Fz}(a/W = 0.9)$	geometry factor for point A or C and pure tension for the ratio $a/W = 0.9$, determined from the FE simulations [-]

$Y_{A,C\text{-}Fz}(c/B = 0.9)$	geometry factor for point A or C and pure tension for the ratio $c/B = 0.9$, determined from the FE simulations [-]
$Y_{A,C\text{-}lin\text{-}a/W\text{-}Fz}$	linear approximation for point A or C and pure tension between NR and $a/W = 0.9$, enhanced for $0.5 < a/W \leq 0.9$ [-]
$Y_{A,C\text{-}lin\text{-}a/W\text{-}Mx}$	linear approximation for point A or C and bending around the x-axis between NR and $a/W = 0.9$, enhanced for $0.5 < a/W \leq 0.9$ [-]
$Y_{A,C\text{-}lin\text{-}c/B\text{-}Fz}$	linear approximation for point A or C and pure tension between NR and $c/B = 0.9$, enhanced for $0.5 < c/B < 1.0$ [-]
$Y_{A,C\text{-}lin\text{-}c/B\text{-}Mx}$	linear combination for point A or C and bending around the x-axis between NR and $c/B = 0.9$, enhanced for $0.5 < c/B < 1.0$ [-]
$Y_{A,C\text{-}Mx}(a/W = 0.9)$	geometry factor for point A or C and bending around the x-axis for the ratio $a/W = 0.9$, determined from the FE simulations [-]
$Y_{A,C\text{-}Mx}(c/B = 0.9)$	geometry factor for point A or C and bending around the x-axis for the ratio $c/B = 0.9$, determined from the FE simulations [-]
$Y_{A,C\text{-}NR\text{-}Fz}$	geometry factor by Newman and Raju for pure tension [-]
$Y_{A,C\text{-}NR\text{-}Mx}$	geometry factor by Newman and Raju for bending around x- axis [-]
$Y_{FE}(a/c,a/W,c/B)$	geometry factor extracted from FE simulations [-]
$Y_N(\Delta a)$	geometry factor for a crack emanating from a notch [-]
$Y_{straight}$	geometry factor for a straight (through-thickness) crack front by Tada [-]
$\Delta Y_{A,C\text{ -}a/W\text{-}Fz}$	alternative geometry factor for point A or C and pure tension, varying around the linear combination between the boundaries, enhanced for $0.5 < a/W \leq 0.9$ [-]
$\Delta Y_{A,C\text{ -}a/W\text{-}Mx}$	alternative geometry factor for point A or C and bending around the x-axis, varying around the linear combination between the boundaries, enhanced for $0.5 < a/W \leq 0.9$ [-]
$\Delta Y_{A,C\text{-}c/B\text{-}Fz}$	alternative geometry factor for point A or C and pure tension, varying around the linear combination between the boundaries, enhanced for $0.5 < c/B < 1.0$ [-]
$\Delta Y_{A,C\text{-}c/B\text{-}Mx}$	alternative geometry factor for point A or C and bending around the x-axis, varying around the linear combination between the boundaries, enhanced for $0.5 < c/B < 1.0$ [-]
z	characterization variable for $0.5 < a/W < 0.9$ enhancement [-]

Greek alphabet

α	material constant of the Ramberg-Osgood hardening equation [-]
α_k	elastic stress concentration factor at the notch root [-]
α_N	Newman's plane stress / plane strain tuning factor [-]
β	material constant to calculate the dependency of the Q-stress [-]
ε	total strain [-]
ε_{el}	elastic strain until yield point [-]
ε_f	failure strain [-]
$\varepsilon_{f,exp}$	failure strain from tensile experiments [-]
$\varepsilon_{f\text{-}EPFM}$	failure strain in elastic-plastic fracture mechanics [-]
$\varepsilon_{f\text{-}LEFM}$	nominal failure strain in linear-elastic fracture mechanics [-]
ε_{pl}	plastic strain beyond yield point [-]
ε_{ref}	nominal applied strain at rupture [-]
ε_{ys}	elastic strain until yield point [-]
ε_0	strain at the yield stress in the Ramberg-Osgood hardening equation [-]
Γ	path around the crack tip of the line integral [mm]
η	material constant to calculate the critical *J*-integral depending on the *Q*-stress [-]
ν	Poisson ratio [-]
ν_t	material constant for the cyclic crack resistance curve [-]
ρ	notch radius [mm]
σ	total stress [MPa]
σ_0	yield stress in the Ramberg-Osgood hardening equation [MPa]
σ_a	stress amplitude [MPa]
$\sigma_{a,i}$	stress amplitude of each load block [MPa]
σ_{appl}	applied stress amplitude [MPa]
$\sigma_{bending\text{-}x\text{-}x}$	stress due to bending around the x-axis [MPa]
$\sigma_{bending\text{-}y\text{-}y}$	stress due to bending around the y-axis [MPa]

$\sigma_{e,0}$	endurance stress for tension/compression loading [MPa]
$\sigma_{e,bending}$	endurance limit for polished specimen under bending [MPa]
$\sigma_{e,bending,skin}$	endurance limit considering the surface of the rolling skin under bending [MPa]
σ_{el}	nominal elastic stress until yielding point [MPa]
$\sigma_{F,0}$	flow stress for tension/compression loading [MPa]
σ_{ij}	stress tensor of the HRR field [MPa]
$\widetilde{\sigma}_{ij}$	tabulated material parameter for calculation of the HRR field [-]
σ_m	mean stress [MPa]
σ_{max}	maximum applied stress [MPa]
σ_{min}	minimum applied stress [MPa]
σ_{ref}	nominal applied stress at failure [MPa]
$\sigma_{tension}$	stress due to tension load [MPa]
σ_{unit}	stress due to the applied unit load [MPa]
σ_{UTS}	ultimate tensile strength [MPa]
σ_{ys}	yield stress [MPa]
$\sigma_{\theta\theta,FEM}$	stress in tangential direction obtained from the numerical simulation [MPa]
$\sigma_{\theta\theta,HRR}$	stress in tangential direction obtained from the HRR field [MPa]
$\Delta\sigma$	stress range [MPa]
$\Delta\sigma_e$	endurable stress range [MPa]
$\Delta\sigma_{notch}$	stress range acting in front of the notch [MPa]
θ	angle for the position of the stress element in the HRR field [°]

8. List of Figures

9. References

[1] Kolitsch, S., Gänser, HP., Pippan, R. 2017. Damage Tolerant Concepts for Railway Switch Components. ESIS TC24 Workshop. Integrity of Railway structures.

[2] Kolitsch, S., Gänser, HP., Pippan, R. 2016. Fatigue crack growth threshold as a design criterion – statistical scatter and load ratio in the Kitagawa-Takahashi diagram. IOP Conference Series: Materials Science and Engineering 119.

[3] Kolitsch, S., Gänser, HP., Pippan, R.. Dependence of Fracture Strain on Flaw Size – Experiments and Theoretical Modelling. Engineering Failure Analysis. submitted 04/2017.

[4] Kolitsch, S., Pippan, R.. Experimental determination of the J-integral for hardening and softening materials in a single edge notch tension (SENT) specimen - limits and recommendations. in progress

[5] Kolitsch, S., Gänser, HP., Pippan, R.. Approximate stress intensity factor solutions for semi-elliptical cracks with large a/W and c/B under tension and bending. Theoretical and Applied Fracture Mechanics. Available online 06/2017.

[6] Kolitsch, S., Gänser, HP., Pippan, R. 2016. Determination of crack initiation and crack growth stress-life curves by fracture mechanics experiments and statistical analysis. 21st European Conference on Fracture. Structural Integrity Procedia Volume 2, 3026-3039.

[7] Kolitsch, S., Gänser, HP., Pippan, R.. Experimental and calculation challenges of crack propagation in notches - from initiation to end of lifetime. International Journal of Fatigue, Vol. 103, pp. 395-404.

[8] Haibach, E. 2006. Betriebsfestigkeit: Verfahren und Daten zur Bauteilberechnung. 3rd Edition., Springer.

[9] Radaj, D., Vormwald, M. 2010. Ermüdungsfestigkeit: Grundlagen für Ingenieure, 3. Auflage, Springer.

[10] Haigh, B. P. 1915. Report on alternating stress tests of a sample of mild steel. British Association Stress Committee, Manchester. BASC-Rep. No.85, pp. 163-170.

[11] Gerber, H. 1874. Bestimmung der zulässigen Spannungen in Eisenkonstruktionen. Z. d. Bayer. Architekten- u. lngenieursverein 6, pp. 101-110

[12] Goodman, J. 1954. Mechanics Applied to Engineering. Longmans, Green & Co, New York 1899; Volume 9.

[13] Soderberg, C. R. 1930. Factor of safety and working stress. J. Appl. Mech. (ASME) 52.

[14] Forschungskuratorium Maschinenbau (FKM) 2012. Rechnerischer Festigkeitsnachweis für Maschinenbauteile (Proof of strength for mechanical engineering components). 6th Ed., VDMA 2012.

[15] Smith, J. H. 1910. Some experiments on fatigue of metals. J. Iron and Steel Institute 82, pp. 246-318

[16] Palmgren, A. 1924. Die Lebensdauer von Kugellagern. VDI-Z 58, pp. 339-341.

[17] Miner,M.A. 1945. Cumulative damage in fatigue. J.Appl.Mech. 12, pp. 159-164.

[18] Haibach, E. 1970. Modifizierte lineare Schadensakkumulations-Hypothese zur Berücksichtigung des Dauerfestigkeitsabfalls mit fortschreitender Schädigung. LBF-Technische Mitteilung TM 50/70.

[19] Anderson, T.L. 2005. Fracture Mechanics – Fundamentals and Applications. Third edition.

[20] Murakami Y. 1997. Stress intensity factors and weight functions. Southampton UK and Boston USA: Computational Mechanics Publications.

[21] Rice, J.R. 1968. A Path Independent Integral and the Approximate Analysis of Strain Concentration by Notches and Cracks. Journal of Applied Mechanics, Vol. 35, pp. 379-386.

[22] Hutchinson, J.W. 1968. Singular Behavior at the End of a Tensile Crack Tip in a Hardening Material. Journal of the Mechanics and Physics of Solids, Vol. 16, pp. 13–31.

[23] Rice, J.R. and Rosengren, G.F. 1968. Plane Strain Deformation near a Crack Tip in a Power-Law Hardening Material. Journal of the Mechanics and Physics of Solids, Vol. 16, pp. 1–12.

[24] Shih C. F. 1983. Tables of Hutchinson-Rice-Rosengren singular field quantities. Materials Research Laboratory, Brown University.

[25] Barsom, J.M. and Rolfe, S.T. 1987. Fracture and Fatigue Control in Structures. 2nd Ed., Prentice-Hall, Englewood Cliffs.

[26] Williams, M.L. 1957. On the Stress Distribution at the Base of a Stationary Crack. Journal of Applied Mechanics, Vol. 24, pp. 109–114.

[27] Kirk, M.T., Koppenhoefer, K.C., and Shih, C.F. 1993. Effect of Constraint on Specimen Dimensions Needed to Obtain Structurally Relevant Toughness Measures. ASTM STP 1171, pp. 79–103.

[28] Shih, C.F., O'Dowd, N.P., and Kirk, M.T. 1993. A Framework for Quantifying Crack Tip Constraint. ASTM STP 1171, pp. 2–20.

[29] O'Dowd, N.P. and Shih, C.F. 1991. Family of crack-tip fields characterized by a triaxiality parameter – I. structure of fields. Journal of the Mechanics and Physics of Solids, Vol. 39, pp. 898–1015.

[30] O'Dowd, N.P. and Shih, C.F. 1991. Family of crack tip fields characterization by a triaxial parameter, II. Fracture Applications. J. Mech. Phys. Solids, Vol 40, pp. 939-969.

[31] E 399-90, 1990. Standard Test Method for Plane-Strain Fracture Toughness of Metallic Materials.” American Society for Testing and Materials, Philadelphia.

[32] E1820-01, 2001. Standard Test Method for Measurement of Fracture Toughness". American Society for Testing and Materials; Philadelphia.

[33] BS 7448, 1991. Fracture Mechanics Toughness Tests, Part1, Method for Determination of KIC, Critical CTOD and Critical J Values of Metallic Materials." British Standard Institution, London.

[34] Shih, C.F. and Hutchinson, C.W. 1975. Fully Plastic Solutions and Large Scale Yielding Estimates for Plane Stress Crack Problems. Report No. DEAP-S-14, Division of Engineering and Applied Physics, Harvard University, Cambridge Mass.

[35] Dowling, N.E. 1977. Crack Growth During Low-Cycle Fatigue of Smooth Axial Specimens, Cyclic Stress-Strain and Plastic Deformation Aspects of Fatigue Crack Growth. ASTM STP 637, American Society for Testing and Materials, pp. 97-121

[36] R6 Revision 4, 2011. Assessment of the integrity of structures containing defects. British Energy, Gloucester.

[37] SINTAP, 1999. Structural Integrity Assessment Procedures for European Industry—Final Procedure, European Union Project No. BE95-1426.

[38] FITNET, 2008. Fitness-For-Service Procedure. Revision MK 8.

[39] Betegon, C, and Hancock, J. 1991. Characterization biparametrica de los campos tensionales en la mecanica de la fractura elastoplastica. Ph.D. Thesis, Deperatment of Construction, University of Ovied.

[40] Betegon, C, and Hancock, J. 1991. Two-Parameter Characterisation of Elastic-Plastic Crack-Tip Fields. ASME Journal of Applied Mechanics, Vol. 58, pp. 104-113.

[41] Ainsworth R.A. 1995. A constraint-based failure assessment diagram for fracture assessment. International Journal of Pressure Vessels and Piping, Vol. 64, pp. 277-285.

[42] MacLennan, I. and Hancock J.W. 1995. Constraint-based failure assessment diagrams. International Journal of Pressure Vessels and Piping, Vol. 64, pp. 287-298..

[43] Budden, P.J. and Ainsworth, R.A. 2012. The shape of a strain based failure assessment diagram. International Journal of Pressure Vessels and Piping, Vol. 89, pp. 59-66.

[44] Budden, P.J. 2006. Failure assessment diagram methods for strain based fracture. Engineering Fracture mechanics, Vol. 73, pp. 537-552.

[45] Paris P.C., Gomez M.P., Anderson W.P. 1961. A rational analytic theory of fatigue. The Trend in Engineering Vol. 13, pp. 9-14

[46] Paris P.C., Erdogan F. 1963. A critical analysis of crack propagation laws. Journal of Basic Engineering Vol. 85, pp. 528-534

[47] Rice, J.R. 1967. Mechanics of crack tip deformation and extension by fatigue. In Fatigue Crack Propagation, Special Technical Publication 415. American Society for Testing and Materials, pp. 247-309.

[48] Kitagawa, H., Takahashi, S. 1976. Applicability of fracture mechanics to very small cracks or cracks in the early stage. Proceeding of the second international conference on mechanical behavior of materials ASM, pp. 627-631.

[49] El Haddad, MH., Topper, TH., Smith KN. 1973. Prediction of non-propagating cracks. Engineering Fracture Mechanics 11, 573-584.

[50] Tabernig, B. and Pippan, R. 2002. Determination of the length dependence of the threshold for fatigue crack propagation. Eng. Fracture Mech. 69, 899-907.

[51] Maierhofer, J., Pippan, R., Gänser, HP. 2014. Modified NASGRO equation for physically short cracks. International Journal of Fatigue 59, 200-207.

[52] Tanaka, K. and Akinawa, Y. 2003. Modelling of fatigue crack growth: mechanistic models. In: Ritchie, R.O. and Murakami, Y. (eds.): Comprehensive Structural Integrity; Volume 4: Cyclic loading and Fracture; Elsevier, 165–89.

[53] Suresh, S. 2012. Fatigue of materials. Cambridge: Cambridge University Press, 2nd. ed.

[54] Pippan, R. and Hohenwarter, A. 2017: Fatigue crack closure: a review of the physical phenomena. Fatigue Fract Engng Mater Struct, 1-25.

[55] Maierhofer J, Gänser HP, Pippan R. 2015. Modified Kitagawa-Takahashi diagram accounting for finite notch depths. Int J Fat 70, p. 503-509.

[56] Bruchmechanischer Festigkeitsnachweis für Maschinenbauteile (FKM), 2009. Fracture mechanics proof of strength for mechanical engineering components. 3. Ausgabe.

[57] Paris P.C., Erdogan F. 196. A critical analysis of crack propagation laws. Journal of Basic Engineering 85, pp. 528-534

[58] Paris PC, Gomez MP, Anderson WP. 1961. A rational analytic theory of fatigue. The Trend in Engineering 13, pp. 9-14

[59] Pippan, R. 1987. The growth of short cracks under cyclic compression. Fract. Engng. Mat. Struct. 9, pp. 319-328.

[60] Johnson H.H. 1965. Calibrating the electric potential method for studying slow crack growth. Material Research Standards 5.

[61] Schwalbe K.H., Hellman D. 1981. Application of the electrical potential method to crack length measurements using Johnson's formula. Journal of Testing and Evaluation 9.

[62] ASTM E1820-15a. Standard Test Method for Measurement of Fracture Toughness

[63] Brocks W., Schneider I. 2001.Numerical Aspects of the Path-Dependence of the J-integral in Incremental Plasticity. Technical Note GKSS/WMS/01/08.

[64] Kunar M. 2008. Numerische Beanspruchungsanalyse von Rissen. 1. Auflage

[65] Brown, W.F., Jr. and Srawley, J.E. 1966. Plane Strain Crack Toughness Testing of High Strength Metallic Materials. ASTM STP 410, American Society for Testing and Materials, Philadelphia.

[66] Nisitani, H., Murakami Y. 1974. Stress intensity factors of an elliptical crack or a semi-elliptical crack subject to tension, International Journal of Fracture 10, 353–368.

[67] Newman, JC., Raju, IS. 1977. Improved stress-intensity factors for semi-elliptical cracks in finite-thickness plates. NASA Report TM-X-72825.

[68] Newman, JC., Raju, IS. 1979. Analysis of surface cracks in finite plates under tension or bending loads. NASA Report TP-1578.

[69] Newman, JC., Raju, IS. 1981. An Empirical Stress-Intensity Factor Equation for Surface Crack. Engineering Fracture Mechanics 15, 185-192.

[70] Newman J.C., Reuter W.G., Aveline C.R. 1999. Stress and fracture analyses of semi-elliptical surface cracks, ASTM Special Technical Publication 1360, pp. 403-423.

[71] Isida M., Noguchi H., Yoshida T. 1984. Tension and bending of finite thickness plates with a semi-elliptical surface crack, International Journal of Fracture 26, pp. 157-188.

[72] Fett T. 1991. Stress intensity factors for semi-elliptical surface cracks in a plate under tension based on the Isida's solution, International Journal of Fracture 48, pp. 139-151.

[73] Wang X., Lambert S.B. 1997. Stress intensity factors and weight functions for high aspect ratio semi-elliptical surface cracks in finite-thickness plates, Engineering Fracture Mechanics 57/1, pp. 13-24.

[74] Shiratori M., Niyoshi T., Tanikawa K. 1987. Analysis of stress intensity factors surface cracks subjected to arbitrarily distributed surface stresses. Stress Intensity Factors Handbook Vol. 2, ed. Y. Murakami, pp. 698-705.

[75] Vainshtok, V.A., Varfolomeyev I. V. 1989. Stress intensity factor equations for part-elliptical cracks and their verification, Engineering Fracture Mechanics 34/1, 125-136

[76] Strobl S, Supancic P, Lube T, Danzer R. 2012. Surface crack in tension or in bending – A reassessment of the Newman and Raju formula in respect to fracture toughness measurements in brittle materials. Journal of the European Ceramic Society 32, pp. 1491-1501

[77] Carpinteri A., Brighenti, R., Vantadori, S., 2003. Circumferentially notched pipe with an external surface crack under complex loading, International Journal of Mechanical Sciences 45/12, 1929-1947.

[78] Shin, C.S., Cai, C.Q. 2004. Experimental and finite element analyses on stress intensity factors of an elliptical surface crack in a circular shaft under tension and bending, International Journal of Fracture 129/3, 239-264.

[79] Carpinteri, A., Brighenti, R., Vantadori, S. 2006. Notched shells with surface cracks under complex loading, International Journal of Mechanical Sciences 48/6, 638-649.

[80] Carpinteri, A., Vantadori, S. 2009. Sickle-shaped surface crack in a notched round bar under cyclic tension and bending, Fatigue and Fracture of Engineering Materials and Structures 32/3, 223-232.

[81] Carpinteri, A., Brighenti, R., Huth, H.J., Vantadori, S. 2005. Fatigue growth of a surface crack in a welded T-joint, International Journal of Fatigue 27/1, 59-69.

[82] Carpinteri, A., Ronchei, C., Scorza D., Vantadori S. 2015. Fracture mechanics based approach to fatigue analysis of welded joints, Engineering Failure Analysis 49, 67-78.

[83] Vantadori S., Carpinteri A., Scorza D. 2013. Simplified analysis of fracture behavior of a Francis hydraulic turbine runner blade, Fatigue and Fracture of Engineering Materials and Structures 36/7, 679-688.

[84] Varfolomeev I., M. Busch, Petersilge M. 1998. Characterization of the computational accuracy in surface crack problems. International Journal of Numerical Methods in Engineering 41, 721-738.

[85] Marques de Sá JP., 2007. Applied Statistics, Using SPSS, STATISTICA, MATLAB and R. Springer-Verlag.

[86] Tanaka K. 2014. Crack initiation and propagation in torsional fatigue of circumferentially notched steel bars. International Journal of Fatigue 58, 114–125.

[87] Berto F., Campagnolo A., Meneghetti G., Tanaka K. 2016. Averaged strain energy density-based synthesis of crack initiation life in notched steel bars under torsional fatigue. Frattura ed Integrità Strutturale 38; 215-223.

[88] Lazzarin P., Zambardi R. 2001. A finite-volume-energy based approach to predict the static and fatigue behavior of components with sharp V-shaped notches. International Journal of Fracture 112, 275–298.

[89] Atzori B., Meneghetti G., Ricotta M. 2016. Fatigue and Notch Mechanics. Fatigue and Notch Mechanics. In: Boukharouba T, Pluvinage G, Azouaoui K. (eds) Applied Mechanics, Behavior of Materials, and Engineering Systems. Lecture Notes in Mechanical Engineering. Springer, 9-23.

[90] Glinka G. 1985. Calculation of inelastic notch-tip strain-stress histories under cyclic loading. engineering Fracture Mechanics 22, 839-854.

[91] Atzori B., Filippi S., Lazzarin P., Berto F. 2004. Stress distributions in notched structural components under pure bending and combined traction and bending. Fatigue Fracture Engineering Material Structure 28, 13–23.

[92] Clark G., Knott J.F. 1975. Measurement of fatigue cracks in notched specimens by means of theoretical electrical potential calibrations. Journal of the Mechanics and Physics of Solids 23, 265-276.

[93] Hicks M.A., Pickard A.C. 1982. A comparison of theoretical and experimental methods of calibrating the electrical potential drop technique for crack length determination. International Journal of Fracture 20, 91-101.

[94] Gandossi L., Summers S.A., Taylor N.G., Hurst R.C., Hulm B.J., Parker J.D. 2001. The potential drop method for monitoring crack growth in real components subjected to combined fatigue and creep conditions: application of FE techniques for deriving calibration curves. International Journal of Pressure Vessels and Piping 78, 881-891.

[95] Riemelmoser F.O., Pippan R., Kolednik O., 1999. The influence of irregularities in the crack shape on the crack extension measurement by means of the direct-current potential drop Method. Journal of Testing and Evaluation 27, pp. 42-46

[96] Neuber H., 1977. Die halbelliptische Kerbe mit Riß als Beispiel zur Korrelation von Mikro-und Makrospannungskonzentrationen. Ingenieur-Archiv 46, pp. 389–399.

Appendix A

Below, the equations for the NR solution [67], [68], [69] with $\phi = 0°$ for point A and $\phi = 90°$ for point C are summarized:

$$Y_{\text{A,C-NR-Fz}} = \cdot\sigma_{\text{tension}} \cdot \sqrt{Q} \cdot F\left(\frac{a}{W}, \frac{a}{c}, \frac{c}{B}, \phi\right) \quad \text{A 1}$$

$$Y_{\text{A,C-NR-Mx}} = \cdot\sigma_{\text{bending-x-x}} \cdot H \cdot \sqrt{Q} \cdot F\left(\frac{a}{W}, \frac{a}{c}, \frac{c}{B}, \phi\right) \quad \text{A 2}$$

$$Q = 1 + 1.464 \cdot \left(\frac{a}{c}\right)^{1,65} \quad \text{A 3}$$

$$F = \left[M_1 + M_2 \cdot \left(\frac{a}{W}\right)^2 + M_3 \cdot \left(\frac{a}{W}\right)^4\right] \cdot f_\phi \cdot f_{\text{W}} \cdot g \quad \text{A 4}$$

$$M_1 = 1.13 - 0.09 \cdot \frac{a}{c} \quad \text{A 5}$$

$$M_2 = -0.54 - \frac{0.89}{0.2 + \frac{a}{c}} \quad \text{A 6}$$

$$M_3 = 0.5 - \frac{1.0}{0.65 + \frac{a}{c}} + 14 \cdot \left(1.0 - \frac{a}{c}\right)^{24} \quad \text{A 7}$$

$$f_\phi = \left[\left(\frac{a}{c}\right)^2 \cdot \cos^2\phi + \sin^2\phi\right]^{0.25} \quad \text{A 8}$$

$$g = 1 + \left[0.1 + 0.35 \cdot \left(\frac{a}{W}\right)^2\right] \cdot \left(1 - \sin^2\phi\right) \quad \text{A 9}$$

$$H = H_1 + \left(H_2 - H_1\right) \cdot \left(\sin\phi\right)^p \quad \text{A 10}$$

$$p = 0.2 + \frac{a}{c} + 0.6 \cdot \frac{a}{W} \quad \text{A 11}$$

$$H_1 = 1 - 0.34 \cdot \frac{a}{W} - 0.11 \cdot \frac{a}{c} \cdot \frac{a}{W} \qquad \text{A 12}$$

$$H_2 = 1 + G_1 \cdot \frac{a}{W} + G_2 \cdot \left(\frac{a}{W}\right)^2 \qquad \text{A 13}$$

$$G_1 = -1.22 - 0.12 \cdot \frac{a}{c} \qquad \text{A 14}$$

$$G_2 = 0.55 - 1.05 \cdot \left(\frac{a}{c}\right)^{0.75} + 0.47 \cdot \left(\frac{a}{c}\right)^{1.5} \qquad \text{A 15}$$

and with the factor f_w for tension

$$f_w = f_b \cdot \left\{ \sec\left[\frac{\pi}{2} \cdot \frac{c}{B} \cdot \sqrt{\frac{a}{t} \cdot (1 - 0.6 \cdot \sin(\phi))} \right] \right\}^{1/2} \qquad \text{A 16}$$

where f_b is calculated with

$$f_b = 1 + 0.38 \cdot \frac{a}{c} \cdot \frac{a}{W} \cdot \left(\frac{c}{W}\right)^2 . \qquad \text{A 17}$$

The factor f_w for bending around the x-axis can be calculated as following

$$f_w = \left[\sec\left(\frac{\pi \cdot c}{2 \cdot B} \cdot \sqrt{\frac{a}{W}} \right) \right]^{0.5} . \qquad \text{A 18}$$